ON THE MICROSTRUCTURE OF PEM FUEL CELL CATALYST LAYERS

by

Tatyana Sobolyeva
M.Sc. Chem. Eng., Hochschule Mannheim, 2005

THESIS SUBMITTED IN PARTIAL FULFILLMENT OF
THE REQUIREMENTS FOR THE DEGREE OF

DOCTOR OF PHILOSOPHY

In the
Department of Chemistry

SIMON FRASER UNIVERSITY

Fall 2010

APPROVAL

Name: **Tatyana Sobolyeva**

Degree: **Doctor of Philosophy**

Title of Thesis: **On the microstructure of PEM fuel cell catalyst layers**

Examining Committee:

Chair: **Dr. Erika Plettner**
Associate Professor – Department of Chemistry

_____

Dr. Steven Holdcroft
Senior Supervisor
Professor – Department of Chemistry

_____

Dr. Michael Eikerling
Supervisor
Associate Professor – Department of Chemistry

_____

Dr. Daniel Leznoff
Supervisor
Professor – Department of Chemistry

_____

Dr. Byron Gates
Internal Examiner
Associate Professor– Department of Chemistry

_____

Dr. Göran Lindbergh
External Examiner
Professor – KTH Royal Institute of Technology

Date Defended/Approved: November 2 2010

Declaration of
Partial Copyright Licence

ABSTRACT

In this work, the microstructure of conventional catalyst layers of PEM fuel cells (PEMFCs) is investigated and correlated to the catalyst layer water sorption and retention properties, electrochemical properties and fuel cell performance. Two types of conventional carbon support were chosen for investigation: Ketjen Black and Vulcan XC-72. The microstructure of carbon supports, Pt/carbon catalyst powders, and 3-component, Pt/carbon/ionomer catalyst layers is studied in order to evaluate the effects of carbon support microstructure and Nafion ionomer loadings on the resultant CL microstructure.

The microstructure of the carbon support is found to be a significant factor in the formation of the structure in the 3-component CLs serving as a rigid porous framework for distribution of Pt and ionomer. It is found that deposition of Pt particles on Ketjen Black significantly changes its porosity possibly by forming at the mouth of the support's micropores, thus affecting its effective microporosity, whereas Pt deposited on Vulcan XC-72 does not significantly affect the support's microporosity. The co-deposition of ionomer in the CL strongly influences porosity of the catalyst layer, especially for pore sizes < 20 nm, which are ascribed to the pores within primary carbon particles (pore sizes < 2 nm) and to the pores within agglomerates of the particles (pore sizes of 2-20 nm).

Ketjen Black and Ketjen Black-based CLs were found to posses higher water sorption and retention capacity than Vulcan-XC-72 based catalyst layers due to carbon microstructure.

Electrochemical properties and overall fuel cell performance were found to be strongly dependent on carbon support microstructure, ionomer loading and water sorption and retention capacity of the catalyst layers. It is postulated that carbons with a pore size distribution in the mesoporous range are beneficial for improved Pt utilization, especially, for fuel cell operation in dry conditions. It was also found that in these CLs the ionomer loading can be significantly decreased without significant reduction in performance.

Keywords: PEMFC, catalyst layer, microstructure, water sorption, water retention, Ketjen black, Vulcan XC-72.

DEDICATION

Моим родителям, Людмиле и Анатолию Соболевым.

This is to my parents, Ludmila and Anatoliy Sobolev.

ACKNOWLEDGEMENTS

I would like to thank my senior supervisor Prof. S. Holdcroft for supervision, support, and guidance throughout this thesis. I also extend my thanks and gratitude to my supervisory committee members, Prof. M. Eikerling and Prof. D. Leznoff for supervising this thesis.

My gratitude and appreciation are extended to the following people for their support: Members of the MEA team of the Institute for Fuel Cell Innovation, Drs. Z. Xie, T. Navessin, K.Shi, D. Edwards, P. LeMarquand, M. Haldane for technical guidance and support. Members of the modelling team, Drs K. Malek, J. Gazzarri for helpful discussion. Dr Ohma-san and Mashio-san from Nissan Motor Co for the opportunity to conduct a part of my research at their company and for intensive exchange of knowledge and experience.

My proof-readers Drs T. Peckham, K. Malek and D. Edwards for their timely and constructive criticism.

The staff members of the electronic and machine shop at Simon Fraser University and IFCI for technical support.

Past and present members of the Holdcroft group for their valuable friendship, useful discussions and support throughout my time at SFU.

Prof. W. Schmitt from Hochschule Mannheim for guidance and support through the years.

TABLE OF CONTENTS

LIST OF FIGURES

LIST OF TABLES

LIST OF SYMBOLS AND ABBREVIATIONS

Symbol	Definition, unit
c	The BET constant, -
c_j	Concentration of species j, M
E	Potential of an electrode, V
E^0	Standard potential of an electrode, V
E^0_e	Ideal reversible potential, V
E_{cell}	Cell potential, V
E_e	Equilibrium potential, V
E_{oc}	Open-circuit potential, V
F	The Faraday constant, C/eq
ΔG	Gibbs free energy change in a chemical process, kJ/mol
ΔH	Enthalpy change in a chemical process, kJ/mol
i	Current, A
j	Current density, A/cm^2
j_{lim}	Limiting current density, A/cm^2
j_0	Exchange current density, A/cm^2
k_0	Reaction rate constant, -
m	Mass of a sample, g
n	Number of electrons, -

n	Amount of adsorbed gas, cm^3
n_m	Monolayer adsorbed gas amount, cm^3
N	Avogadro's number, mol^{-1}
p	Gas partial pressure, atm
p_0	Saturation partial pressure, atm
Q	Adsorption charge density, C/cm^2
r_m	Capillary condensation pore radius, m
R	Gas constant, J/mol/K
R_{Ohm}	Ohmic resistance, Ω
s	Cross-sectional area of N_2 molecule, nm^2
t	t-thickness, Å
T	Temperature, K
V	Molar volume of a gas, dm^3/mol
V_L	Molar volume of a liquid, dm^3/mol
α	Transfer coefficient, -
α_a	Anodic transfer coefficient, -
α_c	Cathodic transfer coefficient, -
γ	Surface tension, N/m
η	Overpotential, V
η_{max}	Maximum theoretical thermodynamic efficiency, %
$\eta_{a,a}$	Anode activation overpotential, V
$\eta_{a,c}$	Cathode activation overpotential, V

η_{Ohm}	Ohmic overpotential, V
η_{conc}	Concentration/ mass transport overpotential, V
u	Scan rate, mV/s

Abbreviation	**Definition**
AC	Alternating current
BET	Brunauer-Emmett-Teller
C_{DL}	Double layer capacitance
CCM	Catalyst coated membrane
CL	Catalyst layer
CNF	Carbon nano-fiber
CNT	Carbon nano-tube
CV	Cyclic voltammetry/ voltammogram
DC	Direct current
DVS	Dynamic water vapour sorption
EIS	Electrochemical impedance spectroscopy
EOD	Electroosmotic drag
ESA	Electrochemically active surface area
FC	Fuel cell
GDL	Gas diffusion layer
GDE	Gas diffusion electrode
HFR	High frequency resistance

HOR	Hydrogen oxidation reaction
I/C	Ionomer to carbon ratio
ICE	Internal combustion engine
IUPAC	International union of pure and applied chemistry
KB	Ketjen Black
KB5	Ketjen Black based CL with 5 wt% Nafion ionomer
KB30	Ketjen Black based CL with 30 wt% Nafion ionomer
KB30V5	MEA comprised of Ketjen Black 30 wt% ionomer anode and Vulcan 5 wt% ionomer cathode
KB30KB30	MEA comprised of identical Ketjen Black 30 wt% ionomer anode and cathode
MEA	Membrane electrode assembly
MPL	Microporous layer
OCV	Open circuit voltage
ORR	Oxygen reduction reaction
PEMFC	Polymer electrolyte membrane fuel cell
PFSA	Perfluorosulfonic acid
PSD	Pore size distribution
Pt/C	Pt-carbon composite
PTFE	Polytetrafluoroethylene
R_{CT}	Charge transfer resistance
R_{MT}	Mass transfer resistance
RH	Relative humidity
SA	Surface area

SEM	Scanning electron microscopy
stoich	Stoichiometric ratio
STP	Standard temperature and pressure
TEM	Transmission electron microscopy
TPB	Triple phase boundary
V	Vulcan XC-72
$V_{(xy)}$	Volume
V5	Vulcan-based CL with 5 wt% Nafion ionomer
V5KB30	MEA comprised of Vulcan 5wt% ionomer anode and Ketjen Black 30 wt% ionomer cathode
wt%	Weight percent
WU	Water uptake

1: INTRODUCTION

1.1 PEM fuel cells

Over the past few decades, the direct conversion of chemical energy into electrical energy in fuel cells has been at the centre of attention of electrochemical research and technology development. This interest is due to growing awareness of the technological potential of fuel cells and is a result of society's drive towards developing environmentally friendly power generation.

The fuel cell is an electrochemical device that, in one embodiment, combines hydrogen and oxygen to produce electricity, water and heat. A fuel cell operates as long as fuel and oxidant are supplied to the cell, as opposed to batteries that operate in charge-discharge cycles. First proposed by Schoenbein in 1838 and developed by Sir William R. Grove in 1839, technological development of the fuel cell has lagged behind the more commercially successful internal combustion engine (ICE). The first practical application of a fuel cell was in the 1960s, when a 1 kW alkaline fuel cell was used to provide electricity, heat and potable water for the crew of NASA's Gemini second human spaceflight.[1] Today, potential fuel cell applications range from small portable devices, such as cell phones and laptops, to power generators in vehicles, and stationary power plants for distributed power generation.

Fuel cells are typically classified by temperature of operation (in the range of 40 – 1100 ºC), type of electrolyte (e.g., polymer membrane, ceramic oxide, alkaline solution), and type of fuel (e.g., hydrogen, reformate, alcohol).[2]

1.1.1 Electrochemistry and thermodynamics of PEM fuel cell

The polymer electrolyte membrane fuel cell (PEMFC) is a low temperature fuel cell operated in the range of 80 -105 ºC[1] with a proton exchange membrane as electrolyte. Gas diffusion electrodes are comprised of a gas diffusion layer (GDL) that assures homogenous distribution of reactant gases, and the catalyst layer (CL) where the redox reactions occur. Typically, the fuel used in a PEMFC is hydrogen, and the oxidant is oxygen, the latter usually obtained from air. Figure 1.1 illustrates the operation of a PEMFC.

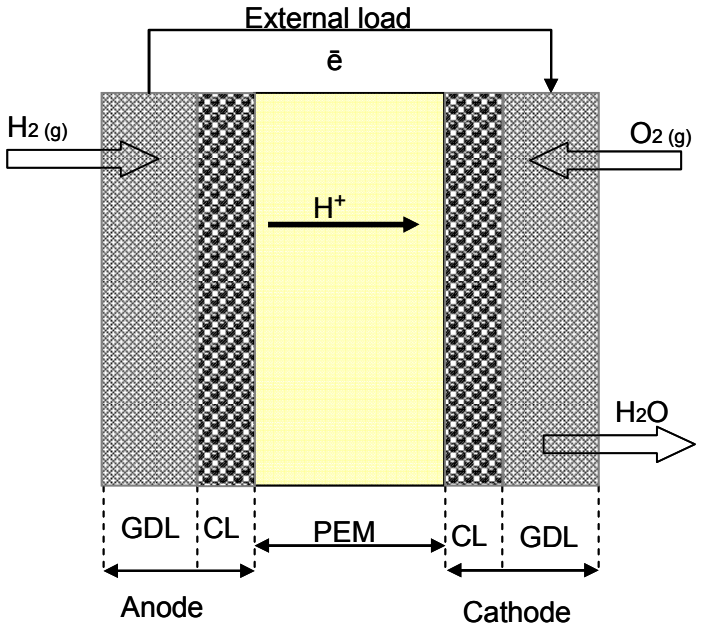

Figure 1.1: Schematic of a membrane-electrode assembly (MEA) of proton exchange membrane fuel cell (PEMFC). CL- catalyst layer, GDL – gas diffusion electrode.

The combination of the proton exchange membrane, the anode and the cathode make up the membrane electrode assembly (MEA). At the anode, hydrogen oxidation occurs (HOR), forming protons and electrons according to equation 1.1,

$$H_2 \rightarrow 2H^+ + 2\bar{e} \qquad E^0 = 0.00\,V \qquad \textbf{1.1}$$

Protons are transported to the cathode through the membrane, and electrons through the external circuit. At the cathode, the oxygen reduction reaction (ORR) occurs by recombining protons with oxygen and electrons to form water as shown in equation 1.2,

$$\frac{1}{2}O_2 + 2H^+ + 2\bar{e} \rightarrow H_2O \qquad E^0 = 1.23\,V \qquad \textbf{1.2}$$

The resulting overall reaction is shown in equation 1.3,

$$\frac{1}{2}O_{2(g)} + H_{2(g)} \rightarrow H_2O_{(l)} \qquad \begin{matrix}\Delta G = -237\,kJ/mol \\ \Delta H = -286\,kJ/mol\end{matrix} \qquad \textbf{1.3}$$

The theoretical cell voltage is the difference between the two half-cell potentials. At equilibrium, the ideal reversible cell potential E_e^0 of the reaction 1.3 is 1.23 V at unit activity of all species and is calculated from equation 1.4,

$$\Delta G = -nFE_e^0 \qquad \textbf{1.4}$$

where n is the number of electrons in the reaction (n=2) and F is Faraday's constant (96485 C/eq). However, the activity of the reactants and products deviates from unit activity under most conditions, e.g., air is only 21% oxygen and reactant gases are combined with water vapour, as they are supplied humidified. The Nernst equation (1.5) is used to calculate the theoretical cell voltage E_e under non-standard conditions,

$$E_e = E_e^0 + \left(\frac{RT}{nF}\right)\ln\left(\frac{(p_{H_2})(p_{O_2})^{1/2}}{a_{H_2O(l)}}\right) \qquad \textbf{1.5}$$

where R is the gas constant (8.314 J/mol/K), T is temperature, and p_{H_2}, p_{O_2} are the partial pressures of H_2, O_2 (1 atm), respectively, and $a_{H_2O(l)}$ is activity of liquid H_2O.

When a load, i.e., external resistance, is applied to a fuel cell, non-equilibrium conditions exist and a current flows through the external load. The rate of electrochemical reactions is proportional to the current density, j, that is, current divided by the geometric area. The voltage-current density relationship of a cell is dictated by irreversible voltage losses: kinetic activation resistance, Ohmic resistance, and mass transport resistance.[3,4] The extent of these losses, or

polarization, is measured by the overpotential (η) that is defined in equation 1.6, and represents the deviation of potential from the equilibrium value.

$$\eta = E - E_e \qquad \textbf{1.6}$$

A schematic representation of a voltage – current density curve, i.e., polarization curve, for an operating fuel cell and associated polarization losses are shown in Figure 1.2.

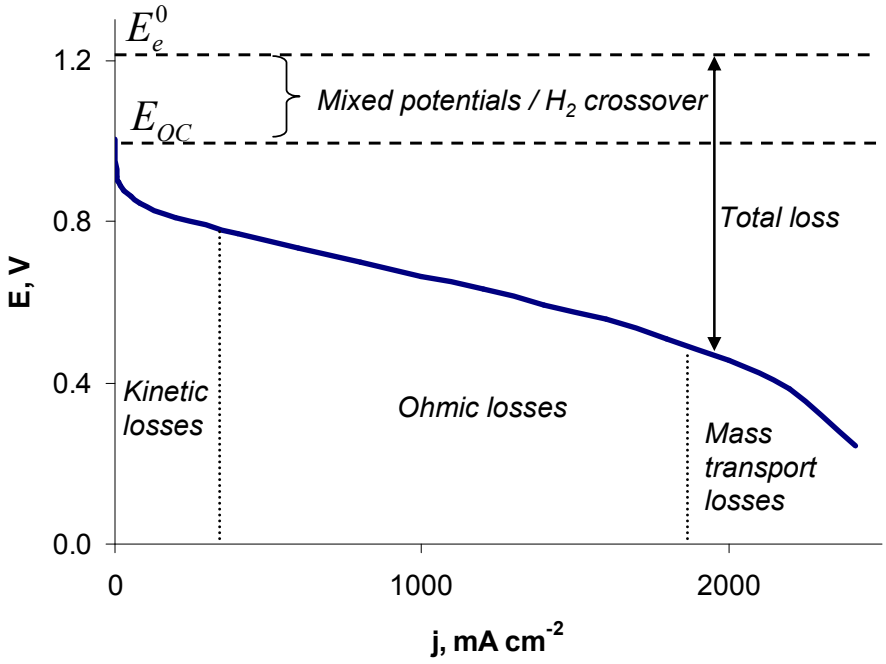

Figure 1.2: Schematic fuel cell performance curve showing polarization losses. E_e^0 is theoretical equilibrium potential at 25 ºC, 1 atm and unit activities. E_{OC} is open-circuit potential of the cell.

The activation polarization (η_a) dominates at very low current densities (j < 100 mA/cm^2) (also known as kinetic losses) is associated with overcoming the

activation energy barrier of the electrode reaction, particularly the ORR because the exchange current density, j_0 (10^{-9} A/cm^2), is much smaller than that of HOR (10^{-3} A/cm^2).[5] The exchange current density measures the rate of exchange of electrons at equilibrium and is a function of concentration of reactants as it shown in equation 1.7.

$$j_0 = nFk_0 c_{O_2}^{(1-\alpha)} c_{H_2}^{\alpha} \qquad \textbf{1.7}$$

where k_0 is the reaction constant, c_{O_2} is concentration of oxygen, c_{H_2} is concentration of hydrogen, α is the transfer coefficient.

Kinetic losses are a function of temperature, pressure, concentration and electrode properties. The relationship between overpotential, η, and current density, j, in the kinetically controlled region is described by the Butler-Volmer equation assuming uniform reaction distribution in the electrode:

$$j = j_0 \left(\exp\left(\frac{\alpha_a \eta F}{RT} \right) - \exp\left(\frac{-\alpha_c \eta F}{RT} \right) \right) \qquad \textbf{1.8}$$

where, F, R and T have their usual meanings, j_0 is exchange current density (A/cm^2), and α_a, α_c are anodic and cathodic transfer coefficients (α= 0.3 – 0.7), respectively.

At intermediate current densities, performance losses are dominated by resistance to ionic current in the electrolyte, electronic current in the electrodes and interfacial contact resistances between cell components, and is called Ohmic polarization (η_{Ohm}). Ohmic polarization is described using equation 1.9:

$$\eta_{Ohm} = i \cdot R_{Ohm} \qquad \textbf{1.9}$$

At high current densities, mass transport losses are dominated by concentration polarization (η_{conc}) and occur when the rate of consumption of reactants at the reaction site exceeds the rate at which reactants are delivered to the reaction site. Concentration polarization is affected by the concentration and flow rate of the reactants, cell temperature, and the structure of gas diffusion catalyst layers. A simple concentration polarization can be described by equation 1.10,

$$\eta_{conc} = 2.303 \frac{RT}{nF} \log\left(\frac{j_{\lim}}{j_{\lim} - j} \right) \qquad \textbf{1.10}$$

where $j_{\lim}$ is the limiting current density (A/cm^2) and is defined as the reaction rate at which the surface concentration of reactants is zero.

The actual cell voltage E_{cell} at any given current density can be represented as the reversible potential of the cell minus overpotentials, as expressed by equation 1.11,

$$E_{cell} = E_{oc} - \eta_{a,a} + \eta_{a,c} - \eta_{conc,a} + \eta_{conc,c} - \eta_{Ohm} \qquad \textbf{1.11}$$

where E_{oc} is the open-circuit voltage (theoretically, $E_{oc} \sim E_e$ but $E_{oc} < E_e$ in fuel cells due to fuel crossover and establishment of a mixed potential).

The power density delivered by a fuel cell is the product of the current density and the cell voltage at that current density. The effect of performance losses on the power density is a peak where the cell is used effectively at high current densities, but undergoes appreciable decline at lower and very high current densities as shown in Figure 1.3. State-of-the-art fuel cells deliver power densities in the range of 0.6 – 1.2 W/cm^2. Powers required by large-scale applications such as automotive and distributed power generation are achieved by assembling single fuel cells into stacks; 75 – 100 kW are typically required for automotive stacks.

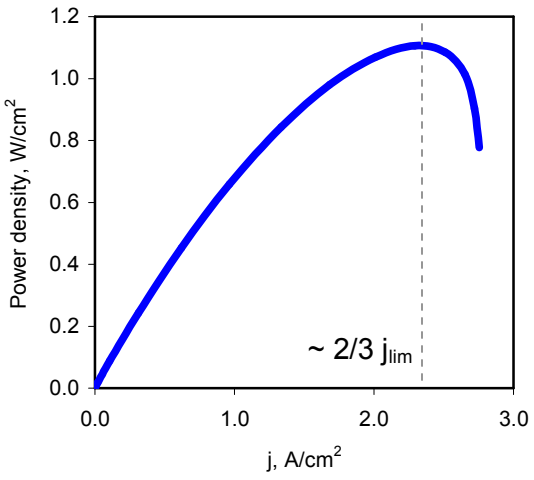

Figure 1.3: Power density curve showing a maximum at approximately 2/3 of limiting current density.

The theoretical efficiency of fuel cells is exceptionally high due to the fact that chemical energy is directly converted to electrical energy in contrast to conventional electricity generation, which takes place in a three-stage conversion process (chemical energy - thermal energy - mechanical energy - electricity). The maximum theoretical thermodynamic efficiency (η_{max}), defined as a ratio of electrical output to the maximum heat output of a hydrogen-oxygen fuel cell, expressed by equation 1.12, is 83% at 25 ºC.

$$\eta_{\max} = \frac{\Delta G}{\Delta H} = \frac{-nFE_e^0}{\Delta H} \cdot 100\% \qquad \textbf{1.12}$$

The efficiency of a fuel cell is also a function of the form of the reaction product (i.e., liquid water or vapour) and temperature. In contrast to the thermodynamic Carnot efficiency, the efficiency of the fuel cell decreases with increasing temperature due to a negative entropy change, ΔS, of liquid water formation as the reaction product, e.g., at 100 ºC, the fuel cell efficiency is 79%. These efficiencies are higher than the maximum theoretical efficiency of conventional internal combustion engine (ICE) that is ~ 60 %.[2] However, a more practical way of expressing and comparing efficiencies of fuel cell and ICE vehicles is in terms of tank-to-wheel and well-to-wheel efficiencies. In tank-to-wheel context, hydrogen powered fuel cell vehicles reach efficiencies in the range 36 – 48% compared to ICE efficiencies of 24 – 30%. Well-to-wheel efficiency is the combination of fuel production and vehicle operation efficiencies with many more variables included in the estimation. Fuel cell vehicles employing

compressed hydrogen produced from natural gas are expected to provide highest well-to-wheel efficiency of up to 32% (alternative sources for hydrogen production are not included in this comparison). Maximum efficiency for ICE powered vehicles is 25% in the case of gasoline as a fuel.[2]

1.1.2 State-of-the-art membrane electrode assemblies

As a result of extensive research over the past decades, PEMFC performance has been significantly improved. A state-of-the-art MEA is comprised of a perfluorosulfonic acid membrane, Nafion, (< 50 μm thick) as electrolyte and catalyst layers (~ 10 μm thick) which utilize Pt catalyst supported on high surface area carbon blacks. Nafion ionomer is added to the catalyst layers as a binder and proton conducting medium.

The introduction of thinner membranes allows for higher cell voltages at current densities ≥ 1 A/cm^2. Currently used 50 μm and 25 μm thick Nafion membranes, Nafion 112 and 211, respectively, result in much lower Ohmic losses than previously used 175 and 125 μm thick Nafion membranes, Nafion 117 and 115, respectively, while still demonstrating high mechanical and chemical stability and hence durability.[6] However, thinner membranes are likely to facilitate gas crossover through the membrane and establishment of mixed potentials at the electrodes.

Carbon-supported Pt catalysts are currently employed instead of Pt-black catalysts as this allows for a reduction of total Pt loading in an MEA from 5 – 10 mg_{Pt}/cm^2 to < 1mg_{Pt}/cm^2 Pt.[7] A breakthrough was accomplished by Raistrick and

co-workers,[8] who proposed impregnating the CL with a Nafion solution. The required loading of Pt was greatly reduced without lowering fuel cell performance. Further improvement was achieved by mixing the catalyst with a Nafion solution.[9-14]

MEA preparation techniques have also evolved, resulting in higher fuel cell performance. One of the first methods of MEA preparation involved catalyst-coated gas diffusion layers (GDL) where catalyst ink was applied (painted, printed, or sprayed) on carbon paper which was subsequently hot pressed onto the membrane. The disadvantage of this technique is a high interfacial resistance between the catalyst layer and the membrane, as well as exposure of ionomer to high temperatures during hot-pressing (> 130 ºC)[15] that might initiate degradation of sulfonic acid groups of the ionomer. The concept of catalyst-coated membranes (CCMs) was introduced in the 1990s by Wilson and Gottesfeld.[13,16] Catalyst layers were applied on a decal from which they were subsequently transferred onto the membrane. Further improvement of this process was achieved by applying the catalyst layers directly onto the membrane, thereby reducing interfacial resistance and avoiding exposure of a CCM to the temperatures exceeding the range of stability of its constituent materials.

The two most common techniques for deposition of catalyst layers on membranes today are ink-based spray deposition and screen-printing. Conventional inks are prepared by mixing Pt/C catalyst powder and ionomer in a mixture of aqueous/alcohol solvent. Homogenous inks are produced by mechanical mixing, sonicating, or ball-milling of the mixtures for an extended

period of time. Inks are subsequently sprayed or printed onto a membrane. The temperature of the process largely depends on the boiling point of the solvent, but usually does not exceed 100 ºC.

Advances in preparation methods of carbon-supported Pt catalyst powders (Pt/C) have allowed for very high wt % of metal on carbon, 40 – 50 wt% versus 10 – 20 wt% used previously, while keeping Pt particles stable to agglomeration. The implementation of high Pt content catalyst powders resulted in decreasing thickness of the catalyst layers for similar Pt loadings per cm^2: 10 – 20 μm compared to the earlier 80 – 100 μm thick catalyst layers at 0.4 mg/cm^2. [9,17] The advantages of thinner catalyst layers are high Pt utilization at low current density and improved water management at high current densities.[18]

Previously, in order to improve water management in an MEA, in particular to facilitate water removal from the cathode, PTFE was used in the catalyst layer as a hydrophobic agent and a binder. However, the permeability of O_2 in PTFE is lower than in the hydrated ionomer (Nafion),[19] and, for this reason, Pt particles covered by PTFE are inactive in the reaction, reducing the overall Pt utilization. Exclusion of PTFE from the catalyst layer has been facilitated by the introduction of a microporous layer (MPL) on the “membrane-side” of the GDL.[20] The MPL is a PTFE-containing hydrophobic carbon-based layer with pore sizes of several micrometers that are larger than those of CL but smaller than those of GDL, which facilitates water flux away from the reaction sites and towards GDL.[21] This has allowed for improved water management and enhanced Pt utilization.

1.1.3 Challenges in FC technology advancement

Despite the significant progress in fuel cell technology over the past decades, challenges remain that have yet to be overcome before broad commercial implementation can be achieved.

Cost reduction in materials and components is still the greatest challenge facing the application of fuel cell systems. Considerable progress has been made here, e.g. with regard to noble metal content. However, in proton exchange membrane (PEM) systems, the platinum loading must be significantly reduced before wide market introduction.

Current technology requires ~ 50 g of Pt per vehicle with a minimum of 0.6 mg/cm^2 (anode + cathode loading). At peak densities of ~ 0.7 W/cm^2 (0.6 V, 1.2 A/cm^2) this translates to 0.86 g_{Pt} per kW.[2] At the current price of platinum, ~ $ 53 US per gram Pt (Johnson Matthey), Pt costs are ~ $ 3,500 – 4,500 US per fuel cell stack, i.e., ~ $ 50 US per kW. For comparison, automotive ICE power generators cost $ 25 – 35 US per kW. For fuel cell technology to be competitive, a fuel cell system needs to be reduced to ~ $ 30 US per kW and Pt content has to be reduced to < 20 g per vehicle (US Department of Energy target of 0.2 g_{Pt} per kW). [22]

There are two major pathways to reduce Pt content in fuel cells: i) increasing the efficiency of Pt utilization by improving catalyst support microstructures; or ii) finding alternatives to Pt metal, either as Pt alloys or as completely Pt-free catalysts. There are numerous research efforts towards developing novel catalyst supports for fuel cell CLs. Ordered mesoporous carbons fabricated by a template

method have been studied as a potential catalyst support in hydrogen and direct methanol PEM fuel cells.[23,24] Mesoporous carbon aerogels produced by pyrolysis of resorcinol-formaldehyde with controlled pore sizes were reported for use in fuel cells.[25,26] Carbon-free titanium columnar catalyst supports are currently under development by Bonakdarpour et al.[27], and organic nano-whiskers have been reported by Debe et al.[2,28] A recent growth in carbon nanotechnology has provided a wide range of nano-structured carbon materials, such as carbon nanotubes (CNT) and carbon nano-fibers (CNF) for use in electrocatalysis.[29]

Pt alloys, such as the core-shell concept (precious metal shell and non-precious metal core) show great potential in reducing the amount of Pt required in a fuel cell.[30] Replacement of Pt with other Pt group metals such as Pd and Ru is regarded as another option; however, this route is likely to suffer from similar cost target limitations while providing lower ORR efficiency. A review of other non-precious metals under consideration for fuel cell electrocatalysis, such as Ti, W, Ta, Mo, Zr, Co, is provided by Borup et al.[31] Despite the intensive research efforts towards alternatives, Pt remains the catalytic material of choice in PEM fuel cells.

Studies by Jaffray et al.[2] on current and projected Pt demand, supply and reserves suggest that wholesale introduction of fuel cell vehicles, e.g., to 50 % of the ICE vehicles, will require a significant increase in Pt supply. However, estimated Pt world reserves are sufficient to cover this demand. Moreover, because PEMFCs operate at low temperature and typically on pure hydrogen, they do not produce NO_x emissions from reactions involving N_2 in air and thus do

not require catalytic converters currently used in ICE vehicles that transform CO and other hydrocarbons to CO_2 and water. Modern catalytic converters utilize 3 – 5 g of Pt per vehicle. Thus, a substantial recovery of Pt group metals is expected from recycling of Pt currently utilized in ICE vehicles.

The commercial viability of fuel cell systems depends strongly on the durability of its components, i.e., the beginning-of-life-performance of a cell has to be maintained over several years. In automotive applications, targets for fuel cell durability are > 5 000 h whereas in stationary applications > 40 000 h.[22] In order to reach the required lifespan, fuel cells are best operated at steady power densities, which is the case of stationary power plant applications. Automotive applications are the most challenging application in the context of durability because of the rapid transient load changes during acceleration and deceleration. In terms of fuel cell operation, this corresponds to cycling between high and low current densities, i.e., low and high voltages. High voltages are known to cause severe degradation of the cathode as carbon is thermodynamically unstable at voltages > 0.4 V[32] and thus exposure to high voltages results in carbon corrosion and subsequent loss of Pt active surface area through Pt agglomeration and dissolution. Mechanisms of cathode degradation have been extensively studied and summarised in a review article by Borup et al.[31] The durability of polymer electrolyte membranes can be impacted by formation of peroxide radicals at the anode due to oxygen crossover from the cathode. Peroxide radicals attack various sites along the polymer chains, causing

polymer degradation and dissolution. Proposed mechanisms of membrane degradation are also summarized in the afore-mentioned review.[31]

Most current fuel cell technologies rely on the use of pure hydrogen. Production, distribution and storage costs for pure hydrogen indirectly impact the wide implementation of fuel cell technology. There are currently three major methods of hydrogen production: natural gas reforming, coal gasification and water electrolysis.[33] The former two directly rely on the availability of fossil fuels, while the last process is of low efficiency, high cost and indirectly dependent on fossil fuel if the electricity used in electrolysis is produced from fossil fuels. However, water electrolysis becomes more meaningful if electricity from renewable sources is used, such as wind and solar energy. Water thermolysis using waste heat from other industrial processes (e.g., nuclear power plants) also presents a viable option. A significant potential for hydrogen production is in various industrial processes involving hydrogen as a by-product (e.g., electrolytic chlorine production). Besides establishing a hydrogen production infrastructure, an infrastructure for the distribution and storage of hydrogen must be concurrently developed.

1.2 Carbon catalyst supports

Supported catalysts are of special interest because they allow for the fine dispersion and stabilisation of small metallic particles and thus high utilization of active metal. Carbon is chosen for many electrochemical applications because of its good electrical and thermal conductivity, low density, adequate stability to corrosion, low thermal expansion, and high purity. The widespread use of carbon

materials in electrochemical systems started in the 19th century, when carbon electrodes replaced copper electrodes in Volta batteries and platinum electrodes in Grove cells. In addition, carbon materials can be produced in a variety of structures, such as powders (carbon black, activated carbon), fibers, thin solids (glassy carbon) and porous sheets. Furthermore, carbon materials are readily available, generally low cost and allow for easy recovery and recycling of the noble metal by burning off carbon.[32,34]

For fuel cell catalysts, carbon blacks are exclusively used to provide a support for Pt dispersions. Carbon blacks with a wide range of surface area, such as Ketjen Black (800 m^2/g), Vulcan XC-72 (220 m^2/g), acetylene black (70 m^2/g), Black Pearls (1500 m^2/g), and many others, are commercially available. Carbon blacks provide adequate electrical and thermal conductivity for fuel cell reactions, and a porous, high surface area medium for gas and water transport. However, carbon is thermodynamically unstable to oxidation over fuel cell operating potentials > 0.4 V, but the kinetics of oxidation are slow at moderate temperatures.[2] The mechanism of oxidation of carbon has been widely discussed in the literature.[32,35,36] Due to advances in preparation of Pt/carbon catalyst powders, carbon blacks allow for uniformly distributed catalyst in PEM fuel cells even if catalyst loading is > 30 wt%, as discussed in Section 1.3.

1.2.1 Microstructure of carbon blacks

Carbon blacks are produced by the oil furnace process from the aromatic oils of petroleum processing. In this process, oil is heated to about 300 ºC and then atomized into the hot zone of the furnace (~ 1400 ºC), where the particles of

carbon black are formed. Higher surface area carbons can be produced if the furnace temperature is increased or by addition of flame modifiers, such as salts of alkali metals. When the aromaticity of feedstock is increased, the degree of aggregation of the carbon black increases.

Carbon black particles vary in size from 5 to 300 nm.[32] Over the years, many models have been proposed for the structure of a single carbon black particle. Most of them are based on X-ray diffraction and high resolution electron microscopy studies. The models suggest that a typical carbon particle consists of small crystalline planes of carbon atoms that form quasi-graphitic crystallites in the range from 12 to 24 Å. These crystallites posses a large d-spacing (distance between the layer planes), typically from 3.5 to 3.6 Å compared to that of graphite (3.354 Å).[32] This d-spacing indicates that the carbon planes do not posses three-dimensional order, as in graphite, but are simply parallel to each other, referred to as turbostratic. A carbon particle is a spherical arrangement of the quasi-graphitic microcrystallites with their size and order becoming smaller and more disordered towards the centre. The orientation of the turbostratic carbon planes is mainly parallel to the surface of the particle. The amorphous phase prevails in the vicinity of the centre of the particle. The dark and bright field electron micrographs of Ketjen black EC suggest that a large fraction of the particles have internal voids.[32] It is expected that further refinements in the model of carbon particles will occur as advancements in high resolution electron microscopy are made.

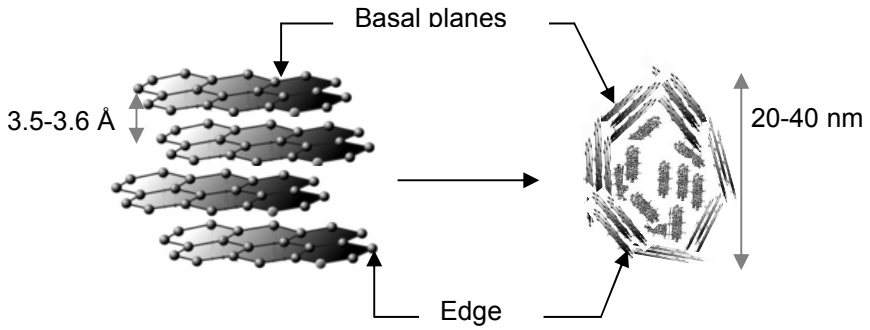

Figure 1.4: Turbostratic microcrystalline domains and their arrangement in a single carbon particle

Carbon particles arrange into agglomerates and, on a larger scale, into chain-like aggregates.[37] The character of agglomeration, e.g., number of particles per agglomerate, shape of the agglomerates, and degree of aggregation depends on the feedstock material and production conditions.

Carbon blacks possess electronic conductivity due to large fractions of the crystalline phase in the primary particle and due to their aggregate structure. The higher the degree of order, i.e., crystallinity, and the degree of aggregation, the higher the conductivity. Graphitization of carbon during heat treatment, increases electrical conductivity due to an increase in the number and size of graphite-like crystallites.

There is a wide range of techniques available for microstructural characterisation of carbon blacks including electron microscopy, X-ray diffraction, gas phase adsorption, mercury porosimetry, and liquid phase adsorption. Until recently, the most widely used carbons in PEMFC have been Vulcan XC-72 and Ketjen Black. These carbons posses similar electronic conductivity but differ in

their surface area and thus, presumably, in morphology. Available structural and physical data for Ketjen Black and Vulcan XC-72 are summarized in Table 1.1.

Table 1.1: Structural properties of Vulcan XC-72 and Ketjen Black (EC) available in literature.

Property	Vulcan XC-72	Ketjen Black
BET surface area ($m^2 g^{-1}$)[30]	254	929
Average particle diameter (nm)[30,36]	20 - 30	30
Projection area of aggregates (μm^2)[36]	0.14	NA
Number of particles per aggregate[30]	79	NA
Contact angle of water(°)[30]	79	84
Electrical conductivity ($S\ cm^{-1}$)[36]	4.5	NA
Apparent density ($g\ cm^{-1}$)	0.145	0.24

1.2.2 Surface properties

The surface microstructure of carbon-black particles is generally very heterogeneous and composed of various crystallographic sites: edge sites, basal sites, defects, and adsorption sites of various activities. The surface structure of carbon affects its physicochemical properties because the reactivity of carbon atoms with unsatisfied valences on the edge sites is greater than that of carbon atoms in the basal plane (refer to Figure 1.4). Consequently, the chemical properties of carbon vary with the relative fraction of edge sites and basal plane sites on the surface. Thus, carbons with a large fraction of edge sites are prone to formation of functional groups, such as – COOH, -OH, -H, =O, -COO.[38,39]

Edge sites and surface groups strongly influence surface wetting properties. The majority of data indicate that carbon itself is not readily wetted by water. The contact angle of water on the basal plane of stress-annealed graphite is 90º, indicative of a hydrophobic surface.[32] It has been reported that generally the surface is rendered more hydrophilic with higher content of oxygen (surface oxides), and more hydrophobic with higher content of hydrogen on the carbon surface. The reported contact angles of 79º and 84º for Vulcan XC-72 and Ketjen Black, respectively, indicate their enhanced hydrophilicity compared to graphitic surfaces due to presence of oxygen containing functional groups.[40] Wettability was reported to be also improved upon addition of metallic particles (Pt, Ag, Ni), which by themselves are readily wetted by water (contact angle of water on Pt is 10º).[5]

Electrochemical activity of carbon has also been found to be a function of crystallographic structure of the carbon. Basal planes are relatively inert to electrochemical reactions compared to the edge sites. Randin and Yeager conducted a series of studies on the dependence of double layer capacitance of carbon on surface properties of carbons. Double layer capacitances have been reported to be 2 – 4 $\mu F/cm^2$ for the basal plane of highly oriented pyrolytic carbon.[41] The capacitance of edge sites is significantly higher, 50 – 70 $\mu F/cm^2$, and dominated by pseudo-capacitance ascribed to the redox transformations of oxygen-containing surface groups.[37,42-44] Double layer capacitance of porous materials may be in the range between 2 – 70 $\mu F/cm^2$ since the surface area of porous carbons is a combination of edge and basal sites and depends on pore

size distribution, specific surface area, crystalline structure and surface properties.[45-48] Kinoshita et al. accepted the value of 8 μF/cm^2 for double layer capacitance of Vulcan XC-72.[36] Shi estimated a double layer capacitance per unit of micropore surface area as 15 – 20 μF/cm^2 assuming that the electric double layer propagates into the micropores, which are accessible by N_2 gas adsorption.[49] However, penetration of the double layer into micro- and mesopores depends on the pore diameter and on the Debye length (the effective thickness of the diffuse double layer). Taking this into account, Vilinskaya et al.[48] and Gryglewitcz et al.[46] reported smaller values for porous carbon in the range of 4 – 10 μF/cm^2. Dependence of the double layer capacity on pore size, particularly on the size of the micropores, has been extensively studied by Chmiola et al.[50-52] The authors have shown that the specific capacitance of carbons increases significantly with the volume of micropores (< 2 nm, IUPAC).

Surface heterogeneity of carbon blacks is strongly affected by heat treatment (i.e., graphitization) - the surface of carbon becomes more homogenous and ordered with basal planes parallel to the surface of the particle. As the temperature of the heat treatment temperature increases, surface layers tend to straighten out and spherical particles are converted to polyhedral shapes. The majority of surface functionalities is also decomposed during heat treatment.

In relation to PEMFCs, the surface chemistry and microstructure of carbons has a direct influence on water sorption and retention, interaction between the carbon surface and catalyst metallic particles during formation of Pt-carbon supported catalysts, electrochemical activity of carbon, and mechanical and

chemical stability and corrosion resistance of carbons. These effects are discussed in the following sections.

1.3 Pt/carbon electrocatalyst powders

Due to the kinetics of oxygen reduction being relatively slow, high surface area electrodes are required to achieve practical electrochemical rates of reaction in fuel cells. Carbon-supported electrocatalysts provide a high interfacial reaction area between O_2, electron and proton conducting phases, and are easily fabricated into electrode structures. Most current technologies for fabrication of MEAs rely on commercially available catalyst powders. Although catalyst manufacturers generally provide little information about the processes and materials for carbon black supported catalysts, numerous preparation methods are described in the literature.[5,53-55] Three of the techniques that are commonly used are impregnation, ion-exchange, and colloidal adsorption.

The impregnation technique involves contacting the support material (e.g., carbon black) with a solution containing dissolved salt of the metal electrocatalyst, e.g., H_2PtCl_6, $Pt(NH_3)_4Cl_2$. The powder must be thoroughly wetted by the salt solution before the excess liquid is removed, usually by evaporation. This step is followed by heating the powder to dryness, and then by thermal or chemical treatment (e.g., hydrogen, formaldehyde) to reduce the metal salt to form metal particles.[56] The mechanism of Pt adsorption on carbon has been extensively studied.[57-61] It has been reported that the interaction of H_2PtCl_6 with carbon implies a redox process in which, after impregnation and drying, the metal complex is stabilized as Pt^{2+} on the carbon surface.[60] Carbon

surface chemistry does not seem to have an effect on the resulting oxidation state of Pt. The presence of surface oxides is found to exert a complicated effect on the impregnation process. The carbon surface-Pt precursor interaction is favoured in presence of surface oxides that make the support more hydrophilic and act as primary anchoring sites. However, after reduction to produce the metallic Pt phase, the majority of these oxygen complexes decompose, with only the most stable complexes remaining. The final dispersion of metallic Pt and sintering resistance are negatively affected by the presence of these surface complexes. The removal of oxygen surface complexes upon reduction gives rise to a redistribution of Pt precursor toward the π-sites in the basal plane of graphitic crystallites. The efficiency the sites is diminished by oxygen complexes due to a withdrawing effect of oxygen which destroys the electron delocalisation at these π-sites.[59] Lozano-Castello et al. reported that the strength of the acid groups has an impact on Pt dispersion.[47] Carboxylic groups and anhydrides are considered to be strong acid groups and show a negative effect on Pt dispersion, whereas lactones, phenols and carbonyls are weaker acids and have a positive effect on Pt dispersion. The specific surface area of carbon seems to have little effect on Pt dispersion using the impregnation method.[57]

In the ion-exchange technique, the dissolved metal salt undergoes specific interaction with the support surface, usually involving a chemical reaction. Commonly, cationic metal complexes (e.g., $M(NH_3)_n)^{z+}$) exchange with a proton on the surface of the carbon. Quantitative exchange is controlled by adjusting the solution pH. Contrary to the impregnation method, the carbon black surface must

be oxidized to produce ion exchange sites such that a high Pt content can be achieved. Chemical or gas phase oxidation produces –OH groups on the carbon surface that favour proton exchange with the Pt complex cation.[61-63]

In the colloidal adsorption method, either Pt metal or Pt oxide (PtO) colloids are formed that are subsequently adsorbed, or reduced and adsorbed in the PtO case, on a carbon support suspended in solution. Numerous reports on various fabrication routes for the colloids can be found in the literature. For example, Pt colloids can be formed from Pt sulphite complexes (produced from H_2PtCl_6 and $NaHSO_3$) that are adsorbed onto the carbon black and subsequently reduced by exposure to hydrogen.[64] This method was found to produce a monomodal particle size distribution in the range 1.2 to 4.3 nm. Some other reducing agents for liquid phase reduction of H_2PtCl_6 are $Na_2S_2O_4$, alcohols, formaldehyde, and sodium citrate.[5,54] Dispersion of Pt can be improved by addition of surface-active agents to the solution.[65] Sorbitan monolaurate prevents the formation of Pt colonies on carbon support[66]; growth of the particle size at high loading electrocatalysts (> 20 wt%) can be prevented by surfactants with electrostatic-based colloid stabilization mechanism,[67] as opposed to polymer steric-based stabilizers. Such a method producing carbon-supported Pt catalyst with very high wt% of Pt (56 – 90 wt%) has been reported by Kim et al.[68] The range of obtained particle sizes can also be tuned by temperature, concentration of reactants, and pH. In contrast to the impregnation methods, the surface area of carbon supports seems to affect Pt particle size produced by the colloidal method, with decreasing particle sizes as a function of increasing carbon black surface

area.[69,70] In another study, the high Pt dispersion ability of Vulcan XC-72 and Regal 600R was attributed to high internal porosity of the former support, and to the carbon surface properties of the latter support.[71] Pt supported on carbon blacks catalyst powder used in this work were prepared by the colloidal adsorption method.

For the maximum utilization of Pt in the electrode, smaller particles are required, so that the ratio of reactive surface atoms to the total number of atoms in the particle is high. At the early stages of ORR catalyst research, it was recognized that mass activity (A/g_{Pt}) of Pt increases with a decrease in Pt particle size, which in turn is a function of the surface area of carbon black supports.[2,69,70,72] Tada et al. reported that CO adsorption on 50 wt% Pt/carbon on 250 and 800 m^2/g carbon supports (corresponding to Vulcan XC-72 and Ketjen Black) increased from 19 ml/g_{Pt} to 30 ml/g_{Pt}, with mass activity increasing from 28 A/g_{Pt} to 55 A/g_{Pt}, respectively.[2] A maximum mass activity for ORR was reported for Pt particles in the range from 3.5 to 5.5 nm by Kinoshita.[73] However, surface specific activity ($\mu A/cm^2_{Pt}$) was reported to decrease with decreasing Pt particle size. Numerous studies suggest that the properties of metal surface atoms in nano-particles differ from those in the bulk as well as from neighbouring surface atoms depending upon the geometric arrangements of the atoms (crystallographic structure). Thus, the specific activity of Pt particles is a function of particle size and concentration of various crystallographic sites on the surface of a particle. The ORR is therefore a structure-sensitive reaction.[5,74-76] Kinoshita suggested that the (100) and (111) crystal phases, but not the edge and corner

sites, are the active sites for ORR at Pt in acid electrolytes.[73] Later studies determined that the energy of adsorption of oxygenated species (-O, -OH) is enhanced at edge and corner sites of a Pt particle. Since the concentration of these sites increases with a decrease in particle size,[73] smaller particles show reduced ORR activity due to the blockage of these sites by adsorbed species. [77-80] Hence, for the ORR, decreasing of Pt size below ~ 3 nm is detrimental. However, in case of the HOR, Pt particle size could be reduced to 1 nm without negatively impacting mass specific activity. In Pt particles < 1nm, crystalline structure has been reported to collapse to form an amorphous phase, thereby making 1 nm the lowest limit for electrochemical activity of platinum.[81]

1.4 PEM catalyst layers

The state-of-the-art catalyst layer is a random heterogeneous, three-component, composite structure comprised of Pt catalyst supported on carbon black, and ionomer. Catalyst layers control the circulation and interconversion of reactant gases and product water through the network of pores, of protons through the interconnected network of ionomer, and of electrons through the ē-conducting network of Pt and carbon. Thus, CLs largely determine efficiency, power density, and water-handling capability of the whole cell.[18] The major objective in catalyst layer development is to obtain the highest possible rates of reactions (HOR and OOR) with a minimum amount of Pt (US Department of Energy target for 2010 is 0.2 g Pt per kW).

The random multi-component nature of CLs makes it extremely difficult to establish a clear microstructural picture and to link structural and material

properties with effects on performance of PEM fuel cell. A tremendous amount of work has been done using modelling methods by Eikerling and co-workers.[18,82-85] In the field of experimental studies, contributions by Uchida et al. are indispensable.[9,14,69,86]

An agglomerate structure with bimodal pore size distribution in the mesoporous range has been proposed for conventional CLs. [9,14,87-89] Carbon particles (10-20 nm diameter) aggregate to form agglomerates (50 – 100 nm diameter).[18,82-85] Primary pores exist within agglomerates (3 – 10 nm); secondary pores (10 – 50 nm) build the pore spaces between agglomerates. Ionomer is assumed to be distributed in the secondary pores, whereas the majority of Pt particles are in the primary pores. Ionomer is necessary for proton conduction within the catalyst layer, however, an excess of ionomer results in the blockage of pathways for gas transport. Models assume that the intra-agglomerate pore space is filled with water that serves as a medium for proton transport as shown in Figure 1.5. Ionomer is not likely to penetrate the intra-agglomerate pores due to the size relations between the ionomer and intra-agglomerate pores. This assumption has also been confirmed in experimental studies.[90]

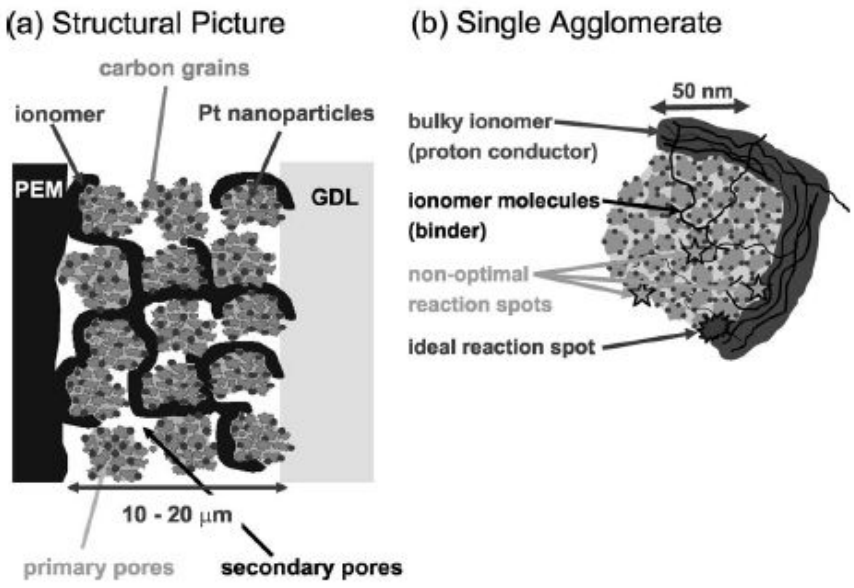

Figure 1.5: Structural picture of catalyst layer depicting (a) various components and porous structure and (b) compositions and reaction spots inside of agglomerate (reproduced from JECS 153 (3) 2006 by Eikerling with permission).

The properties of the ionomer and distribution of hydrophilic and hydrophobic domains in CLs has been found to depend on the nature of the interface (Pt/ionomer, PtO-ionomer, carbon/ionomer) and solvent properties.[83,91] An optimum content for ionomer in CL was found to be ~ 30 wt%.[92-94] At this ionomer loading, a trade-off between sufficient proton conduction and gaseous diffusion of O_2 and water transport is achieved.[12,17,93,94]

Typical thicknesses of conventional catalyst layers is 10 – 20 μm. The catalyst layer thickness plays an important role in reaction kinetics, Pt utilization and water management in CLs. It was reported that effective catalyst utilization can be achieved with ultra-thin planar catalyst layers with thickness ~ 100 – 200 nm. At this length scale, oxygen diffusion (reaction penetration length) is very

close to the thickness of the layer and thus nearly 100% of the Pt particles are used within primary pores.[18] However, thin-film catalyst layers tend to suffer greater mass transport limitations due to flooding.

There are a number of publications on the development of improved designs for conventional catalyst layers. Xie et al. reported an improved performance in the intermediate to high current densities region of GDE with a graded distribution of Nafion ionomer.[95] Wan et al. reported on the preparation of CLs by magnetron sputtering of Pt layer on a carbon-Nafion ink layer alternatively to produce multilayer CLs.[96] Maric et al. reported the fabrication of 1 – 3 μm thin CL with 0.05 mg_{Pt}/cm^2 on cathode by reactive spray deposition.[97]

1.5 Polymer electrolyte membrane and ionomer

There are a number of critical characteristics for a proton exchange membrane in PEM fuel cells. They include: high proton conductivity that allows high current densities without significant Ohmic losses, low electrical conductivity to prevent short-circuiting of the cell, low permeability to fuel and oxidant to prevent mixed potential on the electrodes, good mechanical stability and durability under fuel cell operating conditions.

A perfluorosulfonic acid (PFSA) ionomer electrolyte (Nafion®) developed by DuPont in 1960s has become a standard material for the proton exchange membrane in PEMFCs. Nafion is a copolymer comprised of a hydrophobic tetrafluoroethylene (PTFE) backbone copolymerized with a monomer bearing a

pendant side chain of perfluorinated vinyl ether, terminated by a sulfonic acid group, as shown in Figure 1.6.

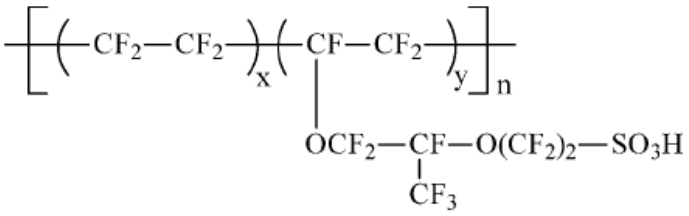

Figure 1.6: Chemical structure of Nafion®; x=6-10, y=1.

The hydrophobic backbone resembling PTFE makes Nafion highly durable and chemically resistant. Terminal sulfonic acid groups, $-SO_3H$, are hydrophilic and responsible for water sorption and formation of proton conducting channels within the membrane. Due to the specific nature of hydrophobic-hydrophilic phase separated morphology, an interpenetrating hydrophilic and hydrophobic networks are formed in the Nafion membrane imparting high stability and high proton conductivity, 0.1 S/cm, at temperatures below 100 ºC and in fully humidified conditions.[98]

There is a vast amount of literature on the hydrophilic/hydrophobic phase-separated morphology,[99-101] water sorption,[102-104] proton conduction mechanisms,[105-107] chemical and mechanical stability, and durability of Nafion.[101] Despite the superior performance of Nafion in low temperature hydrogen fuel cells, it suffers from reduced conductivity at higher temperatures (> 80 ºC) and

low RH. Moreover, the relatively high cost and problematic recycling of fluorous-containing materials, motivates the search for alternative, primarily hydrocarbon-based polymers. These include: sulfonated poly(ether ether ketone) (sPEEK), sulfonated poly(phenoxy benzoyl phenylene) (sPPBP), sulfonated poly(ether sulfone) (sPES), poly(benzimidazole) (PBI).[100,108,109] Hydrocarbon polymers are of particular interest due to their low cost and low environmental impact.[110]

In the catalyst layer, Nafion ionomer is incorporated as a proton conducting phase necessary for formation of the triple phase boundary. Proton conductivity, high permeability to the reactant gases, and chemical and thermal stability of the ionomer are the key requirements. The physicochemical properties and distribution of Nafion ionomer in the CL is under debate. While it was reported that Nafion forms rod-like fibers of ~ 15 – 25 Å in radius and ~ 125 – 350 Å in length in polar solvents,[111] many reports suggest that on the surface of Pt/carbon it distributes in the form of a thin film or as aggregates. Nafion micelle of a size of ~ 200 nm in the CL fabricated from water – alcohol solution was reported by Arico et al.[112] Nafion aggregates of 10 – 20 nm size observed by electron tomography were reported by Uchida et al.,[113] while ~ 6 – 9 nm diameter spherical globules were detected on pyrolytic graphite by Heisgen et al.[114] Wood et al. reported a layered structure of Nafion polymer chains oriented flat on the substrate surface; the first chain strongly interacts with the substrate while the second layer interacts with the first ionomer chain.[91]

Proton conductivity of the ionomer, as in the case of the membrane, depends greatly on the water content. To date, there is no experimental evidence on the

water uptake capacity of the ionomer in the CL; however, it is expected to differ significantly from that of the bulk membrane. If ionomer is believed to be distributed as a thin nanometer-thick layer on the Pt/carbon, it is unlikely that a phase-separated morphology with fully formed hydrophilic clusters of size ~ 3 nm[107] characteristic to the bulk membrane can be formed. It is believed that proton conducting channels within the membrane are formed by water that is strongly adsorbed on the $-SO_3H$ groups, i.e., surface water, and water in the center of the water-filled channels. Proton conductivity in the central region of these channels is expected to be close to the conductivity in bulk water, whereas it is expected to be much lower for the layer of surface water.[107] Hence, due to the predicted absence of water-filled channels within the ionomer layer, a lower proton conductivity of ionomer in the CL is expected.

Gas permeability of the ionomer layer is crucial for the kinetics of the fuel cell reaction. A large number of Pt particles are covered with a layer of ionomer and thus the ability of the gas to penetrate this ionomer layer has to be very high. The permeability of gases through the ionomer layer is expected to have a similar dependence on water content as in the Nafion membrane. It has been reported by Sakai et al., that the lower the hydration of Nafion membrane the lower is gas permeability.[19] The dependence of O_2 solubility and diffusion coefficients on temperature and pressure has been reported by Beattie et al.[115] A dependence of O_2 permeability in the CL on the porosity of the carbon support has been reported by Ignaszak et al.[116]

1.6 Experimental techniques relevant to catalyst layer characterization

1.6.1 Nitrogen adsorption

Physical gas adsorption is the most frequently used technique for evaluation of specific surface areas and pore sizes of porous materials. When a solid (adsorptive) in a closed space is exposed to a gas or vapour (adsorbent) at some definite pressure, the solid adsorbs the gas due to physical (van der Waals) forces between the solid and the gas. The quantity of a gas taken up by a sample is calculated from the fall in pressure by application of gas laws given the known constant volume of the vessel and the solid. A plot of amount of adsorbed gas versus partial pressure is known as an adsorption isotherm. The isotherms are classified into six types.[117-119]

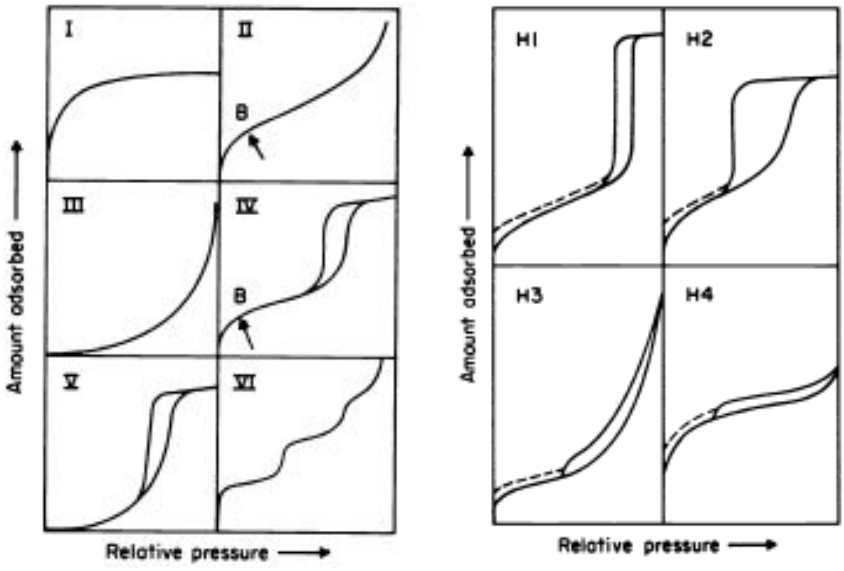

Figure 1.7: Types of physisorption isotherms (a) and types of hysteresis loops (b). (Reproduced from Sing et al , Pure & Appl. Chem., 57 (4) 603 with permission).

The essential features are the rise of isotherm at very low partial pressures, presence or absence of hysteresis and the presence of saturation at partial pressure close to unity.[118-120] Characteristic feature of the type I isotherm is a plateau indicating attainment of saturation and is characteristic of microporous adsorbents. Types II and IV are characteristic of strong adsorbent-adsorbate interactions represented by a steep rise in the low partial pressure region. Type II is indicative of non-porous solids, while type IV isotherm is characteristic of mesoporous solids. Type III and V isotherms occur in the systems where the adsorbent-adsorbate interaction is very weak. Type III is indicative of non-porous solids, while type V implies the presence of porosity. Type VI is rare and is associated with formation of complete monolayer before each subsequent layer commences.

Hysteresis generally indicates the presence of porosity and capillary condensation. H1 type is often obtained with agglomerates of spheroidal particles of uniform size and array and is indicative of microporosity. H2 type is also characteristic of spherical agglomerate systems but without a well-defined pore size distribution and pore shapes. Types H3 and H4 are obtained with adsorbents having slit-shapes pores or plate-like particles, and are indicative of macropores where no saturation is reached.

The specific surface area of a porous material is assessed using the Brunauer-Emmett-Teller (BET) equation:

$$\frac{p/p_0}{n(1-p/p_0)} = \frac{1}{n_m c} + \frac{c-1}{n_m c}(p/p_0) \qquad 1.13$$

where, p represents gas pressure, p_0 is saturation gas pressure, n is amount of adsorbed gas, n_m is monolayer adsorbed gas amount, and c is the BET constant which takes into account the energy of adsorption defined by equation 1.14:[120]

$$c = \exp\left(\frac{E_1 - E_L}{RT}\right) \qquad 1.14$$

The BET method extends the Langmuir theory of monomolecular gas adsorption on a solid surface to multi-layer adsorption, assuming physical adsorption of gas molecules in sequential layers. Each monolayer serves as a site for adsorption for the next layer. The energy of each additionally adsorbed layer, from the second layer onwards, is equal to that of the previous layer and equivalent to the heat of liquefaction of the gas. Each layer can be independently described by Langmuir theory, assuming the solid surface is energetically homogeneous. Despite its simplicity, the theory has been shown to provide an adequate representation of real systems, and is consistent with experimental data for a variety of porous materials.[120,121] The plot of $\frac{p/p_0}{n(1-p/p_0)}$ against (p/p_0) gives a straight line with slope $s = \frac{(c-1)}{n_m c}$ and intercept $i = \frac{1}{n_m c}$. A solution to these two simultaneous equations gives the monolayer capacity $n_m = \frac{1}{s+i}$ and

a measure of the adsorption energy c. For most materials, a linear relationship exists between relative pressures of about 0.05 and 0.30.[120] Surface area is then calculated from the monolayer capacity using equation 1.14,

$$SA_{BET} = \frac{n_m \cdot N \cdot s}{V} \qquad 1.15$$

where N is Avogadro's number, s is cross-sectional area of the N_2 molecule (0.162 nm^2), and V is molar volume of adsorbent gas.

Surface area in porous materials has contributions from the external surface area of the particles as well as the internal surface of pores, cavities, and fissures. In many cases, however, the distinction is not clear, for the surfaces of particles themselves can have cracks and fissures. The line of demarcation between two kinds of surface is drawn in an arbitrary way – the external surface may be taken to include all fissures and cracks which are wider than they are deep. The internal surface will then comprise the walls of all cracks, pores and cavities, which are deeper than they are wide. However, a range of porous materials, including carbons, have an internal surface area greater by several orders of magnitude than the external surface area. These cavities, fissures, cracks are termed pores. A classification of pores according to their average width originally proposed by Dubinin[122,123], and now officially adopted by IUPAC, differentiates micro-, meso- and macropores. Micropores are < 2 nm, mesopores are between 2 and 50 nm, and macropore are > 50 nm. The basis of the classification is that each of the size ranges corresponds to characteristic

adsorption effects as manifested in the isotherm. In micropores, the interaction potential is significantly higher than in wider pores due to the proximity of the walls, and the amount adsorbed at a given partial pressure is correspondingly enhanced. In mesopores, capillary condensation takes place, which in turn results in the presence of hysteresis. Presence of macropores is evident from the exponential increase of the isotherm at the partial pressures close to one.

The Kelvin equation, relating pore size to gas partial pressure for capillary condensation or evaporation, is usually applied to determine pore sizes in the meso-to- macroporous range:

$$\ln\frac{p}{p^0} = \frac{-2\gamma V_L}{RT}\frac{1}{r_m} \qquad 1.16$$

where p represents gas pressure, p_0 is saturation vapour pressure, γ is surface tension, V_L is molar volume of the liquid, r_m is capillary condensation radius, and R and T have their usual meanings. However, the Kelvin equation in its original form is a crude simplification of the actual process of capillary condensation, hence numerous corrections and modifications have been developed. Introduction of the statistical film thickness (t-thickness) that accounts for the formation of the liquid-like layer on the pore wall prior to commencement of capillary condensation was shown more accurately to represent experimental data. A universal dependence of the t-thickness on partial pressure of nitrogen was found for various adsorbate surface types.[124,125] DeBoer et al. conducted an extensive study of the t-curve method for various porous materials,[124-131] and

recognized the actual pore radius to be the sum of the radius calculated by the Kelvin equation and the thickness of the adsorbed t-layer at each given partial pressure. An important refinement of the Kelvin equation using the t-thickness correction was performed by Barret, Joyner and Halenda (BJH).[132] The relationship that accounts for the formation of a condensed layer of gas molecules on the pore wall prior to capillary condensation in case of N_2 as adsorbate is the Harkins – Jura equation:

$$t = \left(\frac{13.99}{\left(0.034 - \log(p / p_0)\right)} \right)^{1/2} \qquad 1.17$$

where t is the thickness of the adsorbed layer on the pore wall, Å, p is partial pressure of N_2, and p_0 is saturation pressure of N_2 at 77 K.[124] The slit-shape pore geometry is assumed. The volume of adsorbed nitrogen is plotted against t-thickness to produce the so-called t-plot. The volume of micropores (< 2 nm) is found by multiplication of the t-plot y-intercept by the density conversion factor of 0.001547. This factor corresponds to the density conversion from gaseous N_2 at STP condition to liquid phase. The mesoporous surface area is found by multiplying the slope of the t-plot by factor 1.547. The microporous surface area can then be found from the difference in the total BET surface area and the mesoporous surface area.

1.6.2 Dynamic water vapour sorption (DVS)

Water vapour sorption is identical in fundamental principles to N_2 adsorption. Water vapour molecules are adsorbed by adsorbate through weak dispersion forces (physical adsorption). However, water is a polar molecule and thus the character of water vapour sorption is dependent on the polarity of the adsorbent. Stronger water vapour adsorption is observed with polar adsorbents and very weak adsorption with non-polar adsorbents.[120] In case of non-polar hydrophobic adsorbents, such as carbon, interaction between water molecules prevail over the interaction between water and the carbon surface, and very little adsorption is seen in the region of low partial pressures of an isotherm. Presence of oxygen-containing functional groups and edge sites on the surface of carbon enhances water sorption in the low partial pressure range because of their polarity. For this reason, water vapour sorption isotherms are often Type 3 isotherms according to IUPAC classification. Type 3 isotherm is characterised by low adsorption in the low gas partial pressure range and a rapid increase in adsorption in the high partial pressure range, refer to Figure 1.7.

In this work, water vapour sorption is evaluated using gravimetric water vapour sorption technique, as opposed to the volumetric N_2 adsorption described above. The experimental set-up is schematically shown in Figure 1.8. The sorption isotherm is recorded in isothermal condition by exposing a sample to a range of RH; a difference in sample weight at a given RH to a dry sample is used to construct a sorption isotherm. Targeted RH is achieved by mixing a water

vapour-saturated stream of nitrogen gas with a dry stream of gas. RH is monitored and controlled using a dew-point sensor.

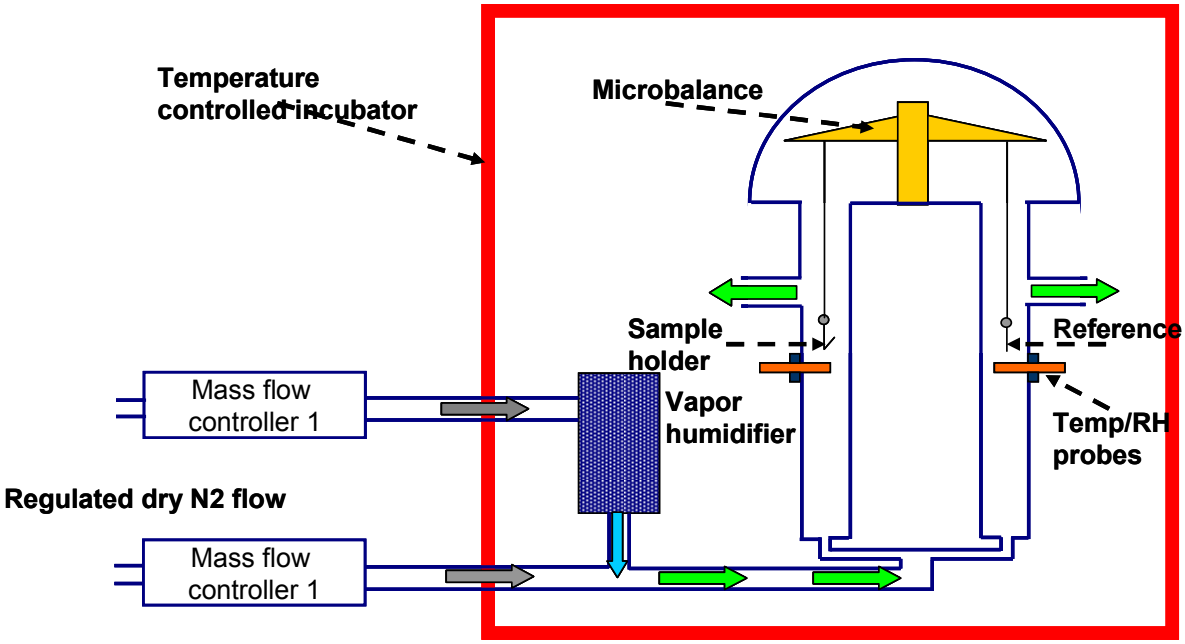

Figure 1.8: Schematic of Dynamic Vapour Sorption chamber used for evaluating water vapour sorption and retention capability of CLs.

Water uptake of a sample at each stage of relative humidity is found using equation 1.17:

$$WU_{RH} = \frac{m_{RH} - m_{dry}}{m_{dry}} \qquad 1.18$$

where WU_{RH} is water uptake at a certain RH, m_{RH} is mass of the sample at this RH, and m_{dry} is the mass of a sample at 0% RH.

Sorption isotherms are used to evaluate total water uptake as well as surface hydrophilic properties. Water retention properties are estimated from the shape and extent of a hysteresis.

1.6.3 Cyclic voltammetry

Cyclic voltammetry (CV) of hydrogen adsorption/desorption is a common diagnostic tool for measuring the mass-specific electrochemically-active surface area (ESA) of Pt. In-situ two-electrode configuration was used in which the anode serves as both the reference and the counter electrode, and the cathode is the working electrode. Hydrogen is fed to the anode, the cathode is purged with nitrogen in order to avoid the reaction of hydrogen with oxygen. The potential of the working electrode is swept between 0 – 1 V in the forward and backward scans. Hydrogen molecules crossing over to the cathode through the membrane are instantly oxidized at the potentials > 0 V and consequently adsorbed on Pt surface during the forward scan and desorbed during the backward scan. The reaction of interest is the electrochemical reduction of protons (H^+) and formation of adsorbed atomic hydrogen on the surface of Pt,[3]

$$Pt + H^+ + \bar{e} \leftrightarrow Pt - H_{ads} \qquad 1.19$$

The atomic hydrogen adsorption charge density Q (C/cm^2) due to the above reaction is determined from the hydrogen adsorption region of a CV as shown in Figure 1.9. The ESA is then calculated from the measured charge density and the Pt content [Pt] in the electrode (mg_{Pt}/cm^2) as shown in equation 1.9:

$$ESA = \frac{Q}{[Pt] \cdot 0.21} \qquad \textbf{1.20}$$

where 0.21 mC/cm^2 is the average charge density corresponding to the average density of Pt atoms in Pt (100), (110) and (111) crystallite faces. It is assumed that each hydrogen atom adsorbs on one Pt atom.

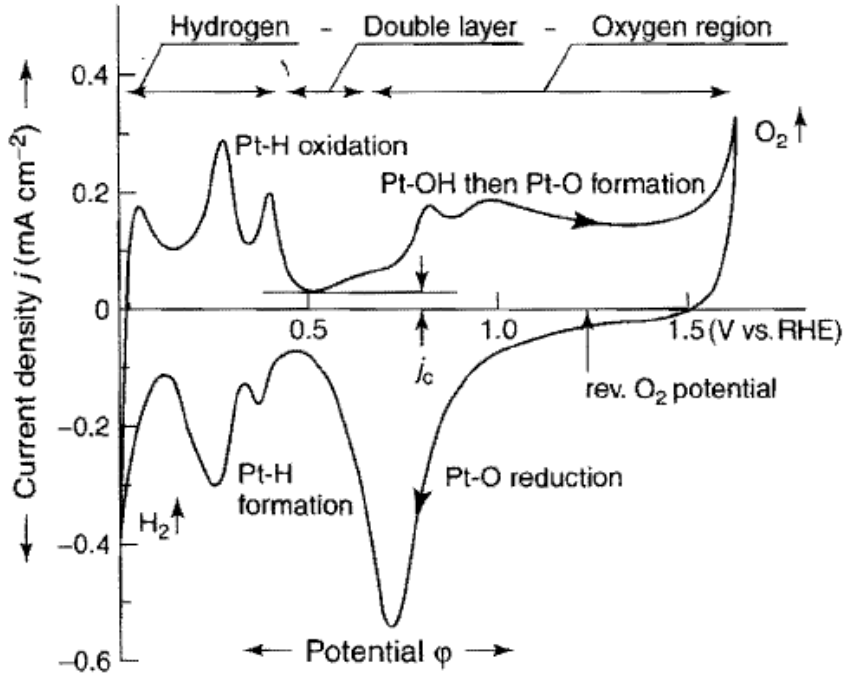

Figure 1.9: Cyclic voltammogram of polycrystalline Pt electrode in 1 M KOH, 20ºC, nitrogen purged, sweep rate = 100 mV/s. (Reproduced from Handbook of Fuel Cells, V.2 with permission from John Wiley &Sons).

The double layer charging and the hydrogen crossover currents are subtracted from the area of hydrogen adsorption in order to avoid overestimating the charge attributed to the electrocatalytic activity. Hydrogen crossover current

is the current produced by oxidation of H_2 that penetrated to the cathode from the anode through the membrane. Double layer charging current arises from the charging of the electrode interface during the potential scan. It is determined from the CV in the 0.4 – 0.5 V range, where no other faradaic processes occur.

The H_2 crossover current is determined from the chronoamperometry measurement under H_2/N_2 atmosphere (anode/cathode). The cathode potential is stepped from 0.2 to 0.5 V in 0.1 V increments and the corresponding faradaic current of hydrogen oxidation at each potential step is monitored as a function of time. The steady-state current density corresponds to hydrogen crossover current density.[133]

Double layer capacitance is attributed to the interface between the electron and the proton-conducting phase in the electrode and thus provides information about the extent of ionomer coverage on Pt and carbon. Double layer capacitance is calculated from the double layer charging current determined from the CV in the 0.4 – 0.5 V range accounting for the hydrogen crossover current, i_{corr}, and scan rate, υ:

$$C_{DL} = \frac{i_{corr}}{\upsilon} \qquad 1.21$$

1.6.4 Electrochemical impedance spectroscopy

Electrochemical impedance spectroscopy (EIS) is a non-invasive diagnostic technique for evaluation of fuel cell properties such as membrane and electrode resistance, reaction kinetics, and mass transport effects. The variety of

processes occurring in a fuel cell possess different time constants. For example, diffusion processes are relatively slow and occur on the time scale of seconds and sub-seconds, whereas charge transfer processes occur at much shorter time scale of sub-milliseconds.[3] EIS takes advantage of the large spectrum of time-scales over which different processes in the fuel cell occur to deconvolute individual effects by applying a perturbing signal (voltage or current) over a broad range of frequencies. Slower processes respond to lower frequencies, faster processes respond to high frequency perturbations. A sinusoidal (AC) perturbation signal of known amplitude and frequency is applied to the cell, and amplitude and phase of the AC response of the cell are monitored. The frequency of the signal can be varied from several kHz to mHz. The impedance response is usually analyzed by application of physical models or equivalent circuit analogues to fit the experimental data. Equivalent circuits are often comprised of resistors, capacitors and various distributed circuit elements corresponding to such physical phenomena as diffusion or mass transport limiting process.[134]

A one-dimensional transmission line model is used to evaluate ionic resistance of CLs.[92,135,136] This is the classical model for the charging of a porous electrode proposed by De Levie.[137] The transmission line with multiple elements is used to mimic the continuous electrical network of carbon and Pt particles in the CL. Each element in the line consists of a proton resistance (R_p), a charge transfer resistance (R_{CT}), electronic resistance (R_e) and double layer capacitor (C_{dl}) as shown in Figure 1.10. Electronic resistance is assumed to be negligible.

Ionic transport and charge transfer dominate the high frequency EIS response (> 1 kHz) of the Nyquist plot for porous media.

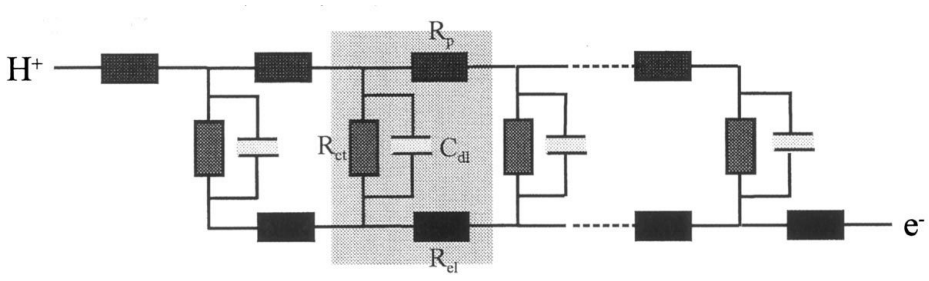

Figure 1.10: The 1-D transmission line equivalent circuit. Elementary unit comprising of proton resistance (R_p), charge transfer resistance (R_{CT}), double layer capacitance (C_{dl}) and electronic resistance (R_e) is highlighted. (Reproduced from Eikerling et al, J. Electroanal. Chem. 1999 with permission)[136]

In an H_2/N_2 environment, no charge transfer occurs and, according to this model, the impedance of the electrode in the Nyquist plot should consist of a 45º region at high to intermediate frequencies and a 90º region representing limiting capacitance and resistance at low frequency. The resistance to proton transfer in the membrane, R_m, is determined from the high frequency intercept of the Nyquist plot with abscissa; proton resistance in CL, R_{CL}, from the difference between the intersection point of the linear region at lower frequencies and the high frequency proton transport resistance as shown in

Figure 1.11. The deviation of the low frequency region from theoretical 90º is attributed to the faradaic reactions in the CL, e.g., oxidation of the crossover H_2.

In an H_2/O_2 environment, a semi-circle in the Nyquist plot is produced due to Faradaic charge transfer reactions. At low current densities, a semicircle is attributed to the charge transfer resistance of the reaction. At high current densities, where mass transport limitations are significant, the semi-circle is the sum of charge transfer and mass transfer resistance ($R_{CT}+R_{MT}$).[4,92]

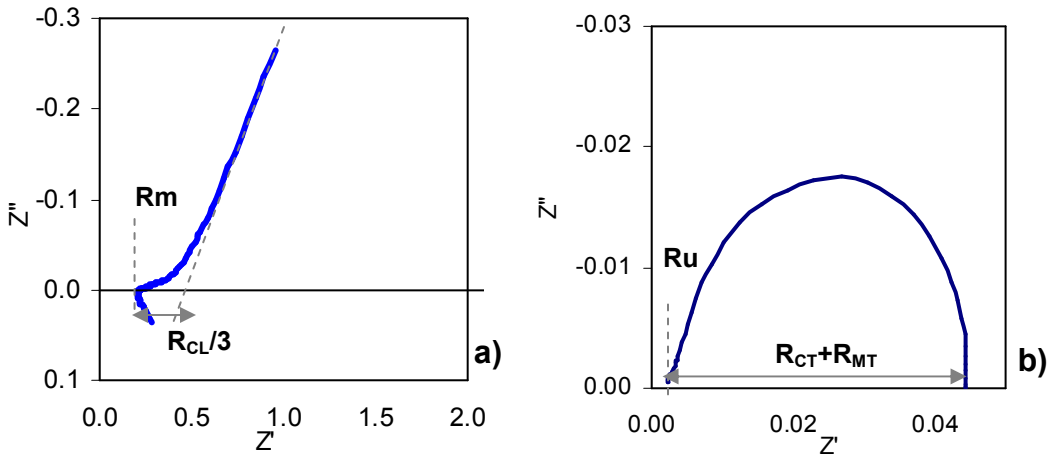

Figure 1.11: EIS Nyquist plot in a) H_2/N_2 atmosphere and b) H_2/O_2 atmosphere.

The high frequency intercept of the Nyquist plot with the Z'-axis is the uncompensated resistance, R_u, which is attributed to the sum of proton resistance in the membrane, cell and cell hardware resistances. At low overpotentials, i.e., low current densities, where the mass transport resistance is not significant, the main contributor to the resistance is the interfacial charge transfer and the diameter of the semi-circle equals R_{CT}. At high overpotentials, i.e., high current densities, oxygen diffusion is dominant, especially when air is used as oxidant.[92]

1.6.5 Scanning electron and transmission electron microscopy

Scanning electron microscopy (SEM) permits characterization of heterogeneous materials on a nanometer to micrometer scale.[138] In SEM, the area to be examined is irradiated with a finely focused electron beam that is swept across the sample to form images. The electrons interact with the atoms that make up the sample producing signals about the sample's topography and composition. The types of signals produced from the interaction of the electron beam with the sample include secondary electrons, backscattered electrons, characteristic X-rays, light, specimen current and transmitted electrons. The signals are obtained from the interaction with atoms at or near the surface of the sample, and are collected by detectors to form images of the sample. In the secondary electron imaging mode, SEM can produce very high-resolution images of the sample's surface, revealing details in the range of 1 – 5 nm in size. Due to a large field of depth, images with the three-dimensional appearance can be attained that are useful for understanding the surface structure of the sample. Magnification up to 500,000 can be achieved. In the back-scattered electron imaging mode, because the intensity of the signal is related to the atomic number of the specimen, information about distribution of different elements in the sample can be obtained.

In the case of FC catalyst layers, information about CL morphology including pore sizes and porosity of the CLs, roughness of the CL surface, and distribution of ionomer can be obtained.

In transmission electron microscopy (TEM), a beam of electrons is transmitted through a very thin sample, interacting with the sample as it passes through.[139] An image is formed from the interaction of electrons transmitted through the sample with an imaging device. The most common mode of operation for a TEM is the bright field imaging mode. In this mode, the contrast formation is formed directly by occlusion and absorption of electrons in the sample. Thicker regions of the sample or regions with a higher atomic number will appear dark, whilst regions with no sample in the beam path will appear bright in this imaging mode.

In the case of FC catalyst layer, TEM images provide useful information about shape and size of carbon particles, character of particles aggregation into agglomerates, and location of crystal and amorphous phase in carbon particles. Information about location and size of Pt particles on carbon support is also obtained.

1.7 Objectives of this research

As outlined previously, a cost reduction in fuel cells is a major technical goal to commercialization. This can be achieved by reducing the amount of Pt used in the catalyst layer of the fuel cell by improving Pt utilization. Pt utilization greatly depends on the microstructure of the catalyst layer and fuel cell operating conditions. It has been recognized that high surface area catalyst supports, e.g., carbon, is beneficial to the efficient distribution of Pt particles, hence requiring a lower Pt content in the CL. Based on these considerations a large number of novel, nano-structured, high surface area catalyst support materials for fuel cells

have been synthesized.[23,24,27,28,140] However, none of them has provided an enhanced fuel cell performance compared to the conventional carbon blacks, such as Ketjen Black. The reason is that the high surface area of catalyst support alone cannot provide improved fuel cell performance due to the multi-component and multi-functional nature of the catalyst layer. The goal of this work is to investigate how microstructural properties of the constituent components of the catalyst layer influence its resultant microstructure, and which of them are beneficial for mass transport and for improving the electrochemical properties and overall fuel cell performance.

In Chapter 2, a study of the microstructures of Ketjen Black and Vulcan XC-72 conventional carbon black catalyst supports, Pt/carbon composites and Pt/carbon/ionomer catalyst layers is described. Microstructure is investigated in terms of the character of carbon particle aggregation, surface area, pore volume, pore size distribution, and pore network. The structural differences between carbons are identified and their impact on the distribution of Pt and ionomer is assessed. The significance of micropores (< 2 nm) on the distribution of Pt particles and their role in the fuel cell reaction is discussed, as well as the role of the mesopores > 20 nm on ionomer distribution. Speculations are offered about the effect of the detected differences in microstructure of these carbon catalyst supports and catalyst layers prepared from them in terms of mass transport properties and, in particular, water transport in the catalyst layer.

In Chapter 3, water sorption, retention and desorption properties of Ketjen Black and Vulcan XC-72 carbons, Pt/carbon composites and Pt/carbon/ionomer

catalyst layers are investigated. Differences in water sorption and retention properties are analyzed in terms of hydrophilicity/ hydrophobicity of the catalyst layer components as well as microstructural properties such as the total pore volume and the pore size distribution. On the basis of this experimental data, considerations are made about the required water sorption and retention properties of the catalyst layer dependent on the application as a cathode or as an anode catalyst layer.

In Chapter 4, CL microstructure is correlated to electrochemical properties of the catalyst layers such as electrochemically active surface area, double layer capacitance, proton conductivity, charge and mass transport resistances, fuel cell performance and water management properties. Effects of microstructure of the catalyst layer on Pt utilization in a range of relative humidity are discussed. The role of ionomer and water contents in the catalyst layer during fuel cell operation is examined. Fuel cell performances of the membrane electrode assemblies with dissimilar water sorption and retention properties of the cathode and the anode catalyst layer are studied.

Research findings are summarized in Chapter 5, research findings are summarized and future work is proposed. Microstructural parameters of catalyst supports beneficial for fuel cell reaction are discussed.

2: MICROSTRUCTURE OF CATALYST LAYERS

2.1 Introduction

Much effort has gone into developing new electrode materials for use in polymer electrolyte fuel cells (PEMFCs). Current trends of research include investigation of high surface area, novel ordered nanoporous carbons[23] and carbon nanotube-based catalyst supports[141], as well as carbon-free catalyst supports,[27,140] and thin film catalyst layers.[96,142] Presently, conventional catalyst layers employing Pt deposited on high surface carbon black supports, with the addition of a proton conducting phase, are most commonly used. Successful development of novel materials for CLs is hindered by a lack of fundamental understanding of the complex, multi-component nature of the CL, the interplay of its components, and their independent and co-operative effects on effective properties, particularly in the context of preparing catalyst coated membranes (CCMs).

Carbon-supported catalysts have been widely used in a variety of industrial applications because of their high surface area, onto which fine dispersions of metal particles can be deposited. The supports are relatively stable to a range of conditions and allow for easy recycling of the metal by burning off carbon. Three forms of carbon are commonly used as supports for precious metals: activated carbon, carbon black and graphitized carbon. Carbon blacks, such as Ketjen Black and Vulcan XC-72, are current technological standard catalyst supports for

fuel cells applications. Carbon blacks are manufactured by pyrolysis of hydrocarbons such as natural gas or aromatic residues of petroleum processing.[32,34] Carbon blacks are known for their tendency to form chain-like aggregates. The higher the degree of aromaticity of the feedstock, the higher is the degree of aggregation. Carbon blacks with specific area ranging from 8 to 1500 m^2/g can be produced.[32]

A significant contribution to understanding the nature of the CLs was made by Ridge et al.[87] presenting the agglomerate structure model for Teflon-bonded Pt-black electrode, which since has been adopted for Pt/carbon/ electrolyte electrodes and developed further by Springer et al,[143] Broka et al,[144] Eikerling et al[82,145] and others. The model suggests formation of agglomerates that are covered with ionomer; intra-agglomerate pores are filled with water. The experimental work of Uchida et al.,[9,86] which indicate formation of carbon particle agglomerates exhibiting a bimodal pore size distribution, is indispensable. This includes: 6 – 20 nm sized pores within agglomerates of carbon particles and larger 20 – 100 nm sized pores that exist between aggregates of agglomerates. Within the fuel cell scientific community, these are often referred to as primary and secondary pores. Ionomer is believed to be distributed within the secondary pores, forming a complex three-dimensional network. However, there also exists a < 2 nm pore structure in the primary carbon particle, the function of which in fuel cell electrochemical reaction has not been clearly determined yet.

In this chapter, a study of the microstructure of carbon supports, carbon-supported Pt catalysts, and 3-component Pt/carbon/ionomer catalyst layers by

TEM, SEM and N_2 adsorption is reported. Two types of carbon support are chosen for investigation, Ketjen Black and Vulcan XC-72; Pt/carbon composite with constant Pt loading and Pt/carbon/ionomer composite CLs with a range of perfluorosulfonate ionomer loadings are investigated to determine the effect of Pt and the ionomer on the resultant microstructure of the CL. The microstructure is described in terms of pore size distribution (PSD), pore volume and surface areas of the pores. The terminology used throughout this work for micro-, meso-, and macropores is that adopted by IUPAC.[118,119] Pores < 2 nm are termed micropores and ascribed to the pores within the carbon primary particles. Pores in the range of 2 – 50 nm are referred to as mesopores, and the pores larger than 50 nm are termed macropores. Pores larger than 2 nm are assumed to be found within the complex agglomerate-aggregate organization of the primary particles.

Nitrogen gas adsorption was chosen over the alternative popular technique of characterization of porous media, mercury porosimetry, because of the pore range of interest. Nitrogen adsorption is implemented to study pores of sizes between several Å to ~ 100 nm, whereas mercury porosimetry cannot be employed for pores < 10 nm due to very high intrusion pressures that have to be applied, which are likely to destroy the porous structure. Moreover, mercury porosimetry is not optimal for compressible materials, such as carbon and Nafion, and is a destructive technique in contrast to N_2 adsorption.

2.2 Experimental

2.2.1 Materials

Ketjen Black carbon and Vulcan XC-72 carbon were received from Tanaka Kikinzoku Kogyo (TKK) and Cabot Corp., respectively. Catalyst powders with 46 wt% Pt on Ketjen Black (TEC10E50E, lot numbers 107-1701 and 108-2021) and Vulcan XC-72 (TEC10V50E, lot number 106-3041) were received from Tanaka Kikinzoku Kogyo. Catalyst inks for spray deposition were prepared by mixing catalyst powder, Pt/carbon (Pt/C), in water and methanol mixture (1:1), corresponding to 0.70 g Pt/C in 100 g of water/methanol solution. The dispersion was sonicated for 30 min, while adding dropwise 0.74, 1.6, 6.0, and 14 g of 5 wt% Nafion solution (Alfa Aesar) to the mixture to produce 5, 10, 30, and 50 wt% ionomer loadings, respectively. The final mixture was sonicated at room temperature for 2 h.

All CLs comprising of Pt, carbon and ionomer were fabricated by spray-deposition on Nafion 211 membrane, which was used as received, producing CCMs with CL deposited on both sides. Spray deposition of the ink on Nafion 211 membrane was performed at 80 °C. CLs with 5, 10, 30 and 50 wt% of ionomer were prepared corresponding to 0.1, 0.2, 0.8, and 1.8 ionomer to carbon dry weight ratios (I/C ratios). Carbon and Pt loadings in all CLs were held constant at 0.475 mg/cm^2 and 0.4 mg/cm^2, respectively.

2.2.2 Methods

Transmission electron microscopy (TEM)

For the analysis of Ketjen Black and Vulcan XC-72 carbon powders a Hitachi H7600 transmission electron microscope was employed. Carbon powders were dispersed in a mixture of water and methanol (50:50) and dropped onto polymer coated (Formvar) 200 mesh copper grids. The solution was allowed to dry and the samples were imaged with an accelerating voltage of 80 kV.

Scanning electron microscopy (SEM)

For analysis of Ketjen Black and Vulcan-based CLs with a range of ionomer loadings, a Hitachi S-3500N scanning electron microscope was employed. CL samples were prepared by freezing the CCMs in liquid nitrogen followed by fracturing. A thin layer of gold (< 10 nm) was vacuum sputtered onto the samples to ensure adequate electrical conductivity. Samples were typically imaged at an accelerating voltage of 20 kV.

Nitrogen adsorption

N_2 physisorption experiments were performed at 77 K on a 3100 Surface Area Analyzer (Beckman Coulter™). N_2 gas of ultra-high purity 99.999 % was used. Carbon and Pt/carbon samples of ~100 mg were degassed at 160 °C for 12 h prior to the adsorption experiment. 50 cm^2 CCMs were cut into thin strips, placed in the sample tube and degassed for 12 h at 105 °C. Adsorption experiments were performed immediately after degassing. A blank adsorption experiment on Nafion 211 membrane was performed for the case of CCMs. It

was found that Nafion 211 absorbed ~ 3 cm^3/g of N_2 at 0.98 (STP), contributing negligibly to the total amount of gas adsorbed by a CCM. Adsorption isotherms of Pt/carbon powders and CCMs were all re-plotted after normalizing to the carbon content in each sample. The BET surface area was calculated from the BET equation by plotting the left-hand side term of the equation against P/P_0 in the range 0.05 to 0.2 P/P_0 as described in Section 1.6.1. The total pore volume was found at a partial pressure of 0.98 P/P_0 (STP) by converting to liquid nitrogen volume using the conversion factor of 0.001547, under the assumption that the density of condensed nitrogen in the pores is equal to the density of bulk liquid nitrogen.[146] Pore size distributions (PSDs) were calculated using the Barret – Joyce – Halenda (BJH) method.

2.3 Results and Discussion

2.3.1 Carbon powders

In principle, all pores larger than the molecular diameter of nitrogen (3.5 Å) can be detected by the N_2 adsorption technique. The physical adsorption in micropores[118,119] (< 2 nm) that is observable at very low gas partial pressures (< 0.01 P/P_0) is described by the theory of micropore filling.[147-149] Adsorption in these pores occurs through volume filling, with the adsorption enthalpy strongly enhanced by the overlap of adsorption forces from the opposite walls of the pore; i.e., neither mono-/multilayer adsorption nor capillary condensation takes place. Concurrent with the filling of micropores, adsorption of a monolayer of nitrogen occurs on the pore walls of meso- and macropores (> 2 nm) and on the external surface of particles. Although it is difficult to distinguish between these concurrent

processes, the consensus is that the steeper the rise in the adsorption isotherm at these very low partial pressures, the larger is the total volume of micropores.[120,150]

As the partial pressure is increased, monolayer formation evolves into multilayer formation until the pore radius related to the capillary condensation at a given partial pressure is reached. Thus, at medium and high partial pressures, two processes may occur simultaneously: multilayer formation and capillary condensation. At a partial pressure close to unity, either all pores are filled with nitrogen and the isotherm reaches a plateau because the saturation point is reached, or multilayer formation continues in macropores and no saturation point in the isotherm is observed. The latter situation is characteristic for aggregate-type systems that possess macropores between agglomerates, such as carbons.

Sorption and desorption isotherms for Ketjen Black and Vulcan XC-72 carbons are shown in Figure 2.1. Both isotherms are type II according to IUPAC classification.[118,119] Type II isotherms are characteristic of systems containing micropores as they exhibit a strong interaction between adsorbate and adsorbent that results in a steep rise in the isotherm under low partial pressures. No saturation is observed at partial pressures close to unity providing evidence for the presence of macropores. This result is interpreted as an indication of the presence of large aggregates of particles.

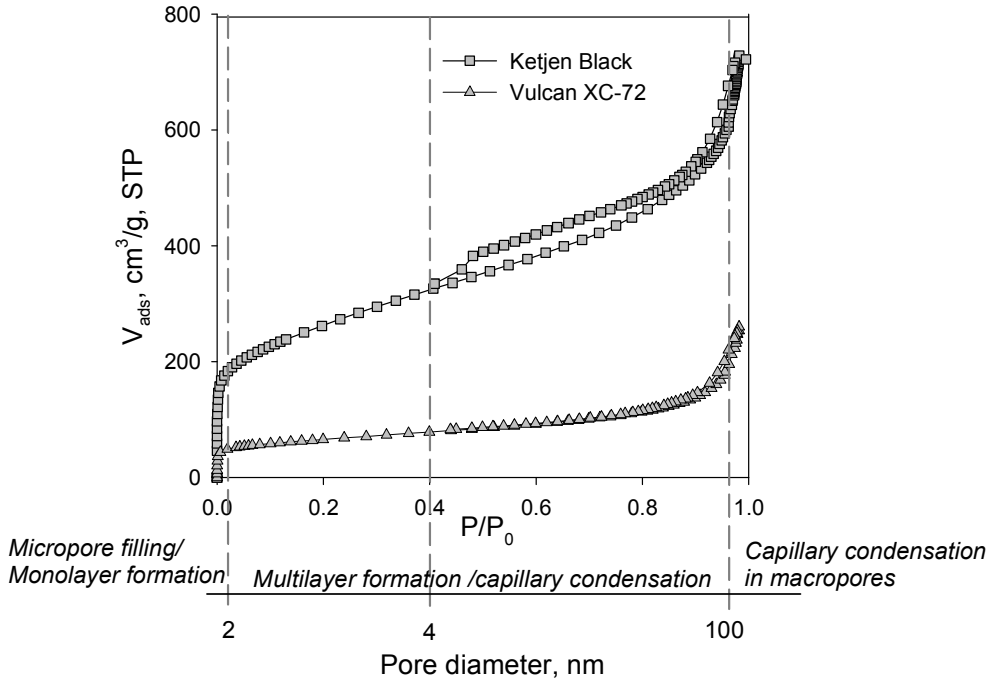

Figure 2.1: N_2 adsorption isotherms for Ketjen Black (squares) and Vulcan XC-72 (triangles) carbon supports. The secondary x-axis indicates pore size and regions of the isotherm characterized by different adsorption mechanisms.

It is difficult to deconvolute unambiguously the microstructure of carbon blacks and the arrangement of primary carbon particles into agglomerates, and then further deconvolute aggregates of agglomerates. However, it is reasonable to assume that the micropore filling process (i.e., filling of < 2 nm pores) occurs in the primary carbon particles, which themselves are ~ 30 nm in diameter.[32,82] The micropores are thought to exist either between the turbostratic graphite planes of the crystallites or in between edges of two crystallites. The primary carbon particles arrange into 100 – 300 nm diameter agglomerates. Within these

agglomerates, mesopores of 2 – 20 nm diameter exist. Agglomerates coalesce into chain-like aggregates, and a continuous network of pores, > 20 nm, is formed in the interstices. Shown in Figure 2.2 is a depiction of carbon black particles, agglomerates of particles, and aggregates of agglomerates; the corresponding micro-, meso, and macropores formed by these structures are indicated by arrows.

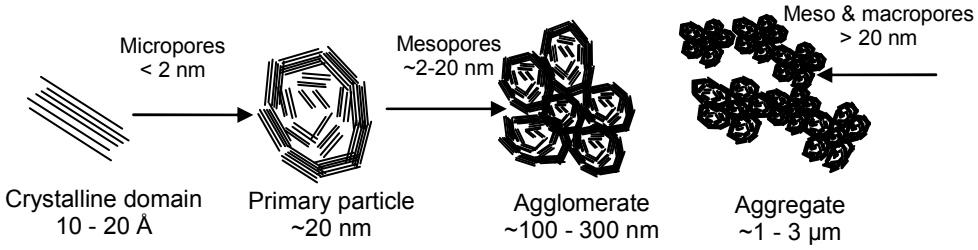

Figure 2.2: A schematic representation of microstructures of carbon blacks: turbostratic crystalline domain, primary carbon particle, agglomerate, and aggregate of agglomerates. Representative micropores, mesopores, and macropores are indicted by arrows (reproduced from ACS Appl. Mater. Interfaces 2, 375, 2010 by Soboleva with permission).

In Figure 2.3, TEM images of carbon powders are shown, where it can be seen that carbon primary particles coalesce into spherical-like agglomerates of ~ 200 nm, which further aggregate into larger entities of several micrometers creating an extensive porous network. A similar type of particle aggregation is observed for Ketjen Black and Vulcan XC-72, however larger aggregates tend to be formed in the Ketjen Black case.

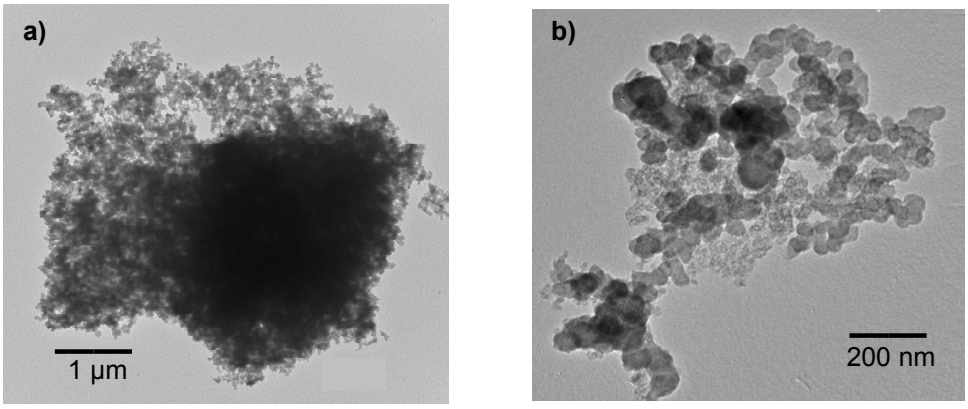

Figure 2.3: TEM micrographs of a) Ketjen Black carbon and b) Vulcan XC-72 carbon aggregates.

Both Ketjen Black and Vulcan XC-72 carbons show hysteresis in their adsorption isotherms, but it is more pronounced for Ketjen Black and extended to a wider range of partial pressures, reaching the hysteresis closure partial pressure at 0.4 P/P_0. The partial pressure of the hysteresis closure is attributed to the tensile strength of the liquid adsorbate since it is assumed that N_2 condenses in pores at 77 K and possesses bulk properties of liquid nitrogen. For nitrogen, independent of the nature of adsorbent, the partial pressure of 0.4 is found to be the critical pressure.[127] Both hysteresis curves are H3 type according to the IUPAC classification, which is characteristic of aggregates of plate like particles giving rise to slit-shaped pores, and is common for carbonaceous materials.[124,125] The pronounced hysteresis in case of Ketjen Black carbon implies the presence of a more extensively-developed pore network wherein the fraction of larger pores trapped within the network of smaller pores is much higher.[151-154] This is consistent with the fact that Ketjen Black possesses a large fraction of micropores and pores < 20 nm, and a broad pore size distribution, as will be

illustrated later. The calculated BET surface area was found to be 890 ± 64.3 m^2/g for Ketjen Black and 228 ± 3.57 m^2/g for Vulcan XC-72, estimated in the range of partial pressures 0.05 – 0.2 P/P_0. The total pore volumes, calculated at a partial pressure of 0.98 P/P_0, are 1.02 ± 0.15 cm^3/g and 0.40 ± 0.02 cm^3/g, respectively.

The pore size distributions (PSDs) of both types of carbon are estimated from the adsorption branch of the isotherms and are shown in Figure 2.4. The adsorption branch is assumed to be free of pore network effects, as opposed to the desorption branch,[120] which will be discussed later in the section. PSD curves are very similar in shape with the PSD maxima at ~ 55 nm, however they differ significantly in the total pore volume, especially in the micro-to-mesopore region (2 – 20 nm) where Ketjen Black carbon adsorbs a notably larger amount of N_2.

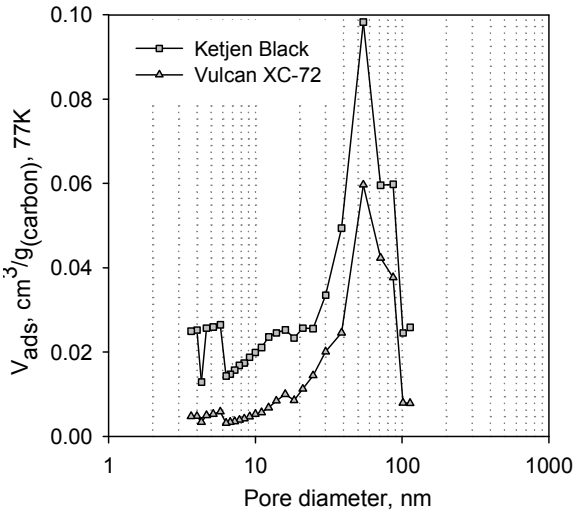

Figure 2.4: Pore size distribution curves for Ketjen Black (squares) and Vulcan XC-72 (triangles) (reproduced from ACS Appl. Mater. Interfaces 2, 375, 2010 by Soboleva with permission).

The same trend in the shape of the isotherm and the amount of N_2 adsorbed is seen in Pt/carbon powders (see Figure 2.5). Pt/Vulcan powder, exhibiting a BET surface area of 228.7 ± 0.657 m^2/g, possesses only ~ 1/3 the sorption capacity of Pt/Ketjen powder, which has a BET surface area of 639.2 ± 26.16 m^2/g.

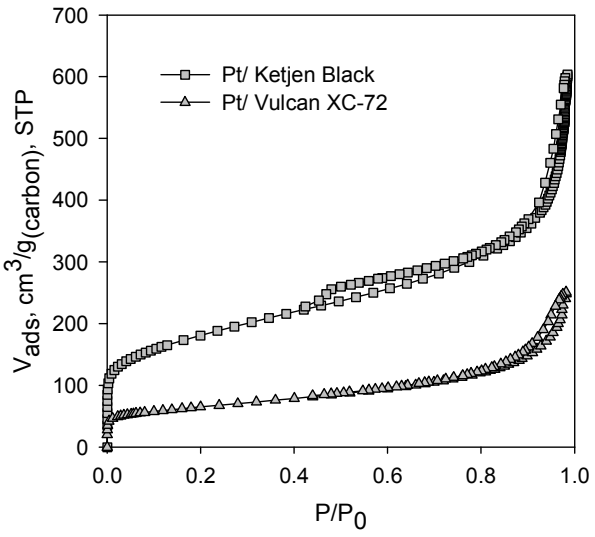

Figure 2.5: N_2 adsorption isotherms for Pt/Ketjen Black (squares) and Pt/Vulcan XC-72 (triangles) catalyst powders.

In both cases, the shape of CCM isotherms and hysteresis loops are identical to those of the native carbon powders. The hysteresis is observed in the range of 0.4 to 1.0 P/P_0 in the case of Ketjen Black support and only at pressures above 0.8 for Vulcan XC-72 support.

The Harkins – Jura equation (1.16) was used to determine the t-thickness values over the entire range of partial pressures, and subsequently used to determine the microporosity of the carbons by re-plotting the adsorption isotherms as a t-plot, i.e., a plot of the quantity of adsorbed N_2 against t, [120,125,128,155] Figure 2.6.

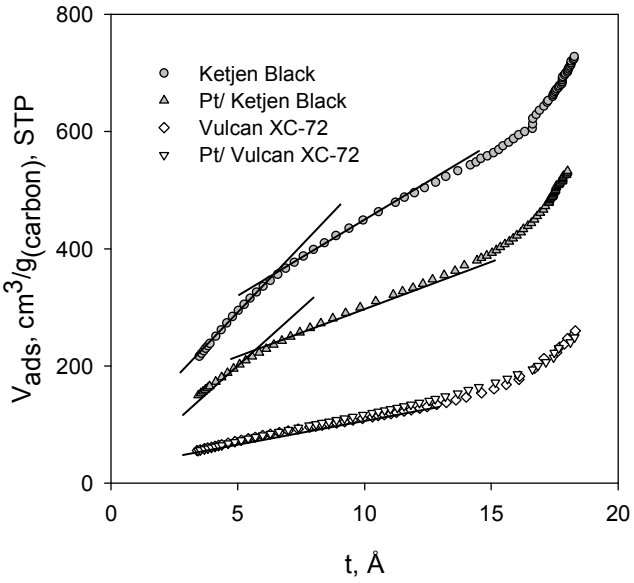

Figure 2.6: t-plots for Ketjen Black and Vulcan XC-72 carbon supports and corresponding Pt/ carbon supported catalyst powders. Ketjen Black (circles), Pt/Ketjen Black (triangles), Vulcan XC-72 (diamonds), and Pt/Vulcan (triangles). Linear regions are used for t-plot analysis (reproduced from ACS Appl. Mater. Interfaces 2, 375, 2010 by Soboleva with permission).

Two linear regions with differing slopes can be distinguished in the t-plots of Ketjen Black support and Pt/Ketjen catalyst powder. The first region of steeper gradient is observed between 3.5 Å – 5 Å; the second linear extends from 5 Å to ~ 10 Å. This observation suggests that there are two different adsorption phenomena within the pores: one corresponding to dimensions of one or two molecular diameters; and the other associated with pores larger than two molecular diameters but smaller than the diameter required for capillary condensation, which is ~ 20 Å. This can be explained in the context of micropore filling and the increased adsorption strength exerted by the pore surface on the gas molecule. A single gas molecule in a pore of similar diameter would

experience enhanced adsorption forces from both walls of the pore. Van der Waals diameter of N_2 molecule is 3.10 Å.

In sharp contrast, only one linear region with constant slope can be distinguished for t-plots corresponding to Vulcan XC-72 and its Pt-deposited analogue. The intercept of the linear region with the y-axis allows the volume of the micropores to be estimated, the results are shown in Table 2.1.

Table 2.1: Microstructural characteristics of carbon supports and Pt/carbon catalyst powders determined from N_2 adsorption isotherms.[a]

Carbon type	BET $SA_{(total)}$, $m^2/g_{(carbon)}$	$SA_{(>2nm)}$, $m^2/g_{(carbon)}$	$SA_{(<2nm)}$, $m^2/g_{(carbon)}$	$Vpore_{(total)}$, $cm^3/g_{(carbon)}$	$Vpore_{(<2nm)}$, $cm^3/g_{(carbon)}$
Ketjen Black	890.6 ± 64.26	409.1 ± 19.46	481.5 ± 61.24	1.02 ± 0.15	0.25 ± 0.03
Pt/ Ketjen Black	639.2 ± 26.16	294.1 ± 19.60	345.2 ± 17.32	0.86 ± 0.06	0.18 ± 0.02
Vulcan XC-72	227.7 ± 3.570	114.7 ± 1.930	113.0 ± 3.000	0.40 ± 0.02	0.06 ± 0.002
Pt/ Vulcan XC-72	228.7 ± 0.657	132.5 ± 13.15	96.19 ± 13.13	0.39 ± 0.003	0.05 ± 0.01

a BET SA was determined in the range of 0.05 - 0.2 N_2 partial pressure; volume of micropores was determined from the intercept of the t-plot; total pore volume from total adsorbed gas amount at 0.98 partial pressure; surface area (SA) of mesopores from the slope of t-plot; SA of micropores as difference between total SA and mesopores SA.

From the table it can be seen that pores of size < 2 nm constitute ~ 25 % of the total pore volume in Ketjen Black carbon, whereas in the case of Vulcan XC-72 they constitute ~ 15 %. From the BET surface area and t-plot analysis, it appears that the deposition of Pt significantly decreases the total detectable surface area of the Ketjen Black carbon support from 890 m^2/g for Ketjen Black to 639 m^2/g for Pt/Ketjen. The volume of micropores (< 2 nm) after Pt deposition

decreases by 30% in case of the Ketjen Black support. Total surface areas and pore volumes of Vulcan carbon and Pt/Vulcan are similar indicating that the deposition of Pt does not affect these microstructural properties: 228 m^2/g for Vulcan XC-72 and 229 m^2/g for Pt/Vulcan; 0.40 ± 0.02 cm^3/g for Vulcan XC-72 and 0.06 ± 0.002 cm^3/g for Pt/Vulcan, Figure 2.7.

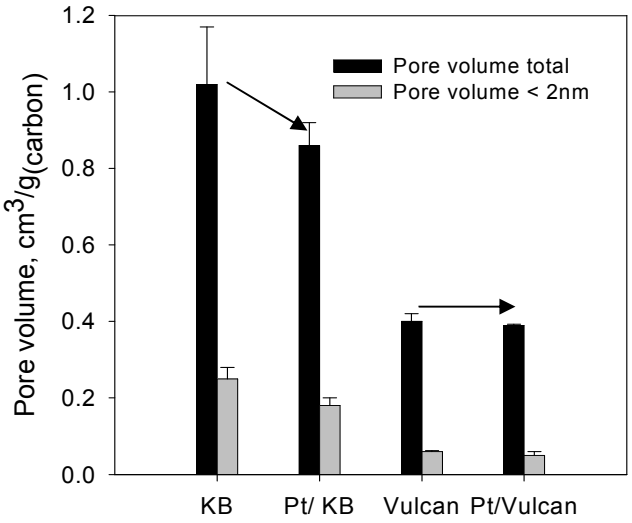

Figure 2.7: Total pore volume and micropore volume of carbon powders and Pt/carbon powders (reproduced from ACS Appl. Mater. Interfaces 2, 375, 2010 by Soboleva with permission).

The changes in the micropore filling volume after deposition of Pt onto the carbon supports were examined by plotting sorption isotherms in the logarithmic scale so that the low pressure region is accentuated, as shown in Figure 2.8. Ketjen Black carbon support adsorbs ~ 59 cm^3/g (STP) at a N_2 partial pressure of 10^{-4}. However, for Pt/Ketjen, the amount adsorbed at this pressure decreased by 25% to 45 cm^3/g (STP) after normalizing to carbon content. In the case of Vulcan XC-72, the volume associated with micropore filling is only 11 cm^3/g (STP) at a

partial pressure of 10^{-4}, i.e., significantly lower than Ketjen Black carbon. Furthermore, after normalizing to carbon content, isotherms of Pt/Vulcan and Vulcan XC-72 carbon coincide indicating no change in micropore volume upon Pt deposition on Vulcan support.

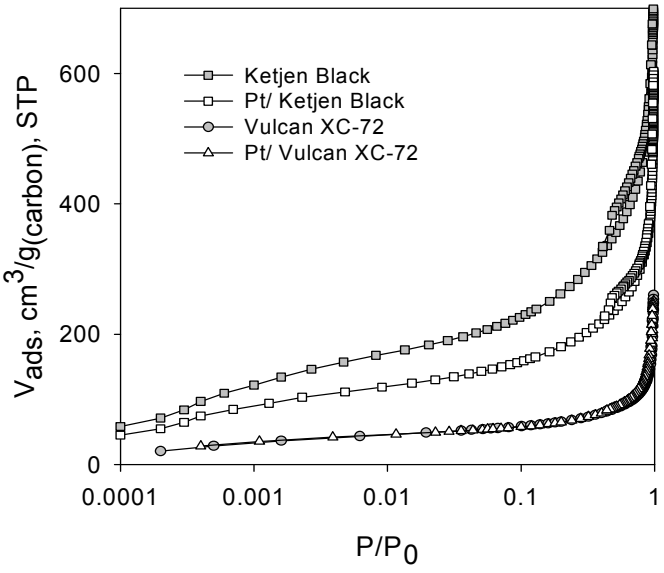

Figure 2.8: N_2 adsorption isotherms for Ketjen Black carbon support, Pt/Ketjen catalyst powder, Vulcan XC-72 carbon support, and Pt/Vulcan catalyst powder (reproduced from ACS Appl. Mater. Interfaces 2, 375, 2010 by Soboleva with permission).

These results are interpreted as blocking of the micropores of Ketjen Black support upon deposition of Pt particles. It is speculated that particles block the entrance of these micropores (< 2 nm). It is suggested that edge-sites of crystallites, that form the necks of micropores, serve as adsorption sites for Pt particles because of their high reactivity. Due to the size relation between the micropores (< 2 nm) and Pt particles (2 – 4 nm)[83] it is unlikely that Pt particles are deposited inside the micropores. In the case of Vulcan XC-72 carbon, where

the fraction of micropores is less significant, this phenomenon is not observed. TEM images of Pt/Ketjen Black and Pt/Vulcan illustrating Pt distribution on carbon particles are shown in Appendix A. However, it is very difficult to determine location of Pt particles on the surface of the carbon particle or in the neck of the micropores from these micrographs.

2.3.2 3-Component Catalyst Coated Membranes (CCMs)

Scanning Electron Microscopy (SEM)

In Figure 2.9 and Figure 2.10, SEM images of catalyst coated membranes with Ketjen Black and Vulcan-based CLs with identical carbon and Pt loading and a range of ionomer loadings are shown. The pictures show three layers of the MEAs. The dark central area is Nafion 211 membrane, the bright areas are the Pt containing CLs. It is seen that the CLs are relatively uniform with slight variation in thickness throughout the layer. The 5 wt% ionomer CLs seem to be loose, whereas 50 wt% ionomer CL are very compact. This is due to the binding properties of ionomer in the CL. With increasing ionomer content the catalyst layers become more dense, and 50 wt% ionomer CLs were found to be thinner than 5 and 30 wt% ionomer CLs. Thickness of the catalyst layers containing 50 wt% ionomer was 9.6 and 9.0 μm for Ketjen Black and Vulcan-based CLs, respectively. Catalyst layers of 15.3 and 10 μm thickness were formed by Ketjen Black and Vulcan-based CLs containing 5 wt%, respectively.

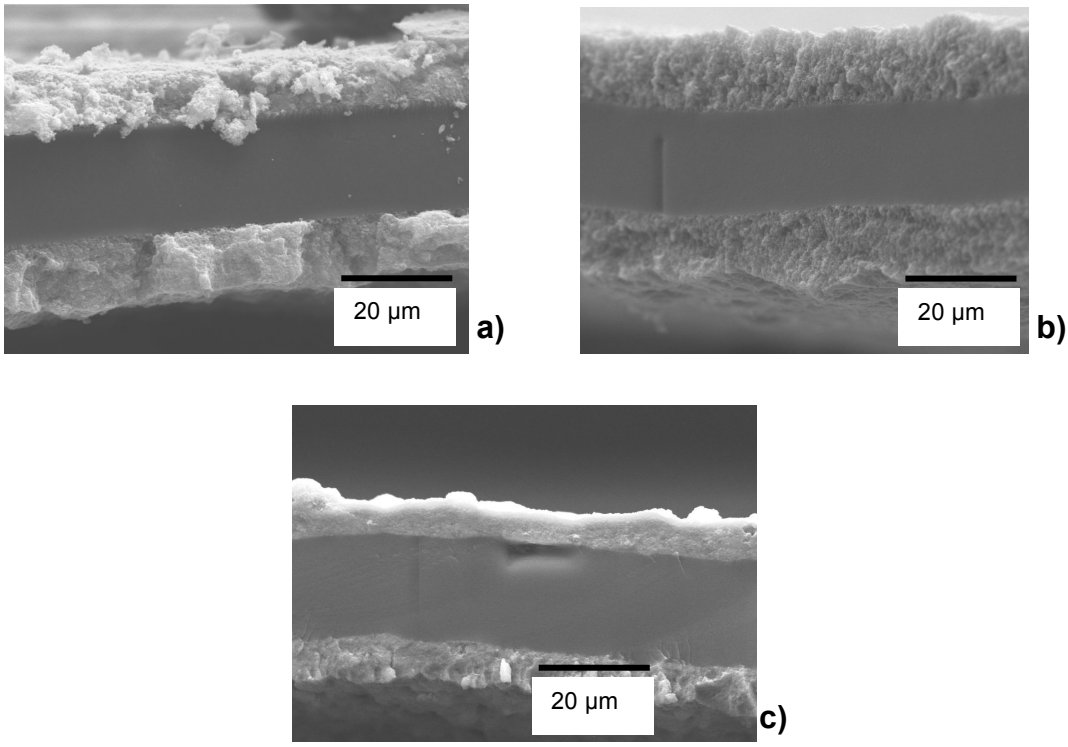

Figure 2.9: SEM images of catalyst coated membranes comprised of Ketjen Black-based catalyst layers with a) 5 wt%, b) 30 wt%, and c) 50 wt% ionomer loading.

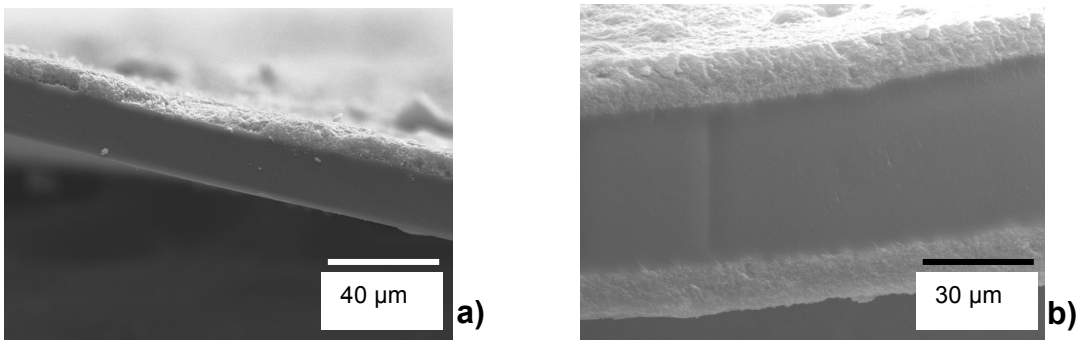

Figure 2.10: SEM images of catalyst coated membranes with Vulcan-based catalyst layers with a) 5 wt%, and b) 50 wt% ionomer loading.

Vulcan-based CLs seem to produce slightly denser CLs than Ketjen Black-based ones, and with a smoother surface, as it is seen from Figure 2.11. The

roughness of the Ketjen Black-based CLs is attributed to relatively larger aggregates formed by Pt/Ketjen Black (~ 4 – 5 μm diameter) compared to Pt/Vulcan aggregates (~ 1 μm diameter) as observed by TEM and shown in Figure 2.3. The larger the aggregates, the rougher the surface of the catalyst layer. Void spaces, cracks and pores, of micrometer size are distinct in Ketjen Black 50 wt% ionomer CL as opposed to the Vulcan 50 wt% ionomer CL as shown in Figure 2.11.

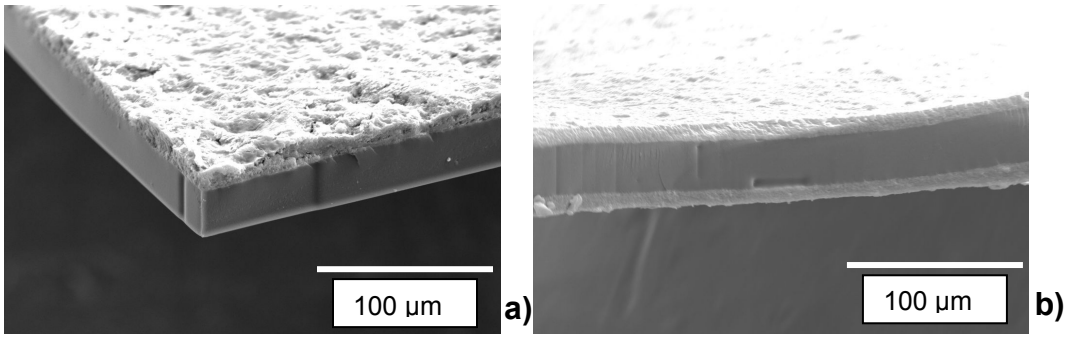

Figure 2.11: SEM images of the CL surface for a) Ketjen Black 50 wt% ionomer and b) Vulcan 50 wt% ionomer CLs.

Nitrogen Adsorption

Isotherms of catalyst layers were examined in the form of catalyst coated membranes (CCMs). Sorption isotherms of CCMs and the associated hysteresis loops are similar in shape to the corresponding Pt/carbon powder isotherms; but differ significantly in the amount of gas adsorbed, as shown in Figure 2.12a, b.

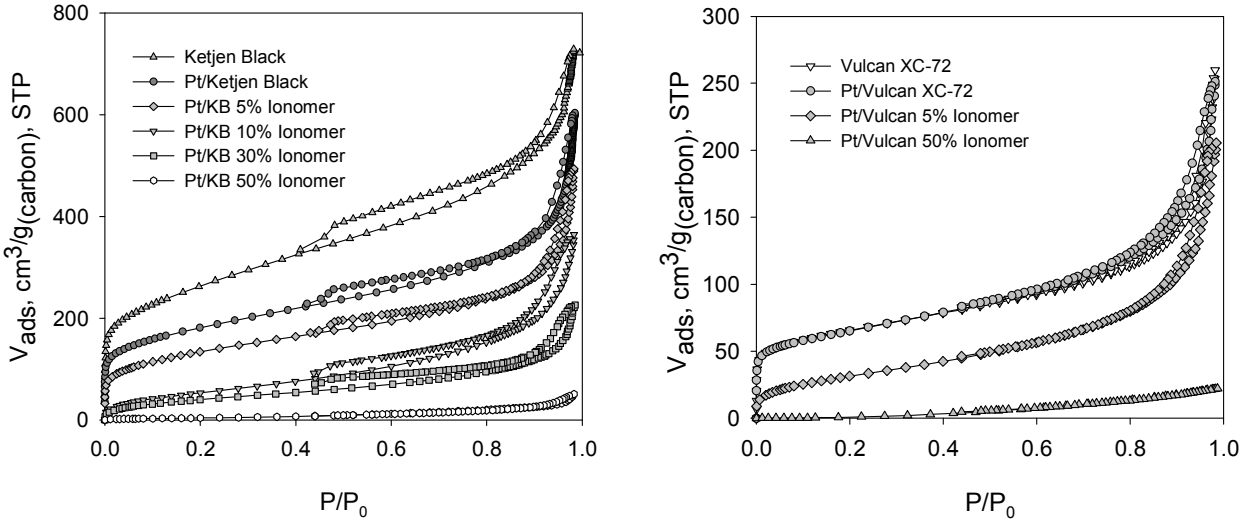

Figure 2.12: a) N_2 adsorption isotherms of Ketjen Black supported CLs with 5, 10, 30, and 50 wt% ionomer. Isotherms for Ketjen Black and Pt/Ketjen Black are shown for reference. b) N_2 adsorption isotherms for Vulcan XC-72 supported CLs containing 5 and 50 wt% ionomer; Vulcan XC-72 and Pt/Vulcan XC-72 isotherms are shown for reference (reproduced from ACS Appl. Mater. Interfaces 2, 375, 2010 by Soboleva with permission).

Virtually all the N_2 is adsorbed by the catalyst layer of the CCM because the contribution from Nafion 211 is negligible (refer to section 2.2). According to IUPAC classification, isotherms for the CCMs exhibit typical Type II behaviour with a rapid uptake in the macropore region that can be interpreted as evidence for the presence of large aggregates of particle agglomerates in the CL. As the ionomer loading in the CL is increased, the amount of adsorbed N_2 decreases, shifting isotherms downwards. This indicates a loss of total pore volume in the CL with increasing ionomer content. Hystereses show type H3 characteristics, consistent with that of carbon supports. In the case of Ketjen Black-based CLs, hysteresis is strongly pronounced over the entire range of partial pressures down

to 0.4 P/P_0, as it is in the native catalyst powder. In the case of Vulcan-based CLs, a hysteresis similar to the Pt/Vulcan powder is seen in the CCM with 5 wt% ionomer. Based on the shapes of hystereses and PSD curves it is speculated that addition of ionomer *does not affect the inherent agglomeration/aggregation characteristics of the Pt/carbon*; ionomer distributes on the pre-formed porous carbon framework covering and filling the pores according to Figure 1.5 The total BET surface area of CLs, total pore volume, volume and surface areas of micro- and mesopores are estimated as described in section 2.2. t-Plots and PSD curves for Ketjen Black-based CLs containing 5, 10, 30, and 50 wt% ionomer and Vulcan XC-72-based CLs containing 5 and 50 wt% ionomer are shown in Figure 2.13 and Figure 2.14, and the results summarized in Table 2.2 and Figure 2.15.

Table 2.2: Microstructural characteristics of catalyst layers (CLs) [a,b]

Carbon type	Ionomer loading, wt%	BET $SA_{(total)}$, $m^2/g_{(carbon)}$	$SA_{(>2nm)}$, $m^2/g_{(carbon)}$	$SA_{(<2nm)}$, $m^2/g_{(carbon)}$	$Vpore_{(total)}$, $cm^3/g_{(carbon)}$	$Vpore_{(<2nm)}$, $cm^3/g_{(carbon)}$
KB	5	501.6 ± 29.00	209.3 ± 22.45	292.3 ± 18.34	0.70 ± 0.13	0.11 ± 0.02
KB	10	206.8 ± 19.55	183.5 ± 1.816	23.33 ± 19.55	0.46 ± 0.09	0.02 ± 0.01
KB	30	137.1 ± 21.40	130.1 ± 0.119	6.21 ± 21.4	0.35 ± 0.01	-
KB	50	24.9 ± 3.43	26.06 ± 0.695	-	0.08 ± 0.01	-
Vulcan	5	114.6 ± 5.616	119.5 ± 6.709	-	0.33 ± 0.05	-
Vulcan	50	24.8 ± 0.55	24.8 ± 0.55	-	0.02 ± 0.001	-

a Pt loading is 0.4 mg/cm^2 in all CLs. b BET surface area (SA) was determined in the range of 0.05 -0.2 N_2 partial pressure; total pore volume from total adsorbed gas amount at 0.98 N_2 partial pressure; volume of micropores from the intercept of the t-plot; surface area of mesopores from the slope of the t-plot; surface area of micropores as difference between total SA and mesoporous SA.

The volume of micropores was calculated using the intercept of the t-plot with the ordinate, however, in case of 30 and 50 wt% Pt/Ketjen/ionomer and 5 and 50 wt% Pt/Vulcan/ionomer samples, the intercepts are negative indicating the absence of detectable micropores. Surface area of mesopores (> 2 nm diameter) in Pt/Ketjen CLs containing 30 and 50 wt% ionomer calculated from the t-plots approach the total BET surface area values estimated from the BET plots indicating absence of the detectable micropores. In the case of Pt/Vulcan at 5 and 50 wt% ionomer contents, the total BET surface areas are equal to the surface areas of mesopores estimated from the t-plots.

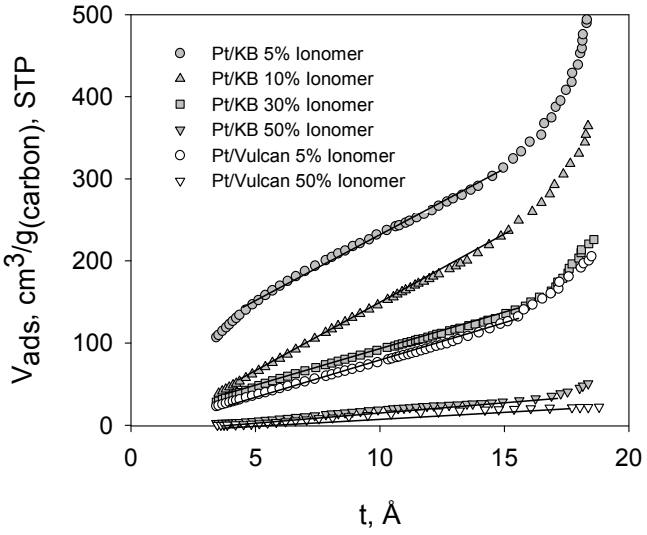

Figure 2.13: t-plots for Ketjen Black supported CLs containing 5, 10, 30 and 50 wt% ionomer, and of Vulcan XC-72 supported CLs containing 5 and 50 wt% ionomer. Linear regions were used to determine micropore volume and mesoporous surface area (reproduced from ACS Appl. Mater. Interfaces 2, 375, 2010 by Soboleva with permission).

With the addition of 10 wt% ionomer in the Pt/Ketjen catalyst layer, the volume of the micropores decreases from an initial 0.18 cm^3/g for the catalyst powder to 0.02 cm^3/g for the catalyst layer. In the case of Pt/Vulcan catalyst layer, the small initial volume of micropores in the catalyst powder, 0.05 cm^3/g, was found to disappear after the addition of just 5 wt% of ionomer, as shown in Table 2.2. The clear trend in the loss of micro – mesopore volume in Pt/Ketjen-based CLs with increasing ionomer content is seen in the PSD curves shown in Figure 2.14a. Mesoporous volume (2 – 20 nm), which corresponds to pore volume within agglomerates, asymptotically decreases with addition of ionomer; whereas in the macroporous region, i.e., pores > 50 nm, a drastic decrease in pore volume is observed only after the addition of 50 wt% ionomer, when larger pores also become filled with ionomer. In the case of Pt/Vulcan-based CLs, addition of 50 wt% ionomer causes a complete loss of porosity over the entire PSD range. These findings are in contrast to the observations of Uchida's group who report that the primary pore volume within agglomerates remains unchanged with increasing ionomer content, whereas the volume of secondary pores (meso- and macropores) decreases.[9,86] The discrepancy in findings is attributed to different experimental methods used to analyse CL microstructure.

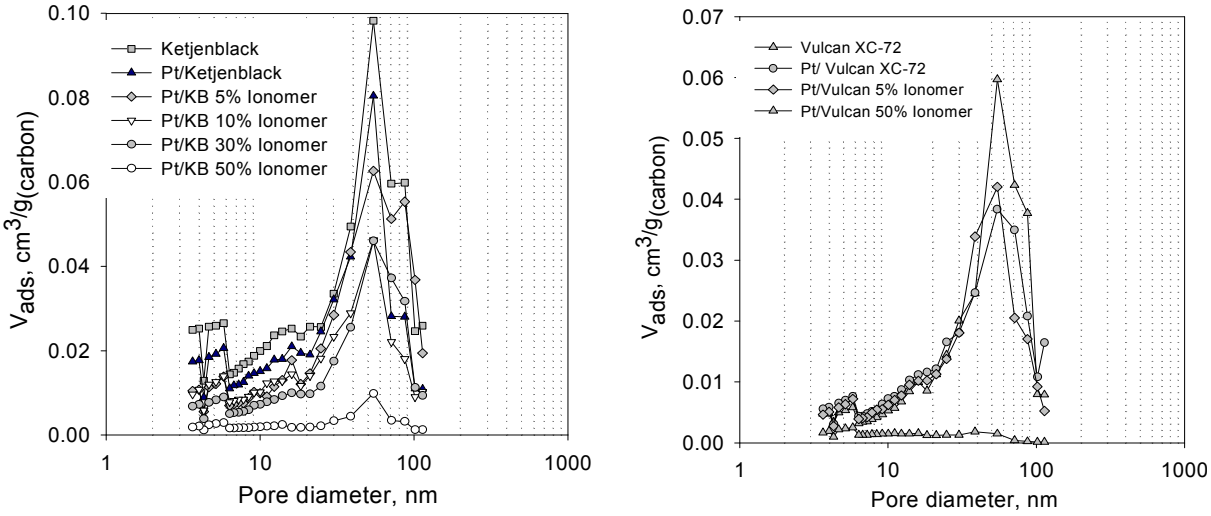

Figure 2.14: a) Pore size distribution curves for Ketjen Black supported CLs showing the effect of CL ionomer loading on pore volume and PSD of the CLs. PSD of Ketjen Black support and Pt/Ketjen Black are shown for reference. b) Pore size distribution curves for Vulcan XC-72 supported CLs showing the effect of CL ionomer loading on pore volume and PSD of the CLs. PSD of Vulcan XC-72 support and Pt/ Vulcan are shown for reference (reproduced from ACS Appl. Mater. Interfaces 2, 375, 2010 by Soboleva with permission).

Summarized structural data of Ketjen Black and Vulcan XC-72 carbons, Pt/carbon and Pt/carbon/ionomer systems are depicted in Figure 2.15.

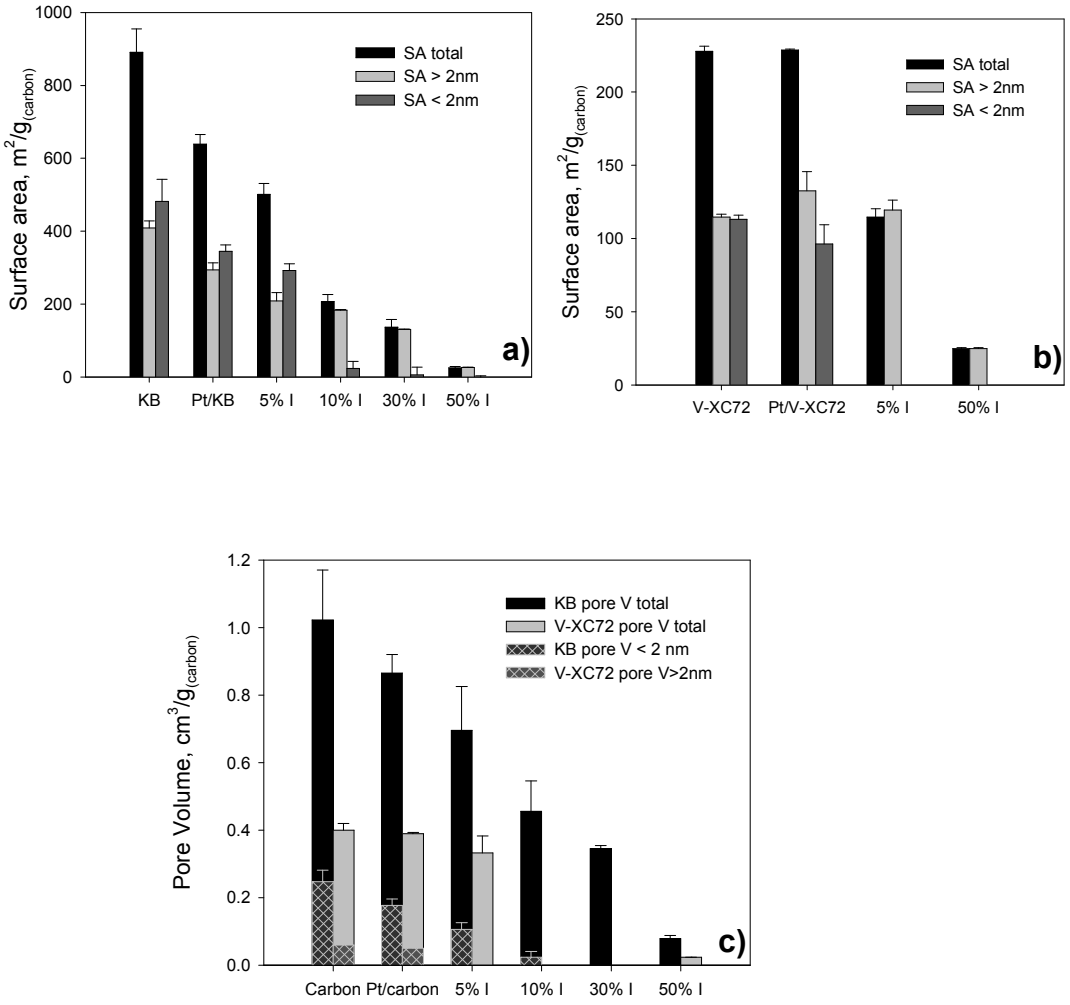

Figure 2.15: a) Surface areas of Ketjen Black, Pt/Ketjen Black and the corresponding CLs showing the effect of Pt and ionomer loading on detectable surface area of the examined systems. b) Surface areas of Vulcan XC-72, Pt/Vulcan XC-72 and corresponding CLs showing the effect of Pt and ionomer loading on detectable surface area of the examined systems. c) Total pore volume (plain bars) and micropore volume (checked bars) of Ketjen Black (black bars) and Vulcan XC-72 (gray bars) carbons, Pt/carbon and the corresponding CLs (reproduced from ACS Appl. Mater. Interfaces 2, 375, 2010 by Soboleva with permission).

Based on these findings it is postulated that at very low ionomer content (5 – 10 wt%), *ionomer exists in the meso/macroporous void space formed between agglomerates of carbon particles*, presumably being distributed on the surface of agglomerates. Nitrogen, being poorly soluble in the ionomer, cannot penetrate the ionomeric layer, and thereby is restricted from both entering micropores within primary carbon particles and mesopores formed in the interior of agglomerates of primary particles. As the ionomer content is increased, it covers more and more of the agglomerate surface resulting in the continuous loss of the detectable micro- and mesopores. At ultra-high loadings, the ionomer completely fills meso- and macroporous voids resulting in nearly complete loss of detectable porosity, as illustrated in Figure 2.16.

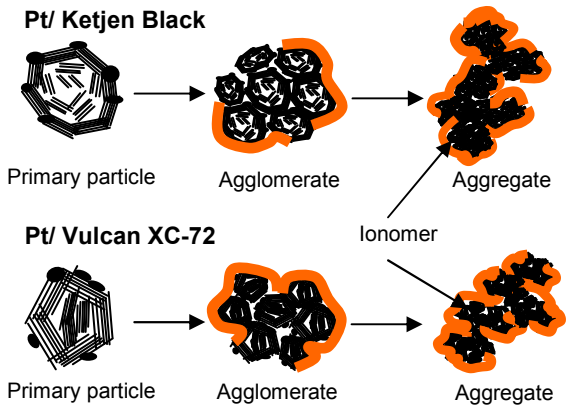

Figure 2.16: Schematic representation of Pt on the primary carbon particles of Ketjen Black and Vulcan XC-72 and the proposed distribution of ionomer on the surface of agglomerates. Micropores are blocked, and meso-macropores exist within aggregates of agglomerates (reproduced from ACS Appl. Mat. Interfaces 2, 375, 2010, by Soboleva with permission)

2.3.3 Pore network effects

In a porous medium with a broad pore size distribution, large pores can be trapped in between the network of smaller pores giving rise to a so called *pore network effect*. It was described by Everett that desorption of a condensed fluid from a pore is influenced by the state of the fluid in the neighbouring pores.[120] If a pore does not have direct access to the outer surface of the material, the desorption partial pressure of this pore depends on the desorption partial pressure of the pores surrounding it. Smaller pores have a lower desorption partial pressure (determined by the Kelvin relation), hence, if a large pore is trapped in the network of smaller pores, it cannot desorb until the desorption partial pressure of the smaller pore is reached. This effect manifests itself in the presence of a hysteresis between adsorption and desorption branches of an isotherm, which extends to low partial pressures (0.4 P/P_0 in case of N_2), and in the asymmetry of pore size distribution curves calculated from the either of the isotherm branches.[120] In Figure 2.12, it is clearly seen that Ketjen Black-based CLs have a more pronounced hysteresis as opposed to the Vulcan-based CLs, thus indicating the pore size trapping effect. This effect is also indicated by asymmetrical adsorption and desorption PSD curves of the CLs as shown in Figure 2.17. PSD curves calculated from the adsorption and desorption branches of the isotherm are almost identical in the case of the Vulcan-based CL with only a slight shift of the desorption curve to smaller pore radii. In the case of the Ketjen Black-based CL, a distinct difference between the curves is observed with a shift of the desorption curve to the left as well as the appearance of a new peak

in the pore radii < 4 nm. Similar PSD has been observed with carbon, Pt/carbon powders and CLs up to ionomer loading of 30 wt% (not shown here).

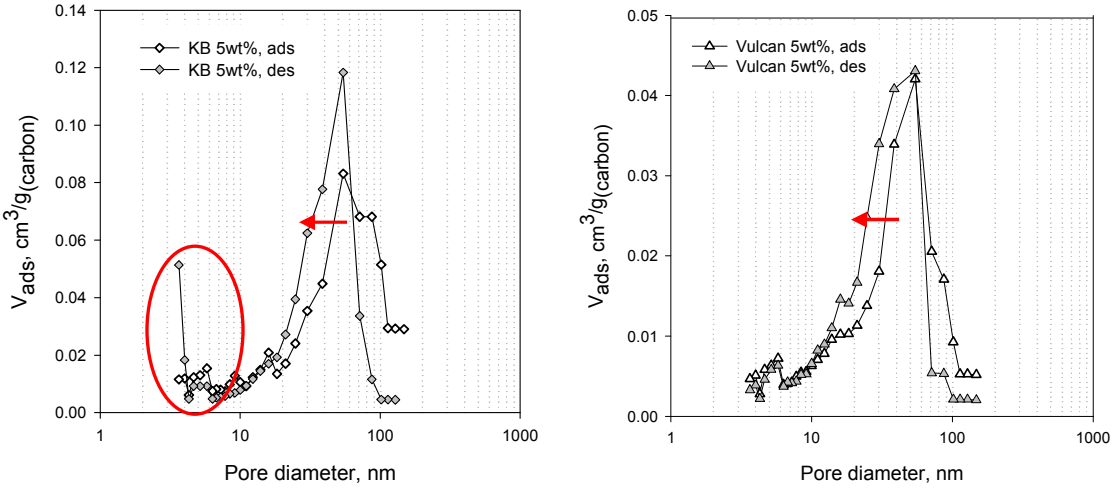

Figure 2.17: Pore size distribution curves of a) Ketjen Black and b) Vulcan 5 wt% ionomer CLs showing the pore network trapping effects.

An extensive pore trapping effect in the Ketjen Black CLs suggests the capability of these CLs to retain water, whereas the absence of the pore network in the Vulcan CLs is indicative of an enhanced water removal property. Water sorption and retention properties of the CLs are addressed in sections below.

2.4 Conclusions

N_2 adsorption, scanning and transmission microscopy were employed to study the microstructure of CLs in PEM fuel cells and to explain the CL microstructure based on structural characteristics of carbon blacks, Pt/carbon supported catalysts, and the formation of the CLs. Carbon black particles, consisting of turbostratic graphitic structures, coalesce to form agglomerates and

aggregates in the powder form. The character of carbon particles' aggregation in powder form is preserved in CLs, as evidenced by similar shapes of isotherms, hystereses and PSD curves. Two commonly used carbon supports, Ketjen Black and Vulcan XC-72, showed significant differences in total available surface area, pore volume, and the fraction of micropores. Ketjen Black possessed significantly higher surface area, due to its higher proportion of micropores, < 2 nm, and consequently much larger pore volume, compared to Vulcan XC-72.

The detectable micropore volume within Ketjen Black is significantly reduced upon deposition of Pt particles. Edge sites of microcrystalline carbon domains are known to be highly reactive due to unsaturated electron density, compared to basal plane carbon.[32,43,156] Higher surface area microporous carbons, such as Ketjen Black, are reported to possess a larger number of edge sites, i.e., they are less graphitized, and thus more microporous. Hence, Pt deposition may be initiated on the edge sites at the necks of micropores since deposition inside pores is unlikely as the Pt particle sizes are 2 – 4 nm. This phenomenon was not observed in case of Vulcan XC-72 because of its significantly lower fraction of micropores. By extrapolation, it is predicted that microstructural characteristics of lower surface area carbon supports, i.e., graphitized carbon, would not be significantly influenced by deposition of catalyst particles, because of their low micropore volume; whereas the reverse is true for higher surface area carbons.

Catalyst layers prepared with various ionomer contents retained the key features of the sorption isotherms of the native carbon powder. Ketjen Black-based CLs exhibited hysteresis over a wide range of partial pressures, from unity

to 0.4 P/P_0, indicating a complex pore network within the CL. In contrast, Vulcan XC-72-based CLs showed hysteresis only between partial pressures of unity to ~ 0.8 P/P_0, which is attributed to condensation-evaporation hysteresis rather than to a pore-network induced hysteresis.[120]

Catalyst layers based on Ketjen Black were generally found to possess higher detectable pore volumes than those based on Vulcan XC-72 at identical ionomer loadings. It is speculated that ionomer distributes on the surface of agglomerates covering the intra-agglomerate pores (< 20 nm); and this occurs with quite low ionomer loadings, e.g., as low as 5 wt% ionomer. These findings are in agreement with agglomerate structure proposed by Eikerling et al, in which pores inside agglomerates (primary pores) are assumed to be filled with water, whereas ionomer is located only in the pores between agglomerates (secondary pores).[82] For the purpose of fuel cell CLs, it is essential that ionomer contents are maintained as low as possible to sustain the appropriate void fraction for gaseous mass transport to occur, while still be sufficient for creating ionomer network for proton conduction. Indeed, significant blocking of pore space by ionomer is observed with higher ionomer loadings, and to a considerably larger degree in the case of Vulcan XC-72-based CLs compared to Ketjen Black-based CLs. This leads to an assumption that the widely accepted optimum value of 30 wt% ionomer content in the CL cannot be truly optimal for both of these carbons, since gas and water transport is expected to be hindered to a greater degree in Vulcan-based CLs due to lower pore volume. *Thus, it is suggested that optimum ionomer loading should be adjusted for each catalyst support depending on its*

surface area and pore volume, in particular, the fraction of meso- and macropores, since it has been indicated that only the surface area of pores > 20 nm is available for ionomer distribution. Moreover, the lower the fraction of surface area available for ionomer distribution, the thicker the ionomeric layer is created. Thickness of the ionomeric layer has a direct impact on available pore volume and hence gas and water transport in the CL, as illustrated in Figure 2.18. In the schematic, the mesoporous volume of Vulcan XC-72 aggregate, which has lower pore volume and surface area in respect to Ketjen Black-based aggregate, is shown to be reduced to a greater extent at the identical ionomer loading. A larger fraction of the surface area is covered in the 5 wt% ionomer case, a thicker ionomer layer is formed in the 30 wt% ionomer case, and a larger fraction of mesopores is completely filled with the ionomer in the 50 wt% ionomer case.

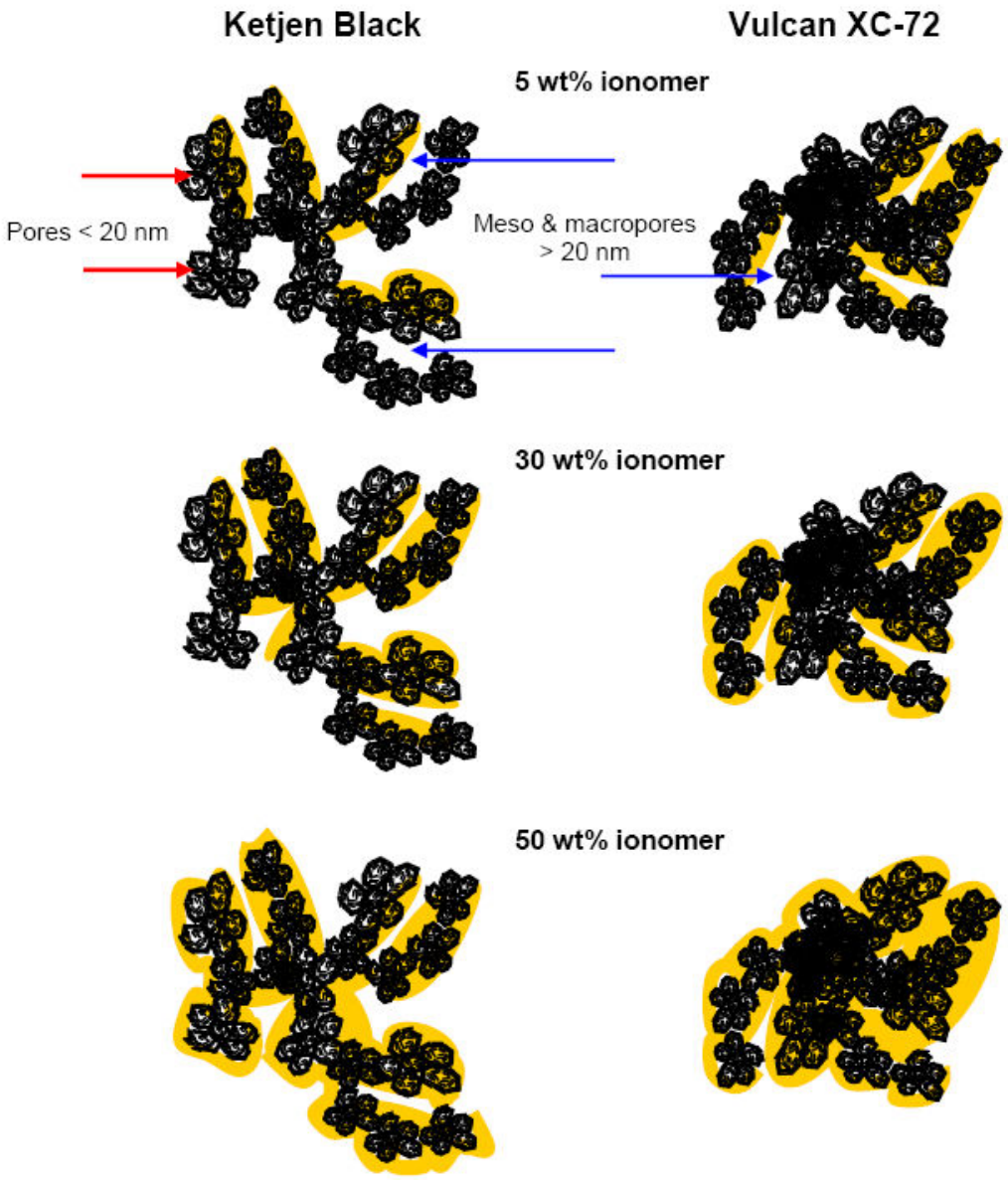

Figure 2.18: A schematic illustrating ionomer distributing in mesopores and its effect on pore volume in Ketjen Black and Vulcan XC-72-based CLs with 5, 30, and 50 wt% ionomer.

The significance of incorporating high microporosity, i.e., high surface area supports, is under debate since it was found that a significant fraction of Pt particles are deposited at the necks of the micropores, thus apparently nullifying

the effectiveness of this microporous space. Based on this finding it is speculated that micropores (< 2 nm) merely serve as active sites for Pt deposition without contributing to enhanced fuel cell performance.

The presence of an extensive porous network within Ketjen Black-based CLs is indicated by adsorption hysteresis and the asymmetrical pore size distribution curves. Pore network effects are known to arise in porous materials with broad pore size distribution where larger pores are trapped between smaller pores. A higher fractions of micro- to mesopores (as evidenced by a broader PSD) indicates a condition of pore-trapping in Ketjen Black-based CLs, which is absent in Vulcan-based CLs. This, in turn, has a direct implication on water retention properties of these CLs. It is suggested that Ketjen black-based CLs possess a better water retaining capability and hence are suspected to perform better at low relative humidities than the Vulcan-based CLs. On the other hand, due to these pore-trapping effects, Ketjen Black-based CLs are expected to suffer greater gas transport limitations if operated at high relative humidities. Based on these considerations, it is suggested that for anode CLs, catalyst supports with broader pore size distribution and more pronounced pore-trapping effects are advantageous, whereas for cathode CLs, materials with a rather narrow pore size distribution, that would facilitate water removal from the layer, are desirable. These hypotheses are examined in Chapter 4.

3: WATER VAPOUR SORPTION IN CLS

3.1 Introduction

One of the major goals of current fuel cell research is the reduction of Pt content in the electrodes. The improvement of Pt utilization can be achieved through advances in composition and structure of catalyst layers (CLs). In Chapter 2, the effect of carbon microstructure, Pt, and ionomer loading on the resultant microstructure of conventional CLs was discussed with the goal of gaining an understanding of which CL microstructural characteristics favour enhanced water transport properties in a CL and, consequently, overall fuel cell performance.

It has been widely recognized that ionomer content has a great impact on gas transport properties in a CL - the higher the ionomer loading, the lower the available pore space for gas transport.[92,157] A value of ~ 30 wt% ionomer has been accepted as an optimum trade-off value between sufficient pore volume for gas transport and the percolated ionomer network for proton conduction.[92-94] However, in the previous chapter, it was shown that ionomer distribution greatly depends on the surface area and pore size distribution (PSD) of the employed carbon support, in particular, the surface area and pore volume of mesopores, > 20 nm diameter. Only the surface area of pores that are larger than ~ 20 nm is available for ionomer distribution; the ionomer does not seem to penetrate into the smaller pores. Hence Pt particles deposited in the pores < 20 nm are not in

direct contact with ionomer and thus their participation in the fuel cell reaction is under debate. In the model developed by Eikerling et al, ionomer is assumed to be distributed on the surface of agglomerates, and the intra-agglomerate space is filled with water.[82] Water is believed to provide pathways for proton conduction to and from Pt particles that are not in direct contact with ionomer. However, very little is known about where and how water is sorbed, distributed, retained and desorbed from the CL. The majority of published work is related to water management in proton exchange membranes (PEM),[158] gas diffusion layers (GDL),[159,160] and flow fields.[161,162] In contrast, very scarce information is available on the role of catalyst layers in fuel cell water management apart from the modelling work that suggests that cathode catalyst layer is a key component in regulating the balance between water fluxes toward membrane and cathode outlet, and for the vaporization of liquid water created in the CL.[82]

Water management in PEM fuel cells has been recognized to greatly affect its overall performance. At present, a straightforward solution to the water management issue has not been found due the complexity of water fluxes inside the fuel cell. Water is supplied to a fuel cell with reactant gas streams in order to achieve sufficient humidification of the PEM for adequate proton conduction. On the cathode, water is produced in the oxygen reduction reaction. It is known that water is also transported from the anode to the cathode by protons travelling through the membrane, electroosmotic drag (EOD). This process is somewhat counter-balanced by a backflux of water toward the anode. However, if the backflux is insufficient to compensate the EOD, the resulting net water flux

toward the cathode adds on to the liquid water produced by ORR. These processes lead to drying out of the anode and flooding of the cathode and are exacerbated at high current densities. Drying out of the anode causes a decrease of ionomer proton conductivity within the anode catalyst layer and in the anode side of the membrane. Flooding of the cathode leads to the blockage of the pathways for oxygen transport and thus a reduction in the rate of ORR.

Early on it was recognized that the cathode catalyst layer performance can be enhanced by increasing its hydrophobicity.[87] Addition of PTFE to the cathode CL was believed to improve its water management properties by creating hydrophobic pores, however a number of drawbacks has been found. Permeability of oxygen through PTFE is significantly lower than through hydrated Nafion ionomer or water.[19] Therefore, access of oxygen access to the reaction sites that are covered with PTFE is hindered. In addition, the inclusion of PTFE was found to be detrimental for the formation of a proton conducting network of ionomer within the CL because it disrupts the continuity of the proton conducting network and decreases the hydration of Nafion ionomer, resulting in very poor proton conduction.[16,163] Moreover, CLs containing PTFE are usually significantly thicker and suffer reduced electron conduction due to a higher fraction of non-conducting phase. Despite these negative effects, improved performance of a CL with a controlled distribution of PTFE in a CL matrix has been recently reported by Friedmann et al.[164] A novel alternative to PTFE – dimethyl silicone oil – has been recently evaluated as a hydrophobic agent in the CL by Li et al.[165]

It seems intuitive to correlate water management behaviour of a material to its inherent hydrophobic/hydrophilic properties. However, in the case of a complex, multi-component, composite structures such as CLs, it is challenging to determine the overall hydrophobicity of the system. An attempt to evaluate overall surface hydrophilicity/-phobicity of a CL has been made by Yu et al through contact angle measurements.[166] Contact angle measurements are, however, dependent on composition and roughness; both of these properties are very inhomogenously distributed in the CL. Moreover, the surface of the carbon and the ionomer is composed of both hydrophobic and hydrophilic sites, the concentration and distribution of which greatly influence the overall hydrophilicity, as discussed below. Furthermore, based on the results presented in Chapter 2 it is predicted that, besides the surface properties, water sorption and retention in the CL also depend on structural characteristics of the carbon such as surface area, porosity, and pore size distribution.[90]

Hydrophobic/ hydrophilic properties of porous carbons are governed by the surface microstructure of carbon particles. The greater reactivity of carbon atoms with unsaturated valences on edge sites leads to formation of oxygen-containing surface functionalities that in turn increase the hydrophilicity of the carbon. Thus, the overall hydrophobicity of a porous carbon is expected to depend on the ratio of the edge sites to the basal sites, e.g., graphitized carbons posses much larger fraction of basal planes and consequently are more hydrophobic. On the other hand, high surface area carbons (200–1500 m^2/g) are known to possess very

high microporosity (< 2 nm), which is directly related to an increased number of edge sites, and are thus expected to be more hydrophilic.

Nafion ionomer employed in conventional CLs is comprised of a hydrophobic backbone and hydrophilic side chains. Its distribution in a CL depends on its interaction with the carbon surface (oxygen-containing groups, basal planes) and with Pt. Adsorption of Nafion ionomer on supporting carbons has been studied by Ma et al. using ^{14}F NMR spectroscopy.[167] The authors reported a stronger interaction between Nafion and carbon than between Nafion and Pt as well as a 4-times larger relative coverage of Vulcan XC-72 carbon surface by ionomer compared to that of Ketjen Black surface.

In this chapter, we correlate described microstructural properties of Ketjen Black and Vulcan XC-72 carbons, platinized composites and CLs with their water vapour sorption and water retention properties.

3.2 Experimental

3.2.1 Materials

Carbon, Pt/carbon and CCMs with 5, 30, and 50 wt% ionomer in catalyst layer samples described in Chapter 2.2.1. were used to perform DVS measurements. Samples of carbon powder and Pt/carbon powder of ~ 5 mg were used for DVS measurements. In the case of CCMs, two punches of 0.5 cm diameter, die-cut from 25 cm^2 CCMs, were used in each experiment.

Analytical Pt loadings in the samples were determined from ICP-MS (Inductively coupled plasma mass spectrometry) by Exova Surrey. CCM samples

of 0.5 cm diameter were dried and grinded, and then dissolved in HNO_3. Aliquots of 5 mL were analysed. Pt contents were reported by Exova in mg/L, and corresponding Pt loading in each sample was re-calculated to mg_{Pt}/cm^2. Carbon and ionomer loadings were calculated based on the known Pt/C ratios in the catalyst powders (0.46/0.54) and ionomer to carbon ratios (I/C ratio) of the CLs.

3.2.2 Methods

A DVS Advantage chamber from Surface Measurement Systems (SMS) was used to perform water vapour sorption experiments. Water uptake of samples was evaluated at 25 ºC in the range of relative humidity from 0 – 97% RH with 10% RH steps from 0 to 90% RH, then to 95 and finally 97% RH. Desorption isotherms were recorded following a backward sequence of relative humidities. CCM samples were suspended on a wire so that the film freestanding conditions were maintained. Samples were equilibrated at each RH stage using a *d*m/*d*t parameter of 0.0002 %/min (change in mass (*d*m) over time (*d*t)). Nitrogen, 99.95%, was used as a carrier gas and de-ionized water was used to humidify the carrier gas.

A Nafion 211 isotherm was used as a blank to separate contributions of the membrane and the CLs to the total amount of water vapour sorbed by a CCM. In Appendix A, sorption isotherms of a Nafion 211 membrane and a CCM are shown.

Water uptake in a CL was found by subtracting the water content in Nafion 211 membrane from the total water uptake by a sample of a CCM. Water uptake

of the CLs is expressed as the mass of water at each RH normalized to carbon content in the sample. The carbon content in Pt/C powders was calculated from the known ratio of Pt on carbon, as specified by the manufacturer.

3.3 Results and discussion

3.3.1 Water vapour sorption in carbon and Pt/C catalyst powders

Water vapour sorption capacity of carbon powders is found to be extremely low, e.g., ~ 0.03 $cm^3/g_{(carbon)}$ at 97% RH for Ketjen Black and Vulcan XC-72 carbons as shown in Figure 3.1. Vapour sorption isotherms of Pt/ Ketjen Black and Pt/ Vulcan XC-72 normalized to carbon mass are also shown in Figure 1. A low sorption capacity of carbon powders is indicative of their hydrophobic nature; contact angles for Ketjen Black and Vulcan XC-72 carbons were reported to be 84º and 79º, respectively.[32] However, when Pt is deposited on carbon, the Pt/carbon powder becomes considerably more hydrophilic due to the wetting properties of Pt (the contact angle of water on Pt is 10º).[5]

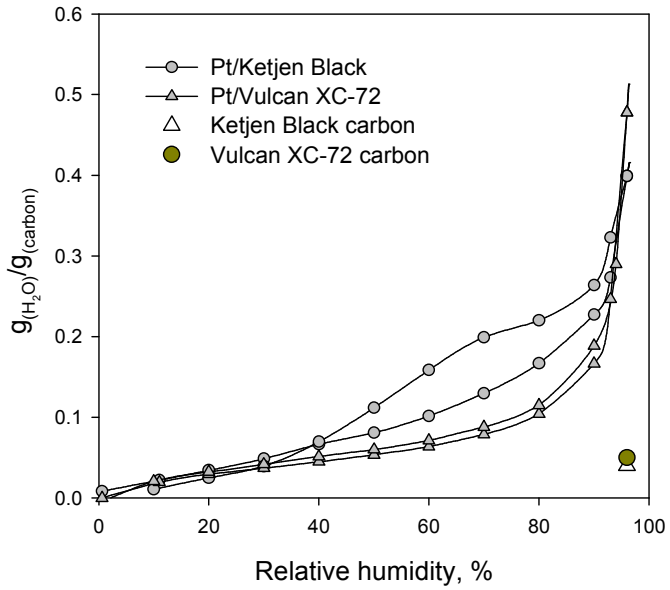

Figure 3.1: Water vapour sorption isotherms of Pt/Ketjen Black (triangles) and Pt/Vulcan XC-72 (circles) catalyst powders. Reference data points for sorption capacity of Ketjen Black and Vulcan XC-72 carbon powders are shown at 97% RH.

Both Pt/carbon isotherms are Type 3 in nature[118,119] with little sorption at low RH and exponentially increasing sorption in the higher RH range. This type of adsorption isotherm is characteristic of strong intermolecular gas interactions and a weak gas-adsorbent interaction. The former is typical of water vapour due to propensity of water molecules to form hydrogen bonds. The latter is due to weak interaction between polar water molecules and nonpolar carbon black.[168] Adsorption below 30% RH is comparatively low, as it is typical for Type 3 adsorption isotherm, due to adsorption of adsorbate molecules on the polar sites as opposed to formation of a monolayer as is the case for a nonpolar adsorbent such as nitrogen.[120,169] Hence, it is assumed that in the low RH condition, water

molecules adsorb first on the hydrophilic sites, such as Pt particles, oxygen containing functional groups on carbon, and edge sites of carbon crystallites.[170,171] In the intermediate range of RH, water molecules build up multilayers around hydrophilic sites due to hydrogen bonding and, when these localized clusters of water are large enough, they coalesce; concurrently capillary condensation takes place.[120,172] Pt/Ketjen Black sorbs noticeably more water than Pt/Vulcan XC-72 in the range of RH between 30 – 90%, presumably due to a larger fraction of mesopores in which capillary condensation occurs. It has been previously reported by Pierce et al that the presence of mesopores results in steeper water adsorption isotherms in the intermediate range of RH.[172] The point of inflection is a function of the size of the mesopores; the smaller the pore size, the lower the relative pressure at which the rise begins. The Pt/Ketjen Black adsorption curve diverges from the Pt/Vulcan XC-72 adsorption curve at 30% RH, which is attributed to the higher mesoporous volume of Pt/Ketjen Black: 0.68 $cm^3/g_{(carbon)}$ for Pt/Ketjen Black versus 0.34 $cm^3/g_{(carbon)}$. The mesoporous volume was found as a difference between total pore volume and pore volume < 2nm (refer to Table 2.1). The total volume of adsorbed water is close to the volume of adsorbed nitrogen in the case of Pt/Vulcan black: 0.48 ± 0.05 $cm^3/g_{(carbon)}$ of water and 0.39 ± 0.003 $cm^3/g_{(carbon)}$ of N_2. In the case of Pt/Ketjen Black, however, the volume of water is significantly lower than that of N_2: 0.4 ± 0.005 $cm^3/g_{(carbon)}$ and 0.86 ± 0.06 $cm^3/g_{(carbon)}$, respectively. A similar trend has been observed earlier by a number of researchers, as summarized by Gregg et al.[120] The liquid volume of water sorbed by a carbon sample at saturation was usually

less than that of the other nonpolar adsorbate, which has been attributed to lower density of water in the pores. Another reason might be due to inaccessibility of micropores in Ketjen Black to water molecules.

A larger hysteresis in the intermediate range of RH in the case of Pt/Ketjen Black is attributed to the presence of the extensive pore network, i.e., trapping of larger pores in the network of smaller pores.[120] As has been discussed in Chapter 2, Pt/Ketjen Black possesses a wider PSD than Pt/Vulcan XC-72[90] which is believed to enhance pore trapping effects.

3.3.2 Effect of carbon support and ionomer content in CLs

As has been shown above, the extent of water vapour sorption differs for Pt/Ketjen Black and Pt/Vulcan XC-72. The effect of the carbon support on water vapour sorption of CLs is demonstrated below. Sorption isotherms of Pt/Ketjen Black- and Pt/Vulcan XC-72 – based CLs with a range of ionomer loadings normalized to mass of carbon are shown in Figure 3.2. Corresponding Pt/carbon sorption isotherms are shown for reference. As it is seen from the figure, microstructural characteristic features of the isotherms of the native carbon supports, such as the shape of the adsorption branch of the isotherm and the hysteresis, are preserved upon addition of the ionomer. However, incorporation of ionomer results in a higher total water uptake in a CL, which rises with increasing ionomer loading.

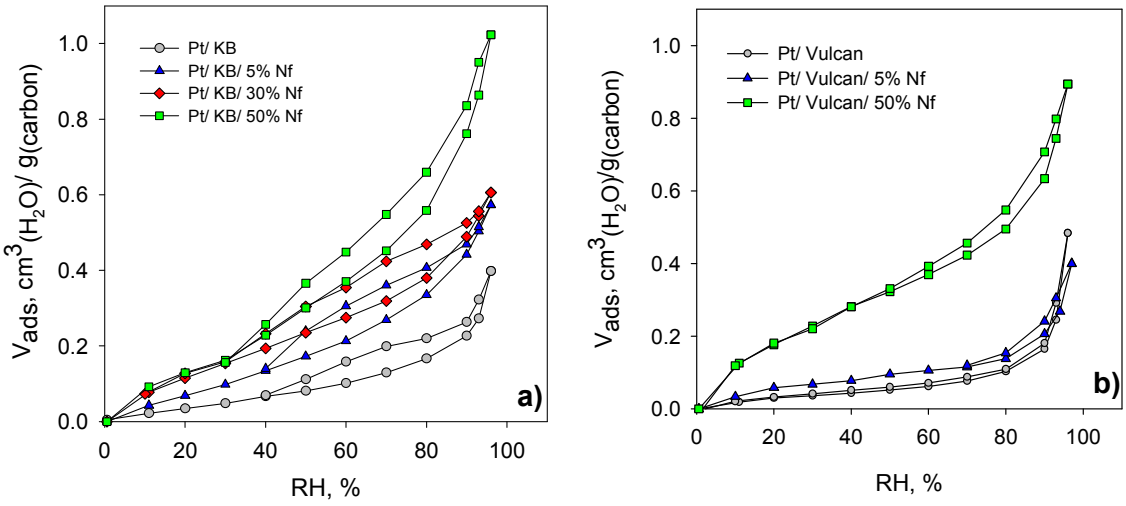

Figure 3.2: Water vapour sorption isotherms of a) Pt/Ketjen CLs with 5, 30, and 50% ionomer and b) Pt/Vulcan XC-72 with 5 and 50% ionomer normalized to carbon content.

Upon addition of the ionomer, an enhanced water sorption is seen in the RH range as low as 10 – 30%. This could be attributed to the increase in the number of hydrophilic sites in the CL - sulfonic groups of Nafion ionomer, $-SO_3^-$, which serve as initial adsorption sites for water molecules, i.e., formation of water clusters at low RH. This effect is more pronounced with increasing ionomer loading as the number of $-SO_3^-$ groups increases.

The slightly higher total water uptakes for Pt/Ketjen Black-based CLs for identical ionomer contents are in agreement with the higher pore volume of Ketjen Black carbon as determined by N_2-adsorption. Moreover, Ketjen Black-based CLs are less dense than Vulcan XC-72 CLs at identical carbon, Pt and ionomer loadings, and have a larger proportion of void space where water can be

incorporated. CL composition and water sorption data are summarized in Table 3.1.

Table 3.1: CL specifications and water sorption data

Carbon type	Ionomer loading, wt%	Pt loading, mg/cm^2	Carbon loading, mg/cm^2	Ionomer loading, mg/cm^2	CL thickness, μm	V_{ads}, 20% RH, $cm^3_{H2O}/g_{(carbon)}$	V_{ads}, 97% RH, $cm^3_{H2O}/g_{(carbon)}$	Vpore, $cm^3/g_{(carbon)}$
KB	5	0.45	0.53	0.04	15.3 ± 2.5	0.07 ± 0.002	0.57 ± 0.03	0.86
	30	0.49	0.58	0.46	18.5 ± 4.0	0.11 ± 0.004	0.61 ± 0.03	0.86
	50	0.38	0.45	0.69	9.6 ± 0.8	0.13 ± 0.01	1.02 ± 0.20	0.86
Vulcan	5	0.4	0.48	0.05	10.0 ± 0.5	0.06 ± 0.05	0.4 ± 0.08	0.39
	50	0.32	0.38	0.67	9.0 ± 0.6	0.18 ± 0.03	0.9 ± 0.03	0.39

Pt loading is determined from ICP; one sample of each catalyst layer was analysed. Carbon and ionomer loadings are calculated using Pt/carbon and ionomer/carbon weight ratios. CL thickness is determined by SEM; V_{pore} determined from N_2 adsorption for Pt/carbon powders.

In order to compare the effect of carbon support and ionomer content on the overall water sorption, isotherms of Ketjen Black and Vulcan XC-72-based CLs with 5 and 50 wt% ionomer in the CL normalized to mass of carbon in CL are shown in Figure 3.3.

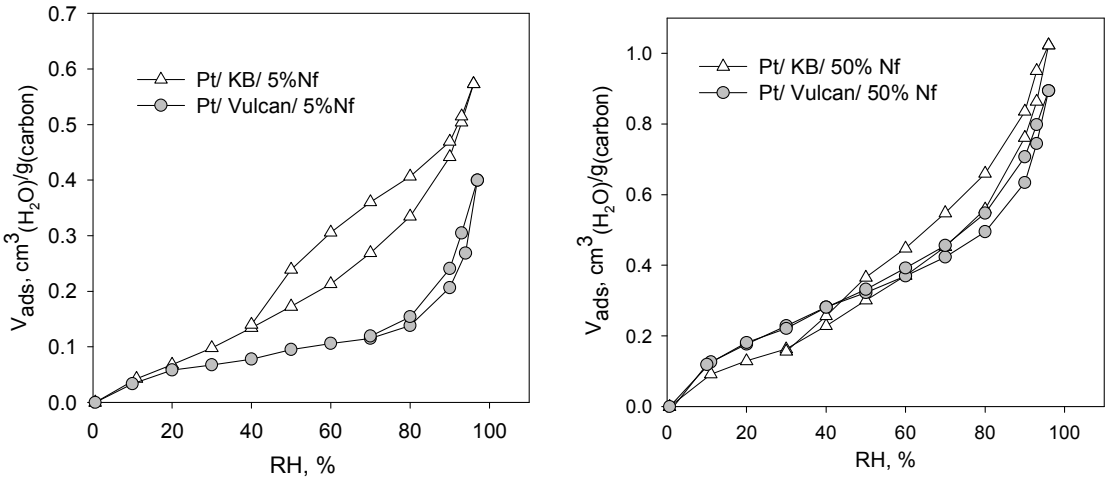

Figure 3.3: Water sorption isotherms normalized to mass of carbon: Pt/Ketjen (triangles) and Pt/Vulcan XC-72 (circles) CLs with 5 and 50% ionomer.

In the case of CLs containing 5% ionomer, Ketjen Black-based CLs sorb considerably more water than Vulcan CL in the range of RH > 20 %. The shape of the isotherms and hystereses maintains the features of the corresponding carbon supports – larger hysteresis and a higher slope of the isotherm rise in the intermediate RH range in the case of Ketjen Black (refer to Figure 3.1). The higher slope of the sorption isotherm is indicative of pronounced capillary condensation in the pores of carbon and the hysteresis is indicative of enhanced water retention capacity in the pore network. In the case of CLs containing 50% ionomer, water sorption is enhanced in both carbon types; the difference in the total amount of sorbed water decreases between carbons and microstructural characteristic features of Pt/carbon isotherms become less pronounced. This is attributed to a dominant effect of the ionomer in the water vapour sorption

process at such high ionomer contents. The effect of the carbon support microstructure on the extent of water sorption is screened at high ionomer loadings.

3.4 Conclusion

The microstructure of conventional catalyst layers has a significant impact on water sorption and water retention properties. The extent of water sorption depends on the pore size distribution of the carbon support and on the ionomer loading in the CL. The larger the fraction of mesopores (2 – 20 nm), the larger the amount of water sorption in the intermediate range of RH. This is attributed to capillary condensation of water in these pores. Moreover, in the case of Ketjen Black-based CLs, which possess a broad pore size distribution, pore trapping effects are more pronounced leading to higher water retention in the CL, as manifested by a broad hysteresis. Incorporation of ionomer into the CL enhances water sorption and the effects of the carbon microstructure on water sorption are less pronounced. In CLs with very low ionomer loading of 5 wt%, water sorption is governed by the carbon microstructure, whereas in the CLs with high ionomer loading of 50 wt%, water sorption by the ionomer dominates.

4: ELECTROCHEMICAL CHARACTERISATION OF CATALYST LAYERS

4.1 Introduction

As discussed in the previous sections, the composition of the CL and the structure of its constituent components have a strong influence on the resultant microstructure and water sorption and retention, which in turn influence fuel cell performance.

The kinetics of the fuel cell reaction is a function of the concentration of O_2 and H_2 (i.e., proton) at the Pt surface, and the electrochemically active surface area of Pt – the area available to the redox reactions as described by the Butler-Volmer equation (1.8) and equation 1.7. The surface concentrations of gases at the Pt interface are a function of the porous structure of the catalyst layer. The rate of gas diffusion in a pore depends on the size of the pore and in the pore size range of the CL (< 10^{-8} m) is described by Knudsen diffusion.[173]

In the fuel cell catalyst layer during operation, a pore is often either partially or fully filled with water, which impedes gas diffusion to the reaction sites. As discussed in the previous section, the degree of pore filling depends on the pore size and the operating conditions. Operating at high RH results in a higher water content in the CL and the pores in the range 2 – 20 nm are assumed to be filled with water by capillary condensation. In these pores, gas transport to the reaction sites occurs through the liquid water phase at a slower rate: ~ 10^{-5} cm^2/s in

water[19] vs. ~ 10^{-3} cm^2/s in a pore via Knudsen diffusion.[173] In the larger pores that are only partially filled with water, gas diffusion occurs either in the porous space or through the water film. Ionomer is the third medium through which gases are transported at the Pt particle interface. Gas permeation through the ionomer layer is slower than that in gas phase and water as has been shown by Sakai et al.[19] Permeability of O_2 through the ionomer film under different water contents and temperatures has been studies by Parthasaraty et al.,[174] and Beattie et al.[115] Overall, the higher the ionomer content in the CL, the slower are the rates of gas transport due to the blocking of the pore space by ionomer.

A percolated ionomer network must be present in the CLs for proton conduction to and from the reaction sites. Thus, the proton concentration at the Pt particles interface is a function of the ionomer content and the connectivity of the ionomer network. It is well known that the proton conductivity of the polymer electrolyte membrane strongly depends on the water content – the higher the hydration of the membrane, the higher the proton conductivity.[175] The same is valid for Nafion ionomer in the CL; however, little is known about the water sorption properties of ionomer in the CL. They are expected to differ from those of bulk Nafion membrane properties due to the nature and distribution of the polymer chains inside the CLs and their interaction with other constituents of the CL – Pt, carbon, and hydrophilic functional groups on the carbon surface.

The electrochemically active surface area (ESA) is an important parameter determining the exchange current density of the fuel cell reaction. ESA is the interfacial area between Pt particle and a proton-conducting medium, i.e.,

ionomer or water, and thus it is also a function of ionomer content in the CL. Only Pt particles that are in contact with the proton conducting phase participate in the fuel cell reaction. However, Eikerling et al.[82] noted that water acts as the primary proton-conducting phase and thus the ESA is also a function of water content in the CL.

The nature of fuel cell operation poses different requirements on the water handling capabilities of the cathode and the anode. Due to the production of liquid water at the cathode and the net flux in a FC being towards it, the cathode needs to posses enhanced water removal properties in order to mitigate flooding. The anode, on the other hand, is prone to losing proton conductivity due to dihydration, hence it has to possess a high water retention capacity.

In this chapter, the electrochemical properties and fuel cell performance of CLs are correlated to their microstructure, composition, and water sorption and retention properties. The potential for the application of CLs with different water sorption and retention capabilities to the anode and the cathode of an MEA is examined.

4.2 Experimental

4.2.1 Materials

25 cm^2 MEAs prepared as described in Section 2.2 were used for electrochemical characterization.

4.2.2 Cyclic voltammetry (CV)

Cyclic voltammetry was used to calculate electrochemically active surface area (ESA) and double layer capacitance (C_{DL}) of the CLs in the 20 – 100% RH range. Prior to CV measurement, the cell was conditioned using evaporation-condensation cycles: the cell was heated up to 80 °C at 100% RH H_2 was fed to the anode while N_2 to the cathode for 1 h, then cooled to ~ 30 °C for another hour, while gases were kept at 80 °C to allow sufficient water condensation in the CL. The cell was then heated to 80 °C and the CVs were recorded. The cycle was repeated until no change in the CV shape was observed (3 – 5 cycles).

H_2 adsorption and desorption currents on Pt were measured in the H_2/N_2 atmosphere in order to avoid the contribution from faradaic reactions at 1atm (abs). A Solatron 1287 potentiostat was used. The potential was scanned between 0.04 and 1.1 V vs. SHE at a scan rate of 50 mV/s. Catalyst layers were tested in the range of 20 – 100% RH. Relative humidity was stepped from 100% RH in the downward scan with 10% RH steps allowing enough time for the cell to equilibrate at each condition. Gas flow rates of 0.2 L/min on the anode and 0 L/min, i.e., no gas flow, on the cathode were used. A cycle of five CVs was repeated three times, the 5^{th} CV in each cycle was used for data analysis.

ESA was calculated from charges corresponding to Pt-H adsorption in the range from 0.08 to 0.45 V using Corrware® software accounting for double layer charging and hydrogen crossover currents.[3] Reported ESA values are the average of three voltammograms.

Double layer capacitance (C_{DL}) was calculated from the double layer charging current in the range 0.4 – 0.6 V after subtraction of the hydrogen crossover current. The hydrogen crossover current was measured by chronoamperometry in the 0.2 – 0.5 V range with a step of 0.1 V. Each potential value was held for 3 min in order to minimize the contribution from the charging current. The value of current at the end of each potential step was ploted versus corresponding potential. The hydrogen crossover current was estimated from the intercept of the plot with the ordinate.

4.2.3 Electrochemical impedance spectroscopy (EIS)

The proton conductivity of CLs was evaluated using EIS under H_2/N_2 atmosphere (anode/cathode) in order to eliminate impedance of the faradaic processes. EIS was employed at 0.45 V DC signal imposing a 10 mV amplitude sinusoidal (AC) signal over the frequency range 15 kHz to 0.01 Hz using a Solatron 1287 potentiostat and a 1260 frequency analyzer. Impedance spectra were recorded under 20 – 100% RH in 10% RH steps. A Nyquist plot in the H_2/N_2 atmosphere usually has two characteristic slopes (refer to Figure 1.11): the first slope at ~ 45º angle in the high frequency region is due to proton resistance in the CL, the second slope at an angle between 55º ~ 90º (the lower the angle, the higher the magnitude of H_2 crossover) at lower frequencies is dominated by the capacitance of the CL. By extrapolating the second slope to the Z'-axis, the proton resistance of the cathode CL can be found as a difference between the extrapolated linear intercept and the intercept of the Nyquist plot with the Z'-axis (membrane resistance) and divided by 3: [3]

$$R_p = \frac{Z'_{LF} - Z'_{HF}}{3} \quad \textbf{4.1}$$

where, R_p is proton resistance, Z'_{LF} is the low frequency intercept, and Z'_{HF} is the high frequency intercept of the Nyquist plot.

In the low RH condition and in the CLs with very low ionomer loading, the transition between slopes was poorly defined. Thus, the proton resistance was estimated using an alternative method. The linear slope of the EIS spectrum in the range 10^4 – 10^3 Hz, representing contributions from the proton resistance and double layer charging capacitance of the CL, is expressed as follows[176]:

$$Z = \sqrt{\frac{R_p}{C_{DL}}} \cdot \omega^{1/2} \quad \textbf{4.2}$$

where Z is magnitude of the real part of impedance, R_p is the proton resistance, C_{DL} is double layer capacitance, and ω is the angular frequency (equal to 2πf, where f is ordinay frequency measured in hertz). By plotting Z vs. $\omega^{1/2}$, the slope $\sqrt{\frac{R_p}{C_{DL}}}$ can be found. Taking the double layer capacitance value determined from CV at each given RH at ~ 0.45 V, the resistance to proton conduction in the CL can be estimated. Proton conductivity is then calculated from R_p and thickness of the catalyst layer determined by SEM.

EIS experiments performed under H_2/O_2 under increasing operational current densities were used to quantify the charge and mass transfer resistances in the

CLs, as well as the uncompensated resistance of the cell, R_U, (i.e., membrane, cell and cell hardware resistances), under 20 – 100% RH. H_2/O_2 EIS was recorded in the frequency range 20 kHz to 0.1 Hz and increasing current densities (0.04 A/cm^2 to ~ 1 A/cm^2). R_U was determined from the high frequency intercept of the Nyquist plot with the Z'-axis. The diameter of the semi-circle is the sum of resistances to the charge transfer and mass transport processes, R_{CT} + R_{MT}, and was used to deconvolute the effects of charge and mass transport resistances.[92]

4.2.4 Fuel cell polarization analysis

MEAs were assembled in a 25 cm^2 single cell with triple serpentine flow channels from Fuel Cell Technologies Inc. Polarization curves were recorded on a 850C test station from Scribner Associates Inc. Prior to obtaining IV polarization data, the cell was conditioned at 80 °C and 100% RH in the potential range between 0.9 V and 0.6 V in 0.05 V steps.

Polarization data were collected by scanning the cell voltage from open circuit voltage (OCV) to 0.2 V in 0.05 V steps (120 s at each potential point). The cell temperature was 80 °C at atmospheric pressure. IV curves were recorded under dry (20% RH) and fully humidified conditions (100% RH). Scans were repeated five times to ensure reproducibility within each MEA.

4.3 Results and discussion

4.3.1 Electrochemically active surface area (ESA) and double layer capacitance (C_{DL})

Cyclic voltammograms of Ketjen Black CLs with 5 and 50 wt% ionomer at 100% RH are shown in Figure 4.1. As it is seen from the figure, the shape of the CVs strongly depends on the ionomer content. The H_2 adsorption and desorption peaks (< 0.4 V) as well as PtO formation and reduction peaks (> 0.6 V), and double layer capacitance (0.4 – 0.5 V) are significantly reduced in the low ionomer content CL. This is due to a decrease in the interfacial area between Pt and the ionomer as the ionomer loading is decreased.

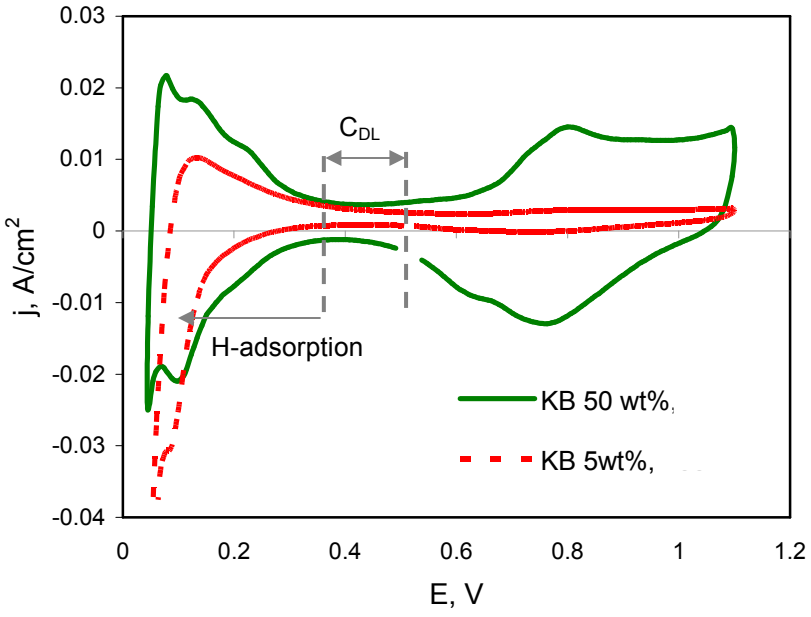

Figure 4.1: Cyclic voltammograms of Ketjen Black CLs with 5 and 50 wt% ionomer, 100% RH, 80 ºC, H_2/N_2, 0.4 mg_{Pt}/cm^2 loading.

The electrochemically active surface area (ESA) is attributed to the interfacial area of Pt and ionomer and water, and is a parameter required for estimating kinetics of the fuel cell reaction. The ESA of CLs was investigated as a function of ionomer content and the relative humidity. In the Figure 4.2, it is shown that the ESA strongly depends ionomer content as well as on relative humidity, i.e., water content in the CL.

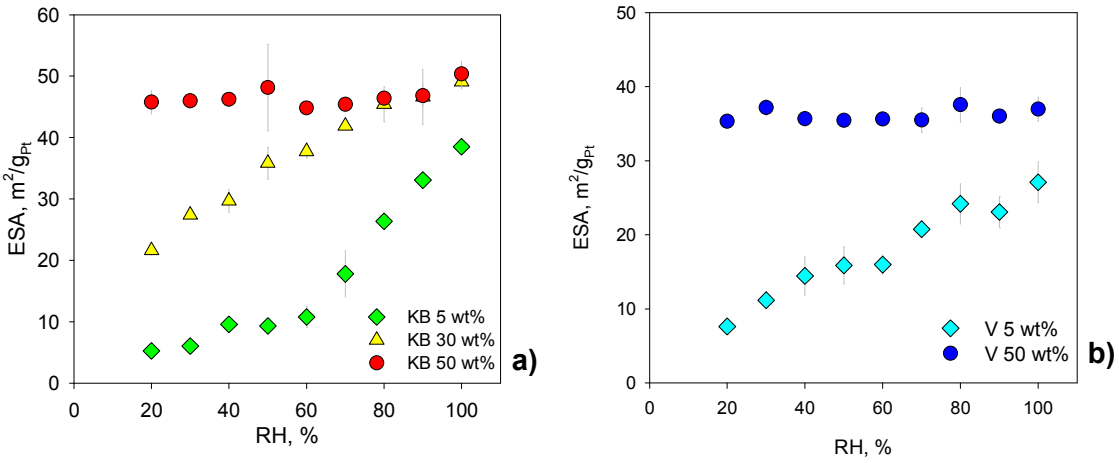

Figure 4.2: Electrochemically active area determined by cyclic voltammetry as a function of RH and ionomer content for a) Ketjen Black CLs with 5, 30, and 50 wt% ionomer, b) Vulcan-based CLs with 5 and 50 wt% ionomer.

Under dry conditions (20% RH), the ESA is shown to increase with ionomer loading in both CL types due to the increase in the interfacial area between Pt and the ionomer. Catalyst layers with 5 and 30 wt% ionomer also show a drastic rise in the ESA with increasing RH from 20 to 100% RH. This increase is attributed to the growing Pt-water interface as water content in the CL increases, which underlines the importance of water in electrochemical activity of the CL. An

nearly exponential rise in the case of 5 wt% Ketjen Black CL is attributed to the capillary condensation of water into the primary pores inside agglomerates (< 20 nm), which are abundant in Ketjen Black as has been shown in Chapter 2. Such a rapid increase in the ESA upon capillary condensation suggests that a large fraction of Pt particles is located in these pores and becomes electrochemically active only after the pores are filled with water. In contrast, a linear rise in the ESA in the case of the Vulcan 5 wt% ionomer CL suggests that Pt particles are located in the mesopores easily accessible to water. Interestingly, the ESA of 5 wt% ionomer CLs approaches the value of 50 wt% CLs in 100% RH, indicating that a relatively high Pt utilization can be achieved even with very low ionomer contents under fully humidified fuel cell operating conditions. By extrapolation, in the operating fuel cell liquid water is produced at the cathode in addition to the water supplied with the reactant gas stream, as opposed to the CV experimental condition where the only source of water is the humidified N_2 gas stream, higher ESA values might be reached. In contrast to the lower ionomer content CLs, ESAs of CLs with 50 wt% ionomer seem to be RH-independent. This might be due to the relatively large amount of water initially present in the 50 wt% ionomer CL under 20% RH (~ 0.1 $cm^3/g_{(carbon)}$) compared to the 5 wt% ionomer CL (~ 0.01 $cm^3/g_{(carbon)}$) or due to prevailing sorption of water in the ionomer layer instead of on Pt particles. However, if ESA values are plotted against actual water content in the CL determined from water vapour sorption experiments as described in Chapter 3, some insightful trends are found, as shown in Figure 4.3. Firstly, a distinct difference in the character of water vapour sorption is seen in

the 5 wt% ionomer CLs: in the case of Vulcan CLs, a steep increase in the ESA is observed with water contents < 0.2 $cm^3/g_{(carbon)}$, after which the ESA seems to plateau at ~ 27 m^2/g_{Pt} ESA. In the case of the Ketjen Black 5 wt% ionomer CL, a significantly slower rise in the ESA is seen with low water contents, < 0.2 $cm^3/g_{(carbon)}$, while considerably higher values, ~ 39 m^2/g_{Pt}, in comparison to the Vulcan 5 wt% ionomer CL are reached with water contents > 0.5 $cm^3/g_{(carbon)}$). The point of inflection at the water content of 0.22 $cm^3/g_{(carbon)}$, corresponding to ~ 60% RH, indicates the onset of the capillary condensation in the intra-agglomerate mesopores of the Ketjen Black CLs, which is absent in the case of the Vulcan-based CL, as also has been shown in terms of adsorption-desorption hysteresis in Chapter 3. This clearly indicates that a large fraction of Pt particles is located in the intra-agglomerate pores in the case of Ketjen Black, which become electrochemically active only after partial pressure of water corresponding to the capillary condensation in these pores, has been reached.

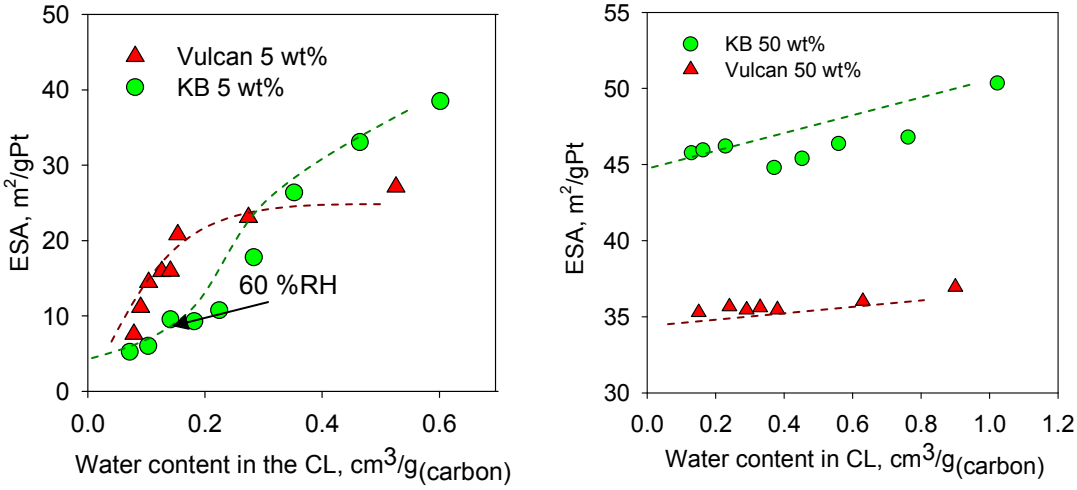

Figure 4.3: Electrochemically active surface area as a function of water content, determined by DVS, and ionomer content in Ketjen Black and Vulcan-based CLs.

The electrochemically active surface area of CLs with 50 wt% is shown to increase slightly with water content: from 46 to 50 m^2/g_{Pt} in the case of the Ketjen Black-based CL, and from 35 to 37 m^2/g_{Pt} in the case of the Vulcan-based CL under 20 and 100 %RH, respectively. The Vulcan 50 wt% ionomer CL seems to possess ~ 25% lower ESA values than the Ketjen Black 50 wt% ionomer CL with identical Pt loading and water contents.

From these findings, it is seen that even in the CLs with an extremely low ionomer loading of 5 wt%, adequate utilization of Pt can be achieved under high RH condition, which promote high water contents in the CL, which, in turn, underlines the importance of water in the electrochemical processes in the catalyst layer. Due to the structural nature of Ketjen Black, i.e., large fraction of pores < 20 nm, where Pt particles seem to be located, much Pt remains inactive

until water condenses in these pores in the high RH range. Pt utilization under low RH conditions can be estimated assuming the value of the ESA in 100% RH to be the total available ESA area of a CL. Then, only ~ 10% of available Pt is active in 20% RH in the case of Ketjen Black 5 wt% ionomer CL, in contrast to ~ 40% in the case of Vulcan 5 wt% ionomer CL. Thus, the location of Pt in the intra-agglomerate mesopores < 20 nm might be considered disadvantageous for the fuel cell operation under low RH condition.

In addition to promoting electrochemical activity of Pt, the ionomer serves as a proton conductor to and from reaction sites. In this case, continuous distribution of ionomer in the CL is crucial for creating a H^+-conducting network. The ionomer distribution is correlated to the double layer capacitance (C_{DL}) of the CL, which represents Pt-ionomer and carbon-ionomer interface. The extent of Pt and carbon coverage by ionomer is expressed by the ionomer coverage. In Figure 4.4, C_{DL} is shown as a function of the ionomer content and RH. C_{DL} is found to rise with the ionomer content because of the increase in Pt-ionomer and carbon-ionomer interfacial areas. As in the case of the ESA, C_{DL} is also found to increase with RH due to contributions of Pt-water and carbon-water interfaces. In 5 wt% CLs, an insignificant variation in C_{DL} is observed in the RH range < 60%, but it increases exponentially above this value. An exponential increase of C_{DL} under higher RH coincides with the onset of the capillary condensation of water in the primary pores within agglomerates (2 – 20 nm), as also observed in the plot of the ESA vs. RH. A similar behaviour was observed by Iden et al. in a Ketjen Black - ionomer pseudo-catalyst layer.[177] It is interesting to note that while

an increase in C_{DL} of 5 wt% ionomer CLs is seen only under high RH condition, the increase in the ESA is seen immediately with the rise of RH. This might be interpreted as preferential adsorption of water molecules firstly on Pt particles before adsorption on oxygen-containing surface groups on carbon or in the ionomer.

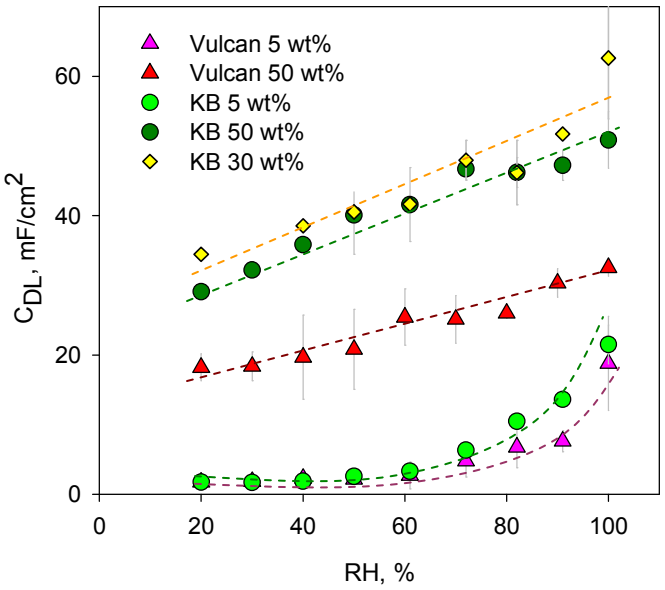

Figure 4.4: Double layer capacitance of Ketjen Black and Vulcan CLs with 5 and 50 wt% ionomer as a function of RH. Ketjen Black 30 wt% CL is shown for comparison.

An extent of Pt/carbon coverage by ionomer in the CL can be estimated assuming that the C_{DL} under 20% RH is due to Pt–ionomer and carbon–ionomer interfaces only since a negligible amount of water is present under this RH, and the C_{DL} under 100% RH is the total available interfacial area in the CL.[177]

Using Equation 4.3, the ionomer coverage in the Ketjen Black 5 wt% ionomer CL is estimated to be 3.5%, whereas in Vulcan 5 wt% ionomer it is 9.3%. In Ketjen Black 50 wt% ionomer it is found to be 57%, and in Vulcan 50 wt% ionomer it is 56%; interestingly, also in the standard Ketjen Black 30 wt% ionomer, 55% ionomer coverage is estimated.

$$\theta = \frac{C_{DL(20\%)}}{C_{DL(100\%)}} \cdot 100\% \qquad \textbf{4.3}$$

It is seen that the estimated ionomer coverage in the Vulcan 5 wt% ionomer CL is notably larger than that of the corresponding Ketjen Black-based CL. This effect is attributed to the fact that at the identical ionomer loading a higher coverage is achieved in the Pt/carbon with a lower surface area, such as Pt/Vulcan (SA of Pt/Vulcan is 132 $m^2/g_{(carbon)}$ vs 294 $m^2/g_{(carbon)}$ of Pt/Ketjen Black). The similarity between the ionomer coverage in 30 and 50 wt% ionomer CLs is attributed to the maximum ionomer coverage reached with 30 wt% ionomer, while further addition of ionomer results in an increase of the ionomer layer thickness rather than an increase in the covered interfacial area.

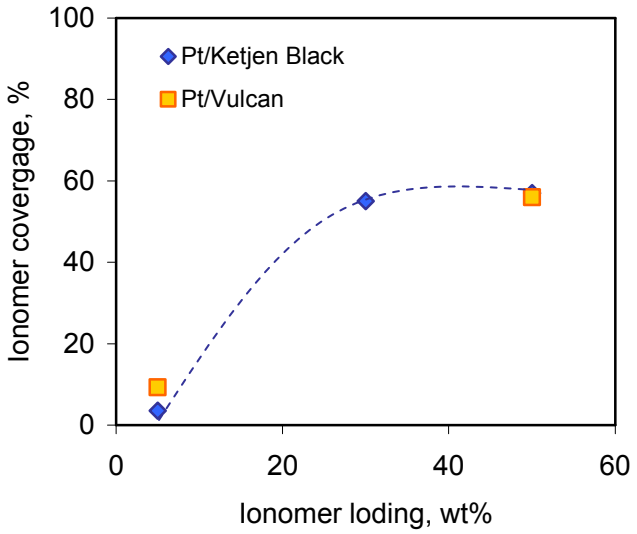

Figure 4.5: Estimated percentage of Pt/carbon surface covered by ionomer as a function of the ionomer wt% loading in Ketjen Black and Vulcan-based CLs.

4.3.2 Proton conductivity

Proton conductivity was estimated using EIS under H_2/N_2 atmosphere, as described in section 1.6.4. Example of Nyquist plots for Ketjen Black and Vulcan-based CLs under 100% RH are shown in Appendix C. Protonic resistance in the CL, R_p, was calculated from the slope of H_2/N_2 high frequency region of a Nyquist plot in the case of 5 wt% CLs and using the transmission line model in the case of 30 and 50 wt% CLs. The thickness of the CLs, determined from SEM, was used to calculate proton conductivity from R_p.

As seen from Figure 4.6, proton conductivity increases with ionomer content from 0.38 – 1.36 mS/cm for 5 wt% ionomer CLs to 4.04 – 5.18 mS/cm for 30 and 50 wt% ionomer CLs under 100% RH. This is attributed to the formation of a

more connected H^+-conducting ionomer network in the CLs as the ionomer content increases. Improvement of proton conductivity is observed with increase in RH in all CLs because water serves as a proton-conducting medium alongside with the ionomer. Interestingly, Vulcan 5 wt% ionomer CL shows an enhanced proton conductivity with increasing RH compared to the Ketjen black 5 wt% CL: 1.36 vs. 0.38 mS/cm in the Ketjen Black 5 wt% ionomer CL under 100% RH. This is somewhat counter-intuitive since the Ketjen Black CL sorbs more water than the Vulcan CL: 0.57 vs. 0.4 $cm^3_{H2O}/g_{(carbon)}$ under ~ 100% RH (Table 3.1 and Figure 3.3), and thus is expected to show an enhanced H^+-conductivity. However, from the microstructural data, it is speculated that the ionomer is distributed on the surface area of the mesopores, which is significantly smaller in Pt/Vulcan than in Pt/Ketjen Black: 132.5 and 294.1 $m^2/g_{(carbon)}$, respectively; as well as the total pore volume that is available for water sorption: 0.86 ± 0.06 and 0.39 ± 0.003 $cm^3/g_{(carbon)}$ for Pt/Ketjen Black and Pt/Vulcan, respectively. Hence, with the identical volume of the ionomer in these CLs, the ionomer is distributed on much lower surface area of the Pt/Vulcan resulting in a more connected ionomer network than in the case of Pt/Ketjen Black CL.

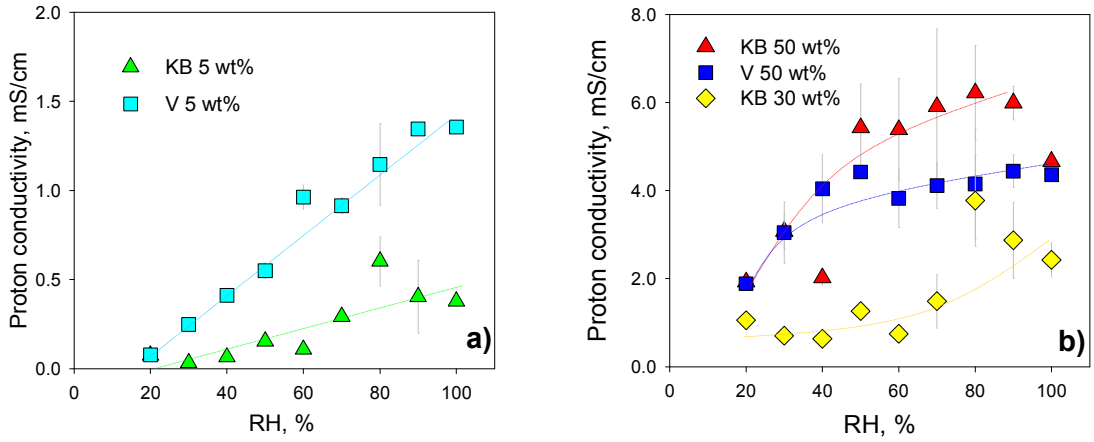

Figure 4.6: Proton conductivity of CLs with a) 5 wt% ionomer loading and b) 50 wt% ionomer loading as a function of RH. Proton conductivity of the standard 30 wt% ionomer Ketjen Black CL is shown for reference.

With increasing RH, water content in the CLs increases and adsorbed water provides linkages between disconnected patches of ionomer, enhancing the connectivity of the ionomer-water H^+-conducting network. The connectivity can be expressed as a ratio of the volume of ionomer + water to the mesoporous surface area of the corresponding Pt/carbon, $V_{(I+H2O)}/SA_{(meso)}$. This ratio is found to be 34 for the Vulcan 5 wt% ionomer CL and 21 for the Ketjen Black 5wt% ionomer CL under 100% RH, which is in agreement with observed enhanced proton conductivity of Vulcan 5 wt% ionomer CL.

Proton conductivity of both 30 and 50 wt% ionomer CLs also increases with relative humidity from ~ 2 mS/cm under 20% RH to ~ 5 mS/cm under 100% RH. The values for proton conductivity of CLs reported here are in good agreement with literature data. Proton conductivity estimated by Havranek[176] for 12 vol%

ionomer Vulcan-based CL is 2.6 mS/cm that is comparable to 4.0 mS/cm for the Ketjen Black 30 wt% (i.e., 13 vol%) ionomer CL.[176] The values reported by Boyer et al.[178] are somewhat higher, in the range of 10 – 20 mS/cm for 15 vol% ionomer CLs. The discrepancies can be attributed to the differences in the CL preparation procedures as well as to variations in proton resistance measurements and data extraction methodologies.

It is interesting to investigate the intrinsic proton conductivity of the ionomer in the CL. This can be done by normalizing proton conductivity of the CL to the volume fraction of ionomer in the CL. The volume fraction of ionomer is calculated from the known ionomer loading, density of ionomer and the thickness of the CL (as shown in Appendix A). The values of the proton conductivity of the CL and the ionomer conductivity are compared in Table 4.1.

Table 4.1: Effective proton conductivity of CLs compared to the CL proton conductivity normalized to volume of the ionomer in the CLs

CL type	$V_{ionomer}$, $cm^3/g_{(carbon)}$	V fraction ionomer, vol%	σ_{H+}, 100% RH mS/cm	$\sigma_{H+/Vionomer\ CL}$, 100% RH mS/cm	σ_{H+}, 20% RH mS/cm	$\sigma_{H+/Vionomer\ CL}$, 20% RH mS/cm
KB 5 wt%	0.052	1.6	0.38 ± 0.02	23	0.07 ± 0.02	4.5
KB 30 wt%	0.41	13	4.04 ± 0.65	31	1.75 ± 0.65	13.5
KB 50 wt%	0.96	46	5.18 ± 0.03	17	2.14 ± 0.04	7.0
V 5 wt%	0.052	2.5	1.36 ± 0.30	82	0.08 ± 0.002	4.7
V 50 wt%	0.096	57	4.4 ± 0.04	14	1.9 ± 0.12	3.7

The ionomer conductivity in the CL is significantly lower than that of the bulk Nafion membrane that is ~ 100 mS/cm (100% RH, 80 ºC) with only the Vulcan 5

wt% ionomer case approaching the Nafion bulk conductivity value. The difference could be attributed to 1) disconnectivity of the ionomer chains within the CL, which leads to the disruption of proton conducting path, 2) the lower water uptake capacity of the ionomer layer in the CL, which might be too thin for the phase-separation and formation of water-filled proton conducting channels within the ionomer layer.

4.3.3 Polarization performance of Ketjen Black and Vulcan-based CLs with 5 wt% ionomer content

Representative O_2 polarization curves of Ketjen black and Vulcan CLs with 5 wt% ionomer under 100 %RH are shown in Figure 4.7. The decrease in ionomer loading from 30 to 5 wt% results in the drastic drop in performance in current density region < 0.1 A/cm^2. This is attributed to lower ESAs of these CLs compared to the standard Ketjen Black 30 wt% ionomer: 27 and 39 m^2/g_{Pt} for Vulcan and Ketjen Black 5 wt% ionomer CLs, respectively, vs. 49 m^2/g_{Pt} for the standard Ketjen Black 30 wt% CLs. Moreover, a sufficiently connected H^+-conducting network is necessary for protons to reach Pt particles in order for ORR to happen, however, ionomer loading of 5 wt% lies significantly below the percolation threshold (~ 30 wt%) leading to impediment of proton transport, and presumably lower proton concentration at the reaction sites. This is reflected in low proton conductivity values as determined in Section 4.3.2: 0.38 and 1.4 mS/cm for Ketjen Black and Vulcan 5 wt% ionomer CLs, respectively. Moreover, due to the low ionomer loading, reaction penetration depth could be reduced and shifted toward the membrane side of the electrode. In the high current density

region, > 2 A/cm^2, minimal mass transport losses are observed, especially in the case of Vulcan 5 wt% ionomer CL. This is attributed to a large pore volume available for gas transport in the CLs with 5 wt% ionomer: 0.59 and 0.33 $cm^3/g_{(carbon)}$ for Ketjen Black and Vulcan CLs, respectively, as is seen from Table 2.2 and Table 4.2. A slightly enhanced performance of Vulcan 5 wt% CL in this current density region is attributed to the lower water retention properties of Pt/Vulcan due to the lower fraction of pores < 20 nm, which become filled with water by capillary condensation and increase pore trapping and water retention, as described in Section 2.3.3. The absence of these pores in Pt/Vulcan facilitates removal of water produced on the cathode hence providing O_2 access to the reaction sites.

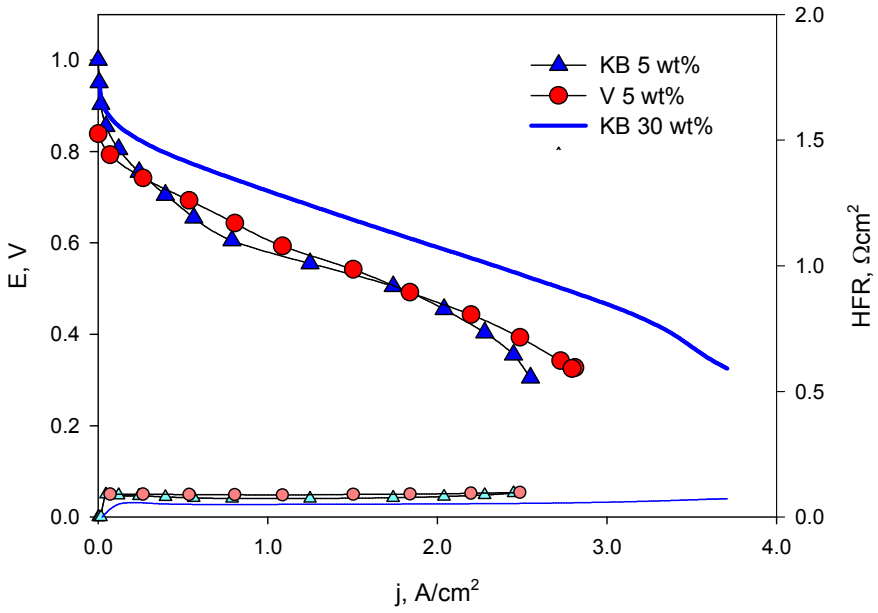

Figure 4.7: Polarization curves for Ketjen Black and Vulcan-based 5 wt% ionomer loading CLs under 100% RH, H_2/O_2, 2:3 stoich, atm, 80 ºC, non-IR-corrected. The standard Ketjen Black 30 wt% ionomer CL is shown for reference.

However, given such a low ionomer loading, the performance of these CLs is surprisingly good. This is attributed to the abundance of water in the CL under 100% RH that functions as a proton-conducting medium and increases the ESA, as shown in Sections 4.3.1 and 4.3.2.

The slight differences observed in performance between Ketjen Black and Vulcan CLs might be due to the differences in ESA, proton conductivity and water sorption and retention properties as shown Table 4.2. Ketjen Black CLs posses high ESA (39 vs 27 m^2/p_{Pt}), but lower proton conductivity (0.38 vs. 1.36 mS/cm) than the Vulcan CLs. Lower proton conductivity in the case of Ketjen

Black-based CL is attributed to the poorer connectivity of the H^+-conducting phase (ionomer + water). The connectivity is expressed as a ratio of volume of water and ionomer to the mesoporous surface area of Pt/carbon, where ionomer is distributed, $V_{(I+H2O)}/SA_{(meso)}$.

Table 4.2: Characteristics of Ketjen black and Vulcan-based CL with 5 wt% ionomer in 100% RH.

CL type	$V_{ionomer}$, $cm^3/g_{(carbon)}$	ESA, m^2/g_{Pt}	σ_{H+}, mS/cm	V_{H2O}, $cm^3/g_{(carbon)}$	V_{pore}>2nm, $cm^3/g_{(carbon)}$	$V_{(H2O+I)}$ / $SA_{(meso)}$, $*10^{-4}$ cm^3/m^2
KB 5 wt%	0.052	38.5 ± 0.77	0.38 ± 0.02	0.57	0.59 ± 0.12	21
V 5 wt%	0.052	27.1 ± 2.78	1.36 ± 0.30	0.40	0.33 ± 0.05	34
KB 30 wt%	0.41	49.1 ± 1.14	4.04 ± 0.65	0.61	0.35 ± 0.01	35

Note: values of ESA, σ_{H+} and V_{H2O} don't take into account water produced on the cathode during FC operation. V_{pore} is in CL determined from N_2 adsorption (dry condition). $SA_{(meso)}$ is the SA of pores > 2 nm of Pt/carbon determined from N_2 adsorption (refer to Table 2.1).

The value of $V_{(I+H2O)}/SA_{(meso)}$ is 34 for the Vulcan 5 wt% ionomer CL, which is nearly identical with the standard Ketjen Black 30 wt% ionomer. In the case of Ketjen Black 5 wt% ionomer it is significantly lower – 21. Thus, losses in the performance of the CLs with extremely low ionomer loading can be attributed to the interplay of the low ESA and the low fraction of the proton-conducting phase in the CL.

Under dry operating conditions, water that benefits proton conduction and the ESA is removed from the CL, and a much more significant drop in performance is observed as shown in Figure 4.8. Moreover, a clear difference in performance between these two CLs is seen with the Ketjen Black 5 wt% ionomer CL

experiencing a drastic drop in performance in the low current density region (< 0.1 A/cm^2).

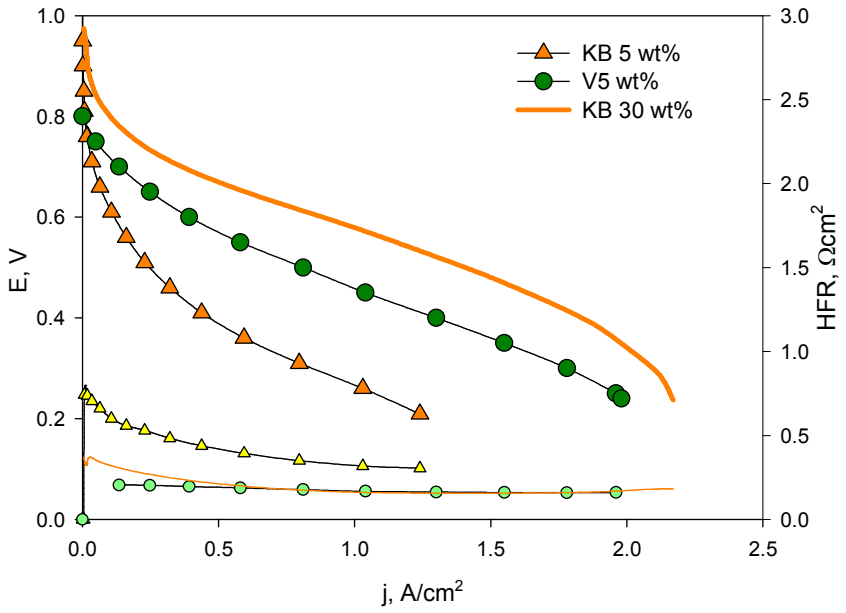

Figure 4.8: Polarization curves for Ketjen Black and Vulcan-based 5 wt% ionomer loading CLs under 20% RH, H_2/O_2, 2:3 stoich, atm, 80ºC, non-IR-corrected. The standard Ketjen Black 30 wt% ionomer CL is shown for reference.

As volume of water in the Ketjen Black 5 wt% ionomer CL decreases from 0.57 (100% RH) to 0.07 $cm^3/g_{(carbon)}$ (20% RH), the ESA drops from 38.5 to 5.3 m^2/g_{Pt}. In the case of the Vulcan 5 wt% ionomer CL, volume of water decreases from 0.4 (100% RH) to 0.06 $cm^3/g_{(carbon)}$ (20% RH) causing a reduction of the ESA from 27.1 to 7.6 m^2/g_{Pt}. The reduction of ESAs is assumed the major contributor to the drastic drop in performance in the low current density region. Moreover, a disruption of ionomer-water H^+-conducting network occurs. This effect is exacerbated in the Ketjen Black CL due to the fact that it possesses a

much larger surface area (i.e., pore volume) on which proton conducting phase is distributed. Ionomer contents in both CLs are identical and water contents are nearly the same under 20% RH (Table 4.3 and Figure 3.3). This suggests a more "disconnected" ionomer network in the case of the Ketjen Black CL compared to the Vulcan CL under these operating conditions. Disconnectivity is expressed as the $V_{(I+H2O)}/SA_{(meso)}$ ratios, which is 8.5 in the case of the Vulcan 5 wt% ionomer CL and 4.1 in the case of the Ketjen Black 5 wt% ionomer CL, Table 4.3. Both of these values are however much lower than in the Ketjen Black 30 wt% ionomer CL – 18, correlating well to the greater polarization losses.

Table 4.3: Characteristics of Ketjen black and Vulcan-based CL with 5 wt% ionomer in 20% RH.

CL type	$V_{ionomer}$, $cm^3/g_{(carbon)}$	ESA, m^2/g_{Pt}	σ_{H+}, mS/cm	V_{H2O}, $cm^3/g_{(carbon)}$	V_{pore}>2nm, $cm^3/g_{(carbon)}$	$V_{(H2O+I)}$ / $SA_{(meso)}$, $*10^{-4}$ cm^3/m^2
KB 5 wt%	0.052	5.3 ± 0.3	0.07 ± 0.02	0.07	0.59 ± 0.12	4.1
V 5 wt%	0.052	7.6 ± 0.4	0.08 ± 0.002	0.06	0.33 ± 0.05	8.5
KB 30 wt%	0.41	21.6 ± 0.72	1.75 ± 0.65	0.11	0.35 ± 0.01	18

Note: values of ESA, σ_{H+} and V_{H2O} don't take into account water produced on the cathode during FC operation. V_{pore} is in CL determined from N_2 adsorption (dry condition). $SA_{(meso)}$ is the SA of pores > 2 nm of Pt/carbon determined from N_2 adsorption (refer to Table 2.1).

A good correlation is observed between the $V_{(I+H2O)}/SA_{(meso)}$ ratios and the ionomer coverage estimated from the double layer capacitance in Section 4.3.1. The percentage of Pt/carbon surface covered by ionomer in 5 wt% ionomer CLs is 3.5 and 9.3% for the Ketjen Black and the Vulcan-based CL, respectively, whereas it is 55% for the Ketjen Black 30 wt% ionomer CL. The larger the ionomer coverage, the more connected proton-conducting network is formed and

a larger fraction of Pt particles is expected to be in contact with ionomer. This is manifested in increasing ESA as the ionomer coverage increases as shown in Figure 4.9.

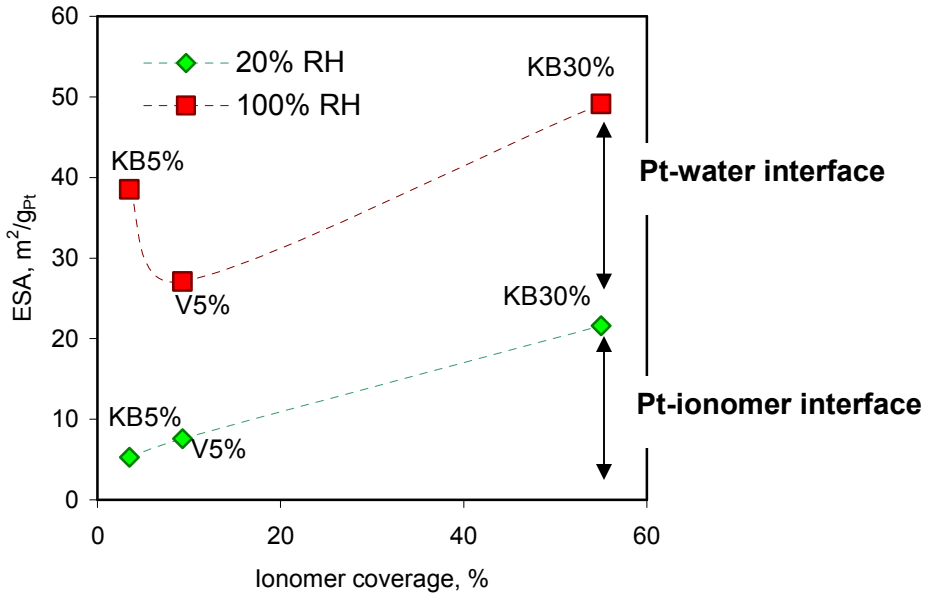

Figure 4.9: ESA as a function of ionomer coverage in 20 and 100% RH for Ketjen Black and Vulcan based CLs.

It is assumed that only small amount of water is present in the ionomer at 20% RH - approximately two water molecules per each SO_3^- site, as was reported for Nafion 117 by Zawodzinski et al.[175] Thus, it is stated that measured ESAs values under 20% RH are only due to the Pt-ionomer interface. The increase in the ESA between 20 to 100% RH is attributed to the Pt-water interface that grows with increase of RH as water is adsorbed and condensed in the catalyst layer. The significantly larger ESA value under 100% RH is observed

in the Ketjen Black 5 wt% ionomer CL compared to the Vulcan 5 wt% ionomer CL despite identical ionomer coverage. This could be attributed to the microstructure-specific location of a large fraction of Pt particles in the pores < 20 nm inside agglomerates of Ketjen Black carbon that are filled with water under 100% RH.

Charge and mass transport resistances are investigated by EIS under a H_2/O_2 atmosphere in order to deconvolute the effect of the ionomer loading on the kinetic and mass transport regions of the V-I curves. In Figure 4.10a,b, the sum of charge and mass transfer resistances, $R_{CT}+R_{MT}= R_T$, are plotted as a function of current density in the 20 – 100% RH range for Ketjen Black and Vulcan 5 wt% ionomer CLs. The total resistance, R_T, decreases with current density. At very low current densities (0.04 A/cm^2), where the kinetics of ORR is the rate limiting step, mass transport limitations can be neglected and the observed resistance is attributed solely to the charge transfer resistance.[92] Thus, R_{CT} values for the CLs are estimated at the current density of 40 mA/cm^2 and shown in Figure 4.11. It is seen that R_{CT} decreases with increasing RH. This is attributed to the growing ESA as water is adsorbed in the CL and to the enhanced H^+ transport in the hydrated ionomer to the reaction sites. In the high current density region, no mass transport limitations are observed, as the resistance stays nearly constant with increasing current density over 1.0 – 2.5 A/cm^2 range. A slight rise at 2.5 A/cm^2 is presumably due to the contribution from the dehydration of the anode/anode side of the membrane at such a high current density, which manifests as a second semi-circle in the low frequency region (APPENDIX B).

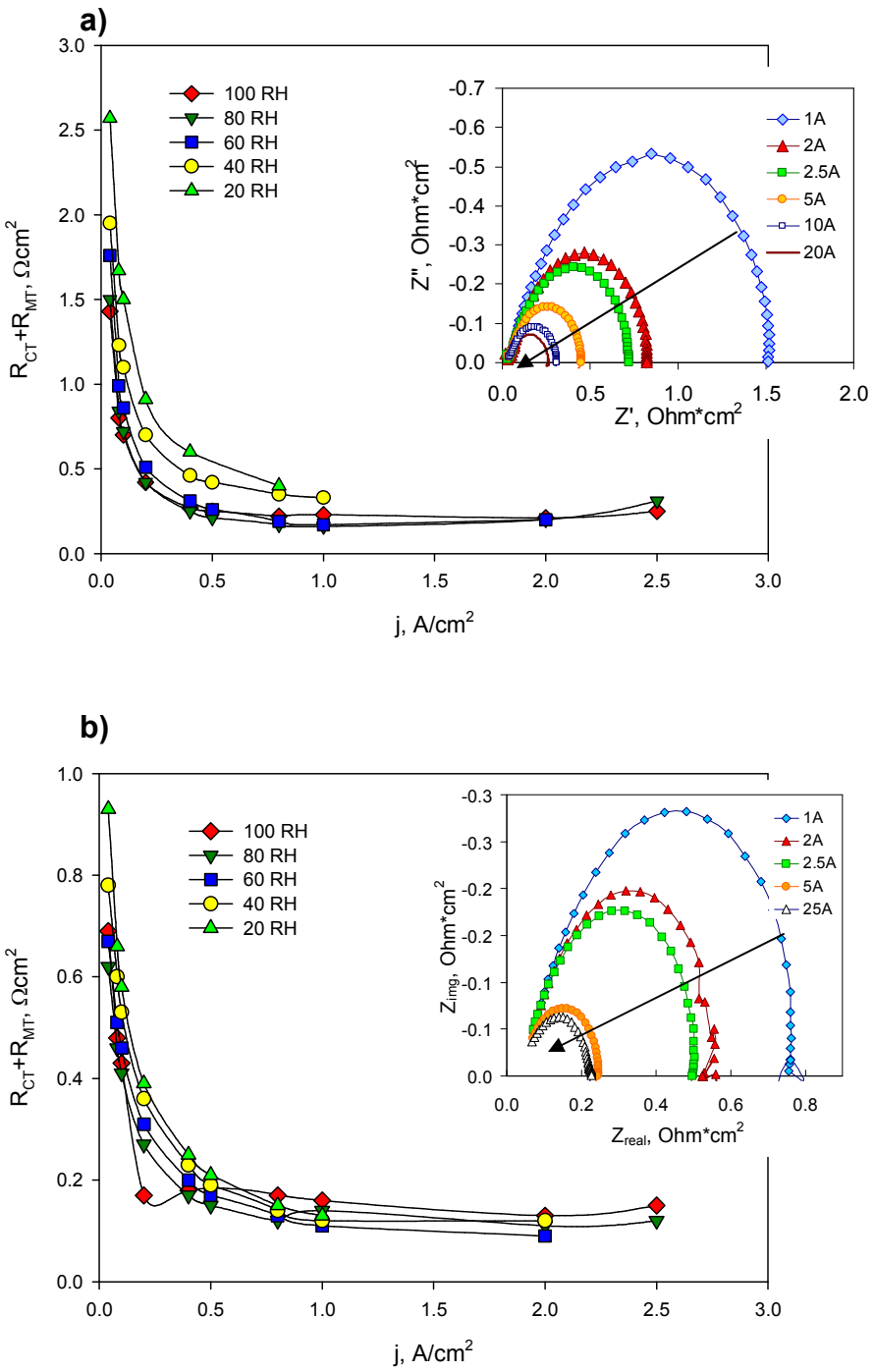

Figure 4.10: Sum of charge and mass transfer resistance of a) Ketjen Black 5 wt% ionomer CL and b) Vulcan 5 wt% ionomer CL as a function of current density in the range of relative humidities. Inset – EIS plots in 100 %RH showing increase in total resistance with increase in current density.

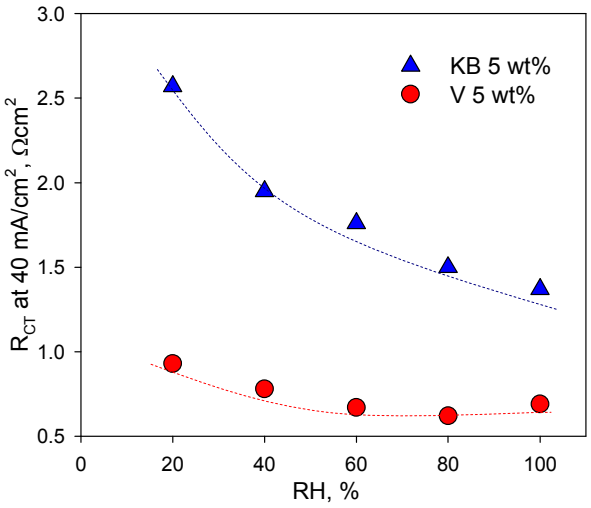

Figure 4.11: Charge transfer resistance determined from EIS as a function of RH for Ketjen Black and Vulcan 5 wt% ionomer CLs.

The lower values of R_{CT} in the case of Vulcan 5 wt% ionomer are a result of a complex interplay of the structural and electrochemical properties of the CLs. The ESA of the Ketjen Black-based CL is higher under 100% RH but is lower under 20% RH, Table 4.2 and Table 4.3. Since oxygen access to the reaction sites is assumed to be unhindered in these CLs at this particular current density, it is speculated that proton transport/ proton concentration at Pt interface is the reaction rate controlling process. Proton conductivity of Vulcan 5 wt% CL is higher in both dry and humidified operating conditions than in the Ketjen Black 5 wt% ionomer CL (1.36 vs. 0.38 mS/cm, 100% RH, and 0.08 vs. 0.02 mS/cm, 20% RH). The proton conducting phase to surface area ratios are also higher in

the case of Vulcan 5 wt% CL (34 vs. 21, 100% RH, and 8.5 vs. 4.1, 20% RH) as well as the ionomer coverage (9.3% vs. 3.5%).

From the $V_{(I+H2O)}/SA_{(meso)}$ ratio, the thickness of ionomer layer in the CL can be estimated. Assuming homogenous distribution of the ionomer on Pt/carbon surface, ionomer layer thickness was calculated to be 0.18 nm for KB 5 wt% ionomer CL and 0.4 nm for Vulcan 5 wt% ionomer CL (mesoporous SA of Pt/carbon are 294.1 and 132.5 $m^2/g_{(carbon)}$ for Ketjen Black and Vulcan, respectively). For Ketjen Black 30 wt% ionomer, the ionomer thickness is estimated to be 1.4 nm. Although this analysis provides an interesting insight, the values are very likely to be underestimated because the surface area of Pt/carbon used in calculations is that of all pores > 2 nm. Yet, as has been shown in the microstructure studies, ionomer is distributed in the pores > 20 nm; hence a smaller surface area is available for ionomer distribution, which would result in a thicker ionomer layer than estimated here. These findings however support the assumption that the ionomer layer in the CL is too thin for formation of water-filled proton conducting clusters as in bulk Nafion membrane, which were reported to be ~ 3 nm in diameter.[101]

Based on the findings reported in this section, lowering of ionomer content in the CL leads to a loss in performance due to lower ESAs and an insufficient H^+-conducting network; this effect is observed in the low to intermediate current density region of the IV curve. Under fully humidified operating conditions, the type of carbon does not seem to have a significant impact due to an abundance of water in the CL that, to a certain degree, compensates for low ionomer

content. In dry operating conditions, however, the lower SA Vulcan shows a notably higher performance due to a more connected H^+-conducting network, which is due to the proportionally higher ionomer coverage.

4.3.4 Polarization performance of Ketjen Black and Vulcan-based CLs with 50 wt% ionomer content

An excess of ionomer in the CL leads to the mass transport issues because of the blockage of porous space in the CL required for gas transport.[93] Although it can be argued that 50 wt% ionomer CLs are of little practical significance, it is useful to help obtain a fundamental understanding of the effects of ionomer and carbon in the CL on performance of the fuel cell. O_2 polarization curves of Ketjen Black and Vulcan CLs with 50 wt% ionomer loading in 100% RH are shown in Figure 4.7. The increase in ionomer loading from 30 to 50 wt% results in a tremendous loss in performance due to severe gas transport limitations that manifest even at very low current densities (< 0.1 A/cm^2). Despite the adequate ESA and proton conductivity in CLs (50.4 m^2/g_{Pt} and 5.2 mS/cm for Ketjen Black 50 wt% ionomer CL; and 37.0 m^2/g_{Pt}, and 4.4 mS/cm Vulcan 50 wt% ionomer CLs), Table 4.4, high ionomer and water content hinder the reactant gases from reaching the active sites through the ionomer and water filled pores. Pore volume is negligibly small in both CLs: 0.08 and 0.02 $cm^3/g_{(carbon)}$ for Ketjen Black and Vulcan-based CLs, respectively. The extent of pore filling can be estimated from the $V_{(I+H2O)}/SA_{(meso)}$ ratio, Table 4.4. The value of 140 in the Vulcan CL and of 67 in the Ketjen Black CL are equivalent to ~ 14 nm and 7 nm thick layer of ionomer + water distributed evenly on the entire mesoporous SA of Pt/carbon. Such a

thick layer of ionomer + water is expected to block the majority of the pores.

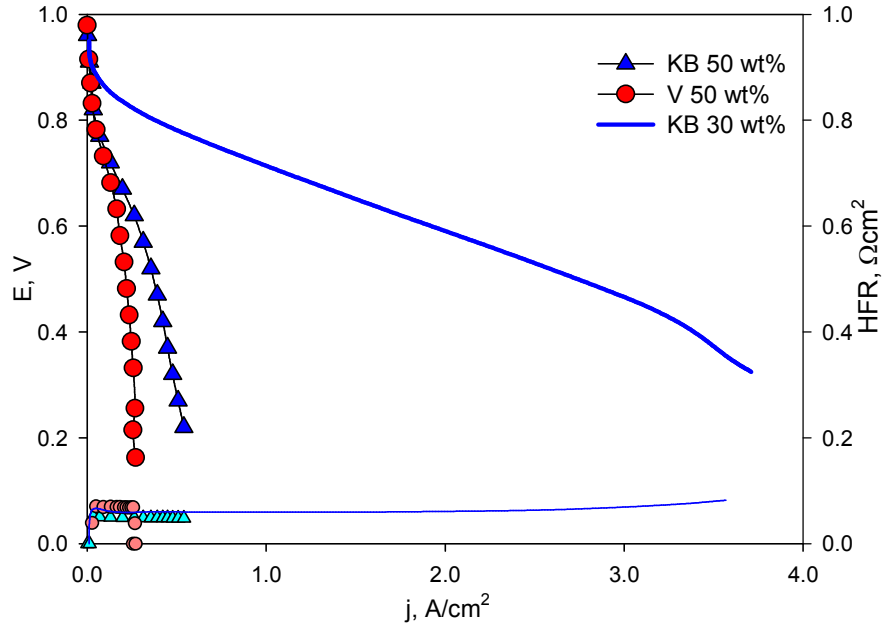

Figure 4.12: Polarization curves for Ketjen Black and Vulcan-based 50 wt% ionomer loading CLs in 100 %RH, H_2/O_2, 2:3 stoich, atm, 80ºC, non-IR-corrected. The standard Ketjen Black 30 wt% ionomer CL is shown for reference.

Table 4.4: Characteristics of Ketjen black and Vulcan-based CL with 50 wt% ionomer in 100% RH.

CL type	$V_{ionomer}$, $cm^3/g_{(carbon)}$	ESA, m^2/g_{Pt}	σ_{H+}, mS/cm	V_{H2O}, $cm^3/g_{(carbon)}$	V_{pore}>2nm, $cm^3/g_{(carbon)}$	$V_{(H2O+I)}$ / $SA_{(meso)}$, $*10^{-4}$ cm^3/m^2
KB 50 wt%	0.96	50.4 ± 2.0	5.18 ± 0.03	1.02	0.08 ± 0.01	67
V 50 wt%	0.96	37.0 ± 1.6	4.4 ± 0.04	0.89	0.02 ± 0.001	140

Note: values of ESA, σ_{H+} and V_{H2O} don't take into account water produced on the cathode during FC operation. V_{pore} is in CL determined from N_2 adsorption (dry condition). $SA_{(meso)}$ is the SA of pores > 2 nm of Pt/carbon determined from N_2 adsorption (refer to Table 2.1).

Under dry operating conditions, when little water is present in the CLs, the performance deteriorates further, as shown in Figure 4.13. Despite the relatively high values of the ESA (46 and 35 m^2/g_{Pt} for Ketjen Black and Vulcan CLs, respectively) and adequate proton conductivity (2.1 and 1.9 mS/cm for Ketjen Black and Vulcan CLs, respectively), Table 4.5, dramatic losses are observed at current densities < 0.1 A/cm^2. Although evaporation of water provides more available pore space for gas transport, oxygen penetration through the dry ionomer layer decreases significantly. Oxygen permeability through a dry Nafion film is an order of magnitude smaller than through a hydrated film: 2.84 x 10^{-15} mol/s/m/Pa in dry Nafion vs. 2.62 x 10^{-14} mol/s/m/Pa in hydrated Nafion, as estimated from data provided by Sakai et al.[19] Thus, performance loss in 50 wt% ionomer CLs is attributed mainly to oxygen transport limitations to the reaction sites, in particular, due to decrease of the available pore space for gas transport and due to reduced oxygen permeability through the ionomer layer.

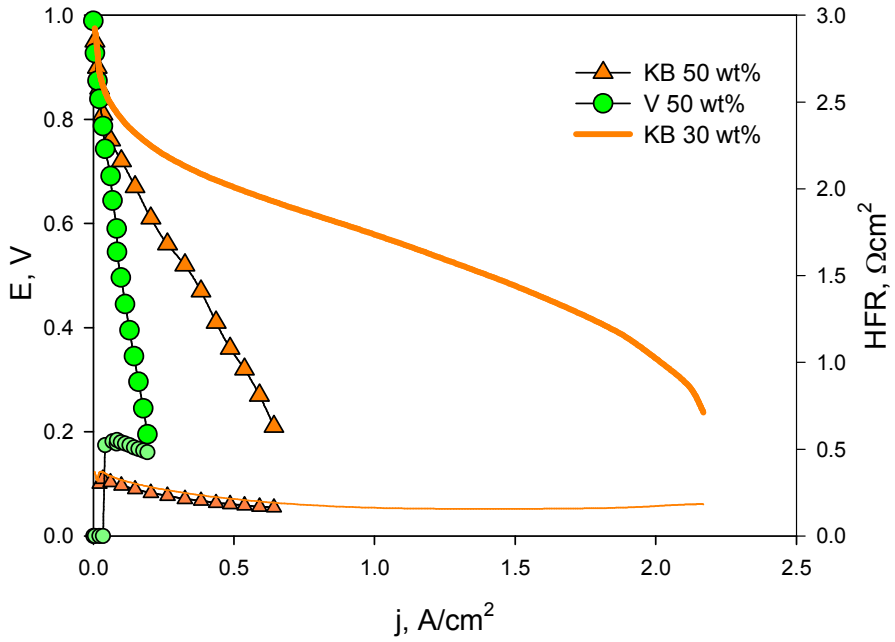

Figure 4.13: Polarization curves for Ketjen Black and Vulcan-based 50 wt% ionomer loading CLs under 20% RH. H_2/O_2, 2:3 stoich, atm, 80 ºC, non-IR-corrected. The standard Ketjen Black 30 wt% ionomer CL is shown for reference.

Table 4.5: Characteristics of Ketjen black and Vulcan-based CL with 50 wt% ionomer in 20% RH.

CL type	$V_{ionomer}$, $cm^3/g_{(carbon)}$	ESA, m^2/g_{Pt}	σ_{H+}, mS/cm	V_{H2O}, $cm^3/g_{(carbon)}$	V_{pore}>2nm, $cm^3/g_{(carbon)}$	$V_{(H2O+I)}$ / $SA_{(meso)}$, $*10^{-4}$ cm^3/m^2
KB 50 wt%	0.96	45.8 ± 1.89	2.14 ± 0.05	0.13	0.08 ± 0.01	37
V 50 wt%	0.96	35.3 ± 0.21	1.9 ± 0.12	0.18	0.02 ± 0.001	86

Note: values of ESA, σ_{H+} and V_{H2O} don't take into account water produced on the cathode during FC operation. V_{pore} is in CL determined from N_2 adsorption (dry condition). $SA_{(meso)}$ is the SA of pores > 2 nm of Pt/carbon determined from N_2 adsorption (refer to Table 2.1).

The negative impact of 50 wt% ionomer loading on mass transport in the CLs is clearly seen from EIS and $R_{CT}+R_{MT}$ plots in Figure 4.14. The total resistance

decreases at very low current densities but starts increasing at ~ 0.1 A/cm^2 current density in both CLs in all RH conditions. This is due to the limitations in O_2 permeation to the reaction sites through the ionomer and ionomer + water filled pores. The effect is exacerbated under 100% RH due to the additional pore blocking by condensed water and by the product water. It is clearly seen in the insets. The diameter of the semi-circle starts increasing at currents > 5 A, corresponding to > 200 mA/cm^2. This effect is somewhat diminished at lower RH due to a lower water content in the CLs, which then can better accommodate the product water to some extent. Overall, R_{CT} of 50 wt% ionomer CLs is higher than of the standard 30 wt% ionomer CL, as shown in Figure 4.15. In the case of Vulcan 50 wt% ionomer CL, R_{CT} and the total R_{CT}+R_{MT} is significantly higher than in the Ketjen Black 50 wt% CL, Figure 4.15, because of the more pronounced blocking of the pore space, which is due to initially lower surface area and pore volume of Pt/Vulcan for ionomer and water distribution.

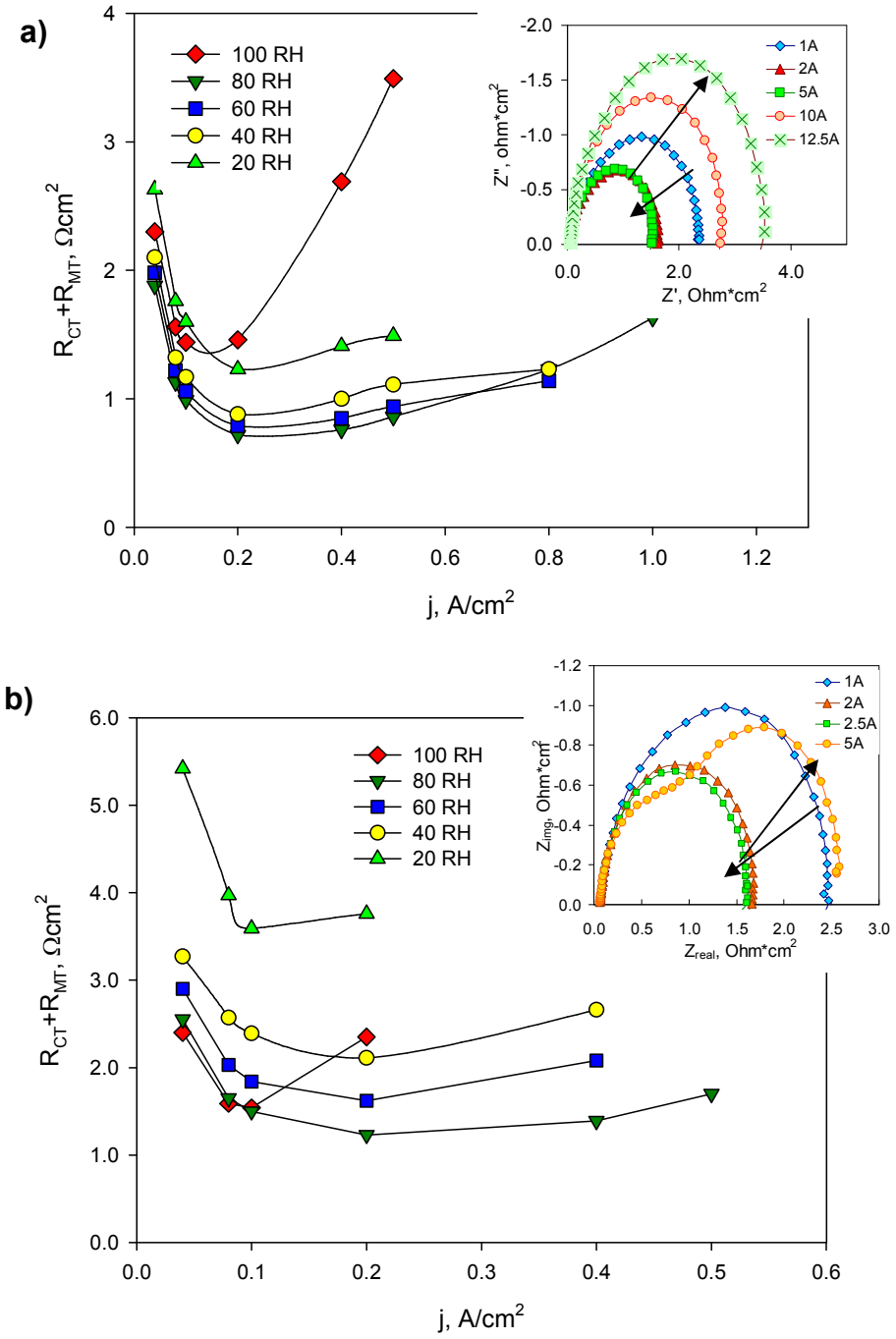

Figure 4.14: Sum of charge and mass transfer resistance of a) Ketjen Black 50 wt% ionomer CL and b) Vulcan 50 wt% ionomer CL as a function of current density in the range of relative humidities. Inset – EIS plots in 100% RH showing increase in total resistance with increase in current density.

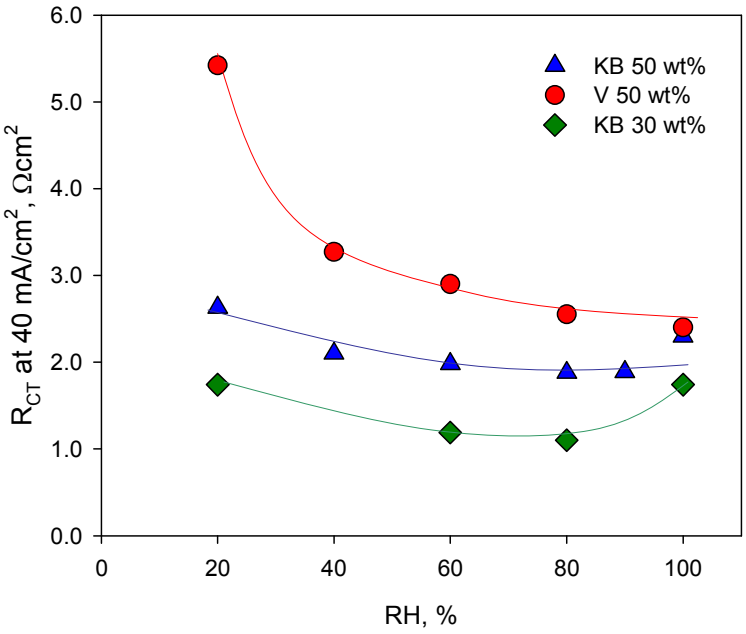

Figure 4.15: Charge transfer resistance determined from EIS as function of RH for Ketjen Black and Vulcan-based CLs with 50 wt% ionomer CLs. The standard 30 wt% ionomer CL is shown for reference.

Using a similar method to that described in Section 4.3.3, the ionomer thickness is estimated to be 3.3 nm and 7.2 nm for Ketjen Black and Vulcan 50 wt% ionomer CLs, respectively (for reference: ionomer thickness is 1.4 nm in Ketjen Black 30 wt% ionomer). The 7.2 nm thick ionomer layer in the case of Vulcan-based CL suggests that pores under 15 nm diameter are completely filled by ionomer. Estimated values of ionomer thickness and extent of pore blocking of these CLs support the assumption that the optimal ionomer loading for the Vulcan-based CLs must be significantly lower than for the Ketjen Black-based CLs. The $V_{(I+H2O)}/SA_{(meso)}$ ratio seems to be a crucial value for estimating the optimal ionomer loading. Assuming that this ratio in the case of 30 wt% ionomer on Pt/Ketjen Black is optimal for this particular carbon support with 294

$m^2/g_{(carbon)}$ of mesoporous area, the optimal ionomer loading for the Pt/Vulcan can be calculated; it is found to be ~ 15 wt%.

4.3.5 Asymmetrical MEAs with Ketjen Black and Vulcan XC-72-based CLs as an anode or a cathode.

Summarizing findings in sections 2.3 and 3.3, a high ionomer loading in the CL (≥ 30 wt%) and a carbon with a broad PSD, Ketjen Black type, facilitate sorption and retention of water in the CL, and thus are believed to be beneficial for the anode CL, which is prone to the dehydration. On the other hand, a lower ionomer loading (< 30 wt%) and a carbon with a narrower PSD in the mesoporous range, i.e., Vulcan type, facilitates water removal and hence is expected to be beneficial for the cathode CL.

Based on these considerations, the fuel cell performance of MEAs comprising of the anode and the cathode of different compositions, i.e., type of carbon and ionomer loading, is evaluated. As proposed, an asymmetrical MEA with a hydrophilic anode (Ketjen Black 30 wt% ionomer CL (KB30)) and a hydrophobic cathode (Vulcan 5 wt% ionomer CL (V5)) is used to assess the fuel cell performance. A “mirror image” MEA with a hydrophobic anode and a hydrophilic cathode (V5KB30 – anode/cathode) is tested to verify the presented hypothesis. Fuel cell performance curves of KB30V5 and V5KB30 MEAs under 100% RH are shown in Figure 4.16.

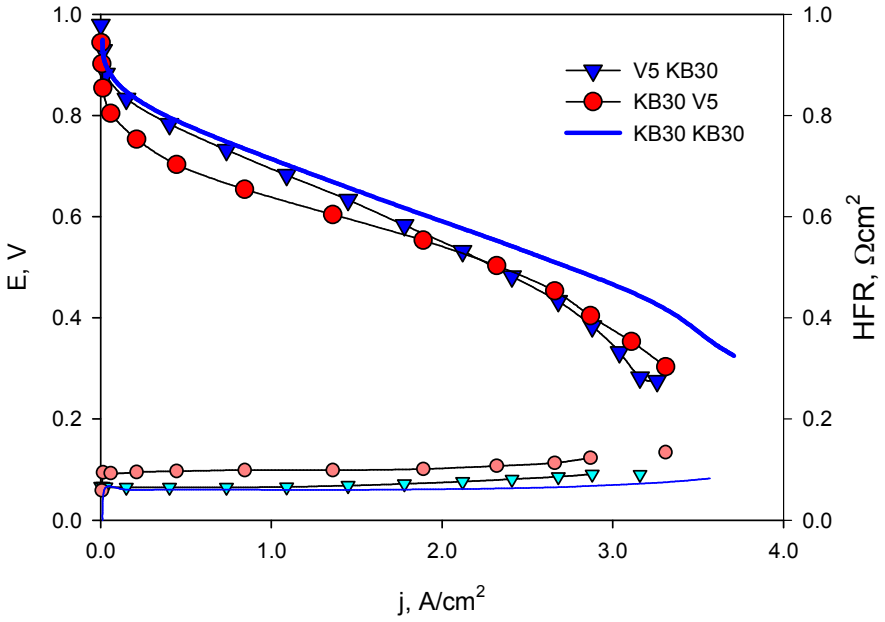

Figure 4.16: Polarization curves for KB30V5 and V5KB30 MEAs under 100% RH, H_2/O_2, 2:3 stoich, atm, 80 ºC, non-IR-corrected. The standard Ketjen Black 30 wt% ionomer CL is shown for reference.

It is seen that both asymmetrical MEAs perform very similar to the standard Ketjen Black 30 wt% ionomer MEA despite a significantly lower ionomer loading on one of the electrodes. As predicted, KB30V5 seems to show a slight enhancement in the mass transport region, however, a large loss in the kinetic and Ohmic region, similar to that seen in the symmetrical 5 wt% ionomer MEAs, is observed. This loss is attributed to the low ESA (27.1 vs. 49.1 m^2/g_{Pt} for V5 and KB30 electrodes, respectively) and a lower proton conductivity (1.36 vs. 4.04 mS/cm for V5 and KB30 electrodes, respectively) of the Vulcan 5 wt% ionomer cathode, despite its beneficial effect on water removal from the cathode.

On the other hand, V5KB30 MEA performs nearly identically to the standard KB30KB30 in the low current density region and diverges at the current density of ~ 1A/cm^2. The inferior performance of V5KB30 MEA compared to the standard 30 wt% ionomer MEA in the intermediate to the very high current density regions is attributed to the disruption of H^+-conducting network on the anode due to dehydration of the anode and the membrane in the high current density region (1 – 3.5 A/cm^2) by electroosmotic drag. This suggests that dehydration of the anode seems to be the major cause of performance deterioration in the high current densities under operation in oxygen as opposed to the flooding of the cathode. At such high current density (> 1 A/cm^2), the EOD flux from the anode is intensified; additionally, a significant amount of heat is generated on the cathode, which leads to faster water evaporation rates from the cathode and dehydration of the anode. Yet, mass transport limitations due to the flooding of the cathode are evident under operation in air, when gas permeation to the reaction sites becomes a rate limiting process. In this case, mass transport limitation are due to flooding, and the V5 cathode demonstrates an enhanced performance in the high current density region compared to the KB30 cathode as shown in Figure 4.17.

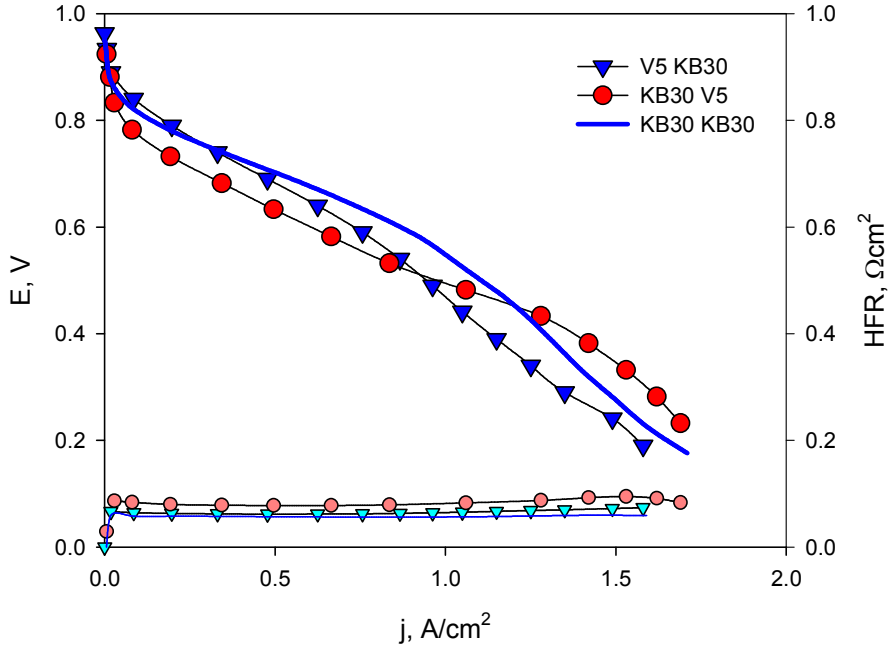

Figure 4.17: Air polarization curves for KB30V5 and V5KB30 MEAs in 100 %RH, H_2/Air, 2:3 stoich, atm, 80 ºC, non-IR-corrected. The standard Ketjen Black 30 wt% ionomer CL is shown for reference.

Despite the losses in the kinetic region, similar to those observed under operation in O_2, a notably higher performance in the current densities > 1 A/cm^2 is observed in the case of KB30V5 compared to V5KB30 and the standard KB30KB30 due to enhanced water removal properties of Vulcan 5 wt% ionomer cathode.

In dry operating conditions (20% RH), reduced water content in the CL has a significant impact on the performance of MEAs as shown in Figure 4.18. KB30V5 MEA suffers a drastic loss in the kinetic region at the current densities < 0.1 A/cm^2. This is attributed to the decrease in the ESA from 27.1 to 7.6 m^2/g_{Pt} and

disruption of H^+-conducting network under low RH condition that is reflected in a decrease of proton conductivity from 1.36 to 0.08 mS/cm, refer to Table 4.2 and Table 4.3. The performance of the V5KB30 MEA is significantly higher under this operating condition and is nearly identical to the performance of the standard KB30KB30 MEA. This is attributed to a relatively high ESA of 21.6 m^2/g_{Pt} and proton conductivity of 1.75 mS/cm under 20% RH in the KB 30 wt% ionomer cathode. The $V_{(I+H2O)}/SA_{(meso)}$ ratio is twice as large in KB30 cathode than in the V5 cathode: 18 vs. 8.5. Interestingly, under this operating condition, a much lower ionomer content Vulcan 5 wt% ionomer anode does not seem to have an impact on performance compared to the Ketjen Black 30 wt% anode in the standard MEA. This suggests that under dry operating condition, the cathode plays a major role in controlling the overall fuel cell performance.

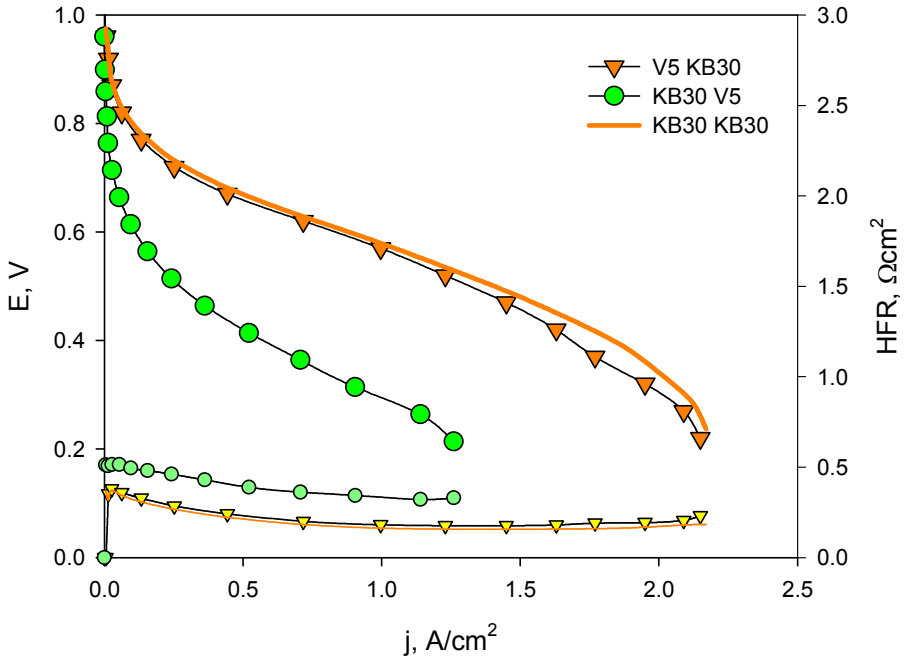

Figure 4.18: Polarization curves for KB30V5 and V5KB30 MEAs under 20% RH, H_2/O_2, 2:3 stoich, atm, 80 ºC, non-IR-corrected. The standard Ketjen Black 30 wt% ionomer CL is shown for reference.

Under operation in air, the fuel cell performance of all three MEAs drastically decreases due to slower reaction kinetics, whereas the trends observed under operation in oxygen remain, as shown in Figure 4.19. The lowest performance is observed in the case of the KB30V5 MEA; V5KB30 and KB30KB30 are very similar in performance.

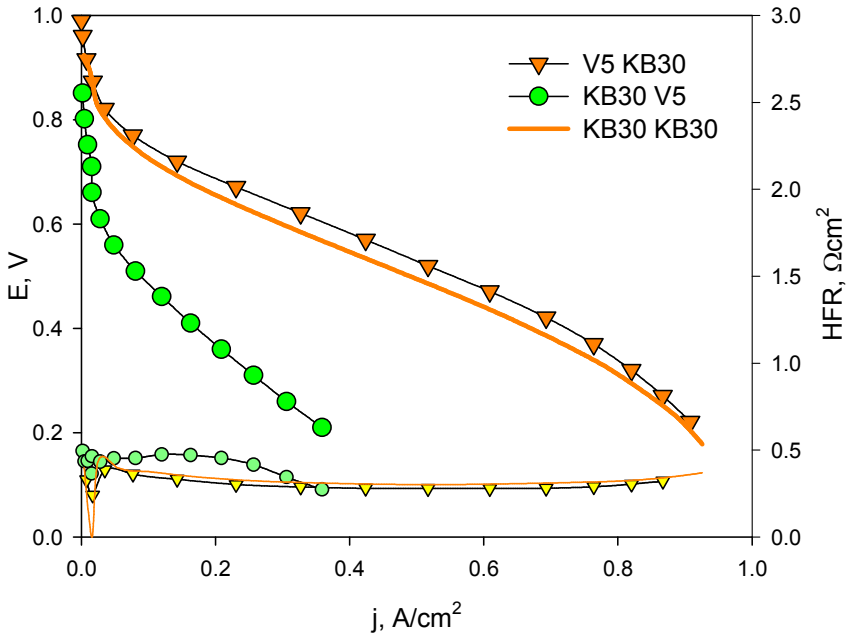

Figure 4.19: Air polarization curves for KB30V5 and V5KB30 MEAs under 20% RH, H_2/Air, 2:3 stoich, atm, 80 ºC, non-IR-corrected. The standard Ketjen Black 30 wt% ionomer CL is shown for reference.

Based on the presented above polarisation curves of the asymmetrical MEAs, it is speculated that the ionomer loading can be reduced in one of the CLs in an MEA without dramatic performance losses. However, whether the reduction is performed on the anode or the cathode depends on the expected operating conditions of the fuel cell. If the operation in low RH condition is required, as often requested by automotive applications[15], reduction of the anode ionomer loading from 30 to 5 wt% ionomer can be achieved without any performance losses. On the other hand, reduction of the ionomer loading on the cathode might be meaningful in order to improve performance in the mass transport region if the fuel cell is operated under fully humidified conditions in under air.

4.4 Conclusion

The microstructure of conventional catalyst layers has a significant impact on water management properties of CLs and on the fuel cell performance. Water sorption properties depend on the pore size distribution of carbon support materials and ionomer loading in the CL. The larger the fraction of mesopores (< 20 nm), the more pronounced the capillary condensation of water in these pores and thus the higher the degree of water retention in the CL. Incorporation of ionomer into the CL enhances water sorption.

Electrochemically active surface is found to be a function of carbon microstructure and ionomer content in the CL. In CLs with ionomer loading < 50 wt%, ESA was found to strongly depend on the amount of water in the CL indicating that water serves as a proton conducting medium in the CL, and Pt particles need not necessarily be in direct contact with ionomer to participate in the fuel cell reaction. However, in the case of the Ketjen Black-based 5 wt% CL, an exponential increase in ESA with RH suggests that a large fraction of Pt is deposited in the range of mesopores < 20 nm, which are believed to be inside of agglomerates, and that Pt is only active when these pores are filled with water through capillary condensation. In other words, a majority of Pt remains inactive in the range of low to intermediate RH in Ketjen Black-based CLs. In contrast, in the Vulcan-based CLs containing 5 wt% ionomer, a linear increase in ESA with RH suggests that Pt particles are located in the pores easily accessible to water. However, it has to be taken into account that in the operating fuel cell, water content in the cathode catalyst layer is usually higher than that determined by by

relative humidity due to production of water. Thus, ESA and proton conductivity are presumed to be enhanced during actual fuel cell operation.

Proton conductivity in the CLs is also a function of water content, and is found to be enhanced in Vulcan-based 5 wt% ionomer CL compared to the Ketjen Black 5 wt% ionomer CL. This effect is attributed to the formation of ionomer-water proton conductive network in which water is believed to provide linkages between disconnected patches of ionomer. This network is assumed to be more connected in the case of Vulcan-based CLs due to a lower pore volume and lower mesoporous surface area of this carbon where ionomer and water are distributed. The ratio of the volume of H^+-conducting phase (ionomer + water) to the mesoporous surface area of Pt/carbon, $V_{(I+H2O)}/SA_{(meso),}$ is found to be a useful parameter for estimating the connectivity of the water + ionomer network and might be employed for evaluating the optimal ionomer loading for a particular carbon support.

Polarization losses are dominated by proton conduction, i.e., proton concentration at the reaction site, in the CLs with 5 wt% ionomer content. Proton transport limitations, however, are largely alleviated in the presence of water. Mass transport losses are negligible in these CLs due to large pore volume available for gas and water transport. In the case of 50 wt% ionomer CLs, mass transport losses dominate the CL performance due to an almost complete blockage of pore space by ionomer and water, and these manifest at current densities as low as 0.1 A/cm^2.

In the Figure 4.20, a schematic of Ketjen Black and Vulcan XC-72-based CLs with 5, 30, and 50 wt% ionomer loading are shown upon water sorption. In 5 wt% ionomer CLs, water is shown to provide linkages between disconnected patches of ionomer; ionomer and water contents are however low enough to leave unoccupied pore space and provide a direct gas access to the reaction sites, i.e., active reaction sites. As ionomer content increases, pore space becomes filled with ionomer and water, and the active sites become blocked to the gas access, i.e., blocked reaction sites.

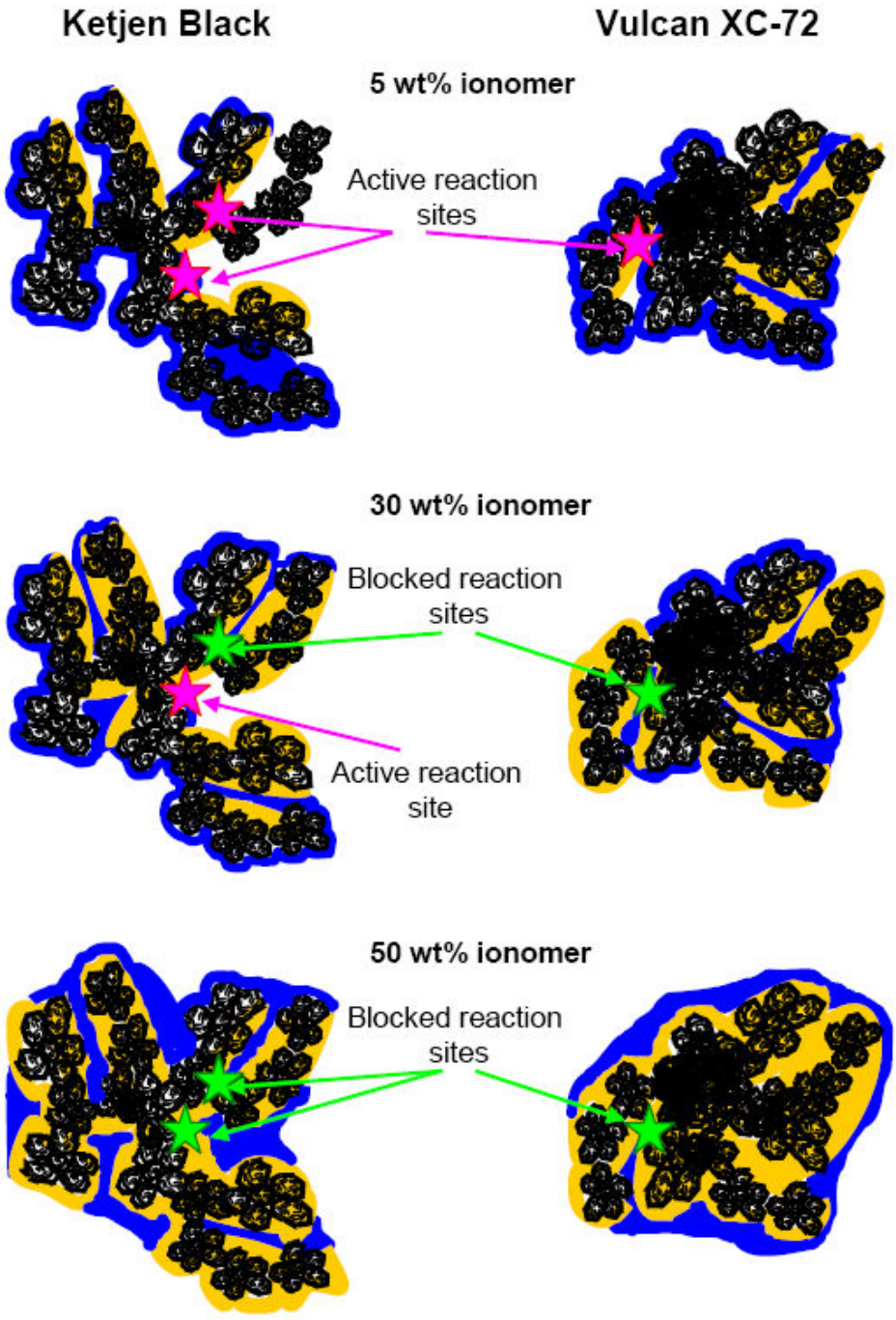

Figure 4.20: A schematic illustrating ionomer and water distribution in the mesopores of Pt/carbon with 5, 30, and 50 wt% ionomer. The active reaction sites that are in contact with gas, proton and electron conductive phases are shown in pink. The reaction sites with a hindered gas access by ionomer and water, i.e., blocked sites, are shown in green.

Based on these findings, we speculate that mesoporous carbons with relatively low surface area (< 200 m^2/g) and a negligible fraction of micropores (< 2 nm) can be beneficial for the purpose of decreasing ionomer content in the CL while maintaining the adequate fuel cell performance. The lower the mesoporous area, the lower ionomer loading is required for formation of connected ionomer network. Platinum, if located in the mesopores too large for capillary condensation, is in direct contact with gas phase over a wide range of RH as opposed to Pt located in the pores < 20 nm inside agglomerates that are filled with water. Although ESA and proton conductivity are reduced in low ionomer CLs, if operated under humidified conditions, water seem to largely compensate the loss by forming active Pt-water interface and water linkages between disconnected patches of ionomer. Production of liquid water at the cathode during fuel cell operation is believed to have a particularly beneficial effect on proton conductivity of low ionomer cathode catalyst layers.

On the anode side, carbons with a broad pore size distribution comprising a large fraction of pores < 20 nm that are prone to capillary condensation and pore trapping effects are favourable. High ionomer content enhances water sorption and retention, which prevents the anode catalyst layer from dehydration.

The presented hypothesis is confirmed for the fuel cell operation under high relative humidity in air. However, in the low relative humidity operation, low ionomer content on the cathode seems to be strongly detrimental for the fuel cell performance. This is assumed to be due to decrease in the ESA and disruption of the water-ionomer H^+-conducting network. On the other hand, low ionomer

content on the anode does not seem to have any negative impact on the total fuel cell performance under dry operating conditions.

It is shown that ionomer loading greatly depends on the mesoporous surface area of the carbon support. The lower the area of the mesopores, the lower the ionomer loading that can be employed without major reduction in performance. Mesoporous carbons seem to be a better choice for the purpose of high Pt utilization, especially in low relative humidity operating conditions, where a large fraction of Pt particles is in direct contact with ionomer and reactant gas. If Pt is deposited in the intra-agglomerate pores < 20 nm that are covered with ionomer, Pt is active only at high relative humidity. In conclusion, mesoporous carbons, similar to Vulcan XC-72, have the potential for reducing ionomer loading in the CLs while still providing an adequate Pt utilization suitable for fuel cell operation at dry conditions.

5: CONCLUSION AND FUTURE WORK

In this thesis, microstructures of conventional catalyst layers employing Ketjen Black and Vulcan XC-72 carbons as Pt supports have been investigated and correlated to water sorption, retention and desorption, electrochemical properties, and fuel cell polarization performance.

N_2 adsorption, scanning and transmission electron microscopy were employed to study microstructure of CLs and to explain its evolution from the original microstructures of carbon blacks to Pt/carbon supported catalysts, and to Pt/carbon/ionomer catalyst layers. It was found that the inherent character of carbon particles agglomeration/aggregation observed in the powder form is preserved upon formation of the catalyst layer – carbon serves as a rigid framework for the distribution of Pt and ionomer. This finding suggests that the architecture of the catalyst support is the decisive factor in the formation of the CL microstructure. Thus, properties such as porosity, pore size distribution, pore shape and pore connectivity have to be carefully controlled in the design of novel Pt supports.

The function of micropores < 2 nm, which greatly contribute to the surface area of the carbon support, needs to be further clarified. It was found that a significant fraction of micropores in Ketjen Black is blocked by Pt particles upon formation of the Pt/Ketjen composite, hence the microporous surface area and the pore volume is ineffective for the actual fuel cell reaction. The necks of

micropores, which largely comprise of reactive edge-sites, are assumed to serve as active sites for Pt adsorption. These findings have several implications in regard to designing novel catalyst supports. The relationship between the high surface area of the catalyst support and the efficient catalyst particles distribution is not so straightforward if a large fraction of the surface area originates from micropores < 2 nm. Hence, it is suggested that microporous surface area of the catalyst support is not available for the dispersion of Pt particles. The high chemical activity of the necks of micropores comprised largely of the edge sites might be important for Pt dispersion onto the support but is detrimental for carbon support stability. The edge sites are prone to oxidation therefore facilitating carbon degradation in the fuel cell operating environment. Thus, graphitic carbons that possess fewer surface defects, i.e., fewer edge sites, are beneficial for the stability of carbons. Future considerations towards clarification of the mechanisms of Pt adsorption on the carbon support in regard to the role of both edge-sites and basal planes of the carbon surface, and of oxygen-containing surface groups may facilitate the design of more stable catalyst supports while ensuring a high dispersion of Pt. X-ray diffraction study of carbons and Pt/carbon composites might provide useful information about crystallinity of carbons and the fraction of basal planes to edge sites. It also might be useful for examining Pt location on carbon particles.

It was found that the pore volume of intra-agglomerate pores (< 20 nm) decreases drastically with the addition of ionomer. It is assumed that ionomer distributes on the surface of agglomerates covering the intra-agglomerate pores

(< 20 nm) and that this occurs at quite low ionomer loadings, e.g., as low as 5 wt% ionomer. For the purpose of fuel cell operation, it is essential that the ionomer content is low enough to sustain the appropriate void fraction for gaseous mass transport, while still being sufficient to form an ionomer network for proton conduction. *It is postulated that the ionomer loading in the CL is a function of mesoporous surface area and it is suggested that the optimal ionomer loading in a CL should be adjusted to the mesoporous surface area of each catalyst support.* In this thesis, however, the mesoporous area includes pores > 2 nm, while surface area of pores > 20 nm should used in the estimation of the optimal ionomer loading. A methodology for determining surface area of pores > 20 nm would be a useful tool.

The CL microstructure was found to exert a strong influence on water sorption and retention properties. The presence of mesopores, where capillary condensation occurs, enhances water sorption in the intermediate range of relative humidity (30 – 90% RH). A broad pore size distribution with a large fraction of micro- and lower range mesopores (< 20 nm), as in the case of Ketjen Black, was observed to enhance water retention due to pore trapping effects. Correspondingly, Ketjen black-based CLs were found to possess an enhanced water retaining capability in the intermediate RH. Based on these considerations, it is speculated that Ketjen Black-based CLs may show improved performance when employed as anode CLs, where de-hydration is an issue, while they are predicted to suffer greater gas transport limitations when employed as cathode CLs, especially if operated under high RH and in the high current density region.

Nafion ionomer was found to enhance total water uptake of CLs. It is suggested that catalyst supports with a broad pore size distribution, a large fraction of mesopores for capillary condensation, and a high ionomer content are advantageous to the anode, whereas materials with a narrower pore size distribution in the mesoporous range facilitate water removal from the cathode CLs alleviating flooding issues. The ionomer content ought to be varied on the anode and the cathode depending on the mesoporous surface area of the employed carbon support and expected fuel cell operating conditions. Useful information about hydrophobicity of carbons and Pt/carbon composites might be obtained from adsorption experiments using hydrophobic adsorbates, such as benzene.

The electrochemically active surface area and proton conductivity were found to be a function of carbon microstructure and ionomer content in the CL. In CLs possessing ionomer loadings < 50 wt%, the ESA and proton conductivity were found to depend strongly on the amount of water in the CL, providing evidence that water serves as a proton conducting medium in the CL, and that *Pt particles need not necessarily be in close proximity with ionomer to participate in fuel cell electrochemistry*. However, in the case of the Ketjen Black-based 5 wt% CL, a large fraction of Pt seems to be deposited in the lower range mesopores (< 20 nm) inside of agglomerates, and is only active when these pores are filled with water at high relative humidity. In other words, Pt utilization in the case of Ketjen Black catalyst support is very low under low RH operating conditions. In contrast, a higher Pt utilization in Vulcan-based 5 wt% ionomer CLs under low RH

condition is attributed to the fact that a larger fraction of Pt is located in the pores > 20 nm and is in contact with ionomer, as illustrated by the ratio $V_{(I+H2O)}/SA_{(meso)}$. An interesting insight might be obtained from comparison of the electrochemically determined ESA values with the gas phase adsorption of hydrogen under vacuum in Pt/carbon composites and catalyst layers using BET adsorption instrument. However, hydrogen spill-over effects have to be taking into account when analysing Pt surface area determined by this method. An alternative to such an experiment could be employment of carbon monoxide as adsorbate, which preferentially adsorbs on Pt surface. In the design of CLs for operation in low relative humidity conditions, as required by automotive applications, elucidation of the differences in water sorption and desorption in the intra-agglomerate pores (< 20 nm), which are blocked by a layer of ionomer on the surface of the agglomerate, and inter-agglomerate pores (> 20 nm), which contain ionomer inside the pore, would provide further information in relation to the optimal design of CLs. Further considerations towards clarification of water sorption and retention mechanisms in agglomerate structure catalyst supports and alternative architectures, such as ordered mesoporous carbons, are essential for selecting optimal catalyst support architecture.

Polarization losses are dominated by proton conduction in the CLs with very low ionomer content. Proton transport limitations, however, are largely alleviated in the presence of water. In the high ionomer loading CLs, mass transport losses dominate the CL performance and manifest at current densities as low as 100 mA/cm^2. Overall, mass transport limitations exert a much larger negative impact

on performance than interfacial kinetic limitations. Taking into account that the peak power density of the fuel cell is at ~ 2/3 of the limiting current density, i.e., in the mass transport region, this implies that CLs with improved mass transport properties may possess a greater potential in enhancing fuel cell performance than CLs with improved interfacial kinetic properties.

Based on these findings, it is suggested that mesoporous carbons with pore sizes > 20 nm should be investigated for fuel cell applications. It seems essential that Pt particles are located in the pores > 20 nm. This provides close proximity of Pt to the ionomer and the reactant gas that in turn allows for high Pt utilization under low RH operating conditions. On the other hand, under high RH operating conditions, these larger pores are less likely to be filled with water because of absence of capillary condensation in the pores of this diameter; thus, efficient gaseous transport to the reaction sites is maintained. High ionomer content CLs are found to enhance water sorption and retention and thus these CLs are expected to be beneficial for the anode CLs, where reduced proton conductivity due to dehydration is an issue.

It is proposed that mesoporous carbon supports should be further investigated for application in the fuel cell with a careful systematic examination of structural parameters, water transport and electrochemical properties. Mesoporous materials with following structural properties should be investigated:

- various morphologies, e.g., highly ordered templated carbons and disordered aerogel carbons

- various interconnectivities of the pores, e.g., ordered networks of straight cylindrical pores and tortuous worm-like pore networks
- very high mesoporous surface area (~ 1000 m^2/g) and low mesoporous surface area (~ 200 m^2/g)
- mono-modal and multi-modal pore size distributions

Due to the different water management requirements posed on the cathode and the anode CLs by the nature of fuel cell operation, CLs with different microstructures and water sorption and retention properties should be used on the cathode and the anode.

REFERENCE LIST

(1) Carrette, L.; Friedrich, K. A.; Stimming, U. *Chemphyschem* **2000**, *1*, 162.

(2) Vielstich, W. L., Arnold; Gasteiger, Hubert *Handbook of Fuel Cells*; Wiley&Sons Ltd, 2003; Vol. 3.

(3) Cooper, K. R.; Ramani, V.; Fenton, J. M.; Kunz, R. *Experimental methods and data analysis for polymer electrolyte fuel cells*; Scribner Associates, 2005.

(4) Bard, A. J.; Faulkner, L. R. *Electrochemical methods: fundamentals and applications*; John Wiley & Sons, Inc., 2001.

(5) Kinoshita, K. *Electrochemical Oxygen Technology*; Wiley, 1992.

(6) Murphy, O. J.; Hitchens, G. D.; Manko, D. J. *Journal of Power Sources* **1994**, *47*, 353.

(7) Ralph, T. R.; Hards, G. A.; Keating, J. E.; Campbell, S. A.; Wilkinson, D. P.; Davis, M.; StPierre, J.; Johnson, M. C. *Journal of the Electrochemical Society* **1997**, *144*, 3845.

(8) Raistrick, I. D. “in Diaphragms, Separators, and Ion Exchange Memrbanes”, 1986.

(9) Uchida, M.; Aoyama, Y.; Eda, N.; Ohta, A. *Journal of the Electrochemical Society* **1995**, *142*, 4143.

(10) Ticianelli, E. A.; Derouin, C. R.; Redondo, A.; Srinivasan, S. *Journal of the Electrochemical Society* **1988**, *135*, 2209.

(11) Srinivasan, S.; Ticianelli, E. A.; Derouin, C. R.; Redondo, A. *Journal of Power Sources* **1988**, *22*, 359.

(12) Paganin, V. A.; Ticianelli, E. A.; Gonzalez, E. R. *Journal of Applied Electrochemistry* **1996**, *26*, 297.

(13) Wilson, M. S.; Gottesfeld, S. *Journal of Applied Electrochemistry* **1992**, *22*, 1.

(14) Uchida, M.; Aoyama, Y.; Eda, N.; Ohta, A. *Journal of the Electrochemical Society* **1995**, *142*, 463.

(15) Costamagna, P.; Srinivasan, S. *Journal of Power Sources* **2001**, *102*, 242.

(16) Wilson, M. S.; Gottesfeld, S. *Journal of the Electrochemical Society* **1992**, *139*, L28.

(17) Antolini, E.; Giorgi, L.; Pozio, A.; Passalacqua, E. *Journal of Power Sources* **1999**, *77*, 136.

(18) Andreaus, B.; Eikerling, M. *Device and materials modeling in PEM fuel cells*, 2009.

(19) Sakai, T.; Takenaka, H.; Torikai, E. *Journal of the Electrochemical Society* **1986**, *133*, 88.

(20) Lufrano, F.; Passalacqua, E.; Squadrito, G.; Patti, A.; Giorgi, L. *Journal of Applied Electrochemistry* **1999**, *29*, 445.

(21) Park, S.; Lee, J. W.; Popov, B. N. *Journal of Power Sources* **2006**, *163*, 357.

(22) Multi-Year Research, Development and Demonstration Plan: Planned Program Activities for 2005-2015; Energy, U. D. o., Ed.; http://www1.eere.energy.gov/hydrogenandfuelcells/mypp/, 2005.

(23) Joo, S. H.; Choi, S. J.; Oh, I.; Kwak, J.; Liu, Z.; Terasaki, O.; Ryoo, R. *Nature* **2001**, *412*, 169.

(24) Rao, V.; Simonov, P. A.; Savinova, E. R.; Plaksin, G. V.; Cherepanova, S. V.; Kryukova, G. N.; Stimming, U. *Journal of Power Sources* **2005**, *145*, 178.

(25) Mulik, S.; Sotiriou-Leventis, C.; Leventis, N. *Chemistry of Materials* **2008**, *20*, 6985.

(26) Smirnova, A.; Dong, X.; Hara, H.; Vasiliev, A.; Sammes, N. *International Journal of Hydrogen Energy* **2005**, *30*, 149.

(27) Bonakdarpour, A.; Fleischauer, M. D.; Brett, M. J.; Dahn, J. R. *Applied Catalysis a-General* **2008**, *349*, 110.

(28) Debe, M. K.; Schmoeckel, A. K.; Vernstrorn, G. D.; Atanasoski, R. *Journal of Power Sources* **2006**, *161*, 1002.

(29) Serp, P.; Corrias, M.; Kalck, P. *Applied Catalysis a-General* **2003**, *253*, 337.

(30) Zhang, J.; Lima, F. H. B.; Shao, M. H.; Sasaki, K.; Wang, J. X.; Hanson, J.; Adzic, R. R. *Journal of Physical Chemistry B* **2005**, *109*, 22701.

(31) Borup, R.; Meyers, J.; Pivovar, B.; Kim, Y. S.; Mukundan, R.; Garland, N.; Myers, D.; Wilson, M.; Garzon, F.; Wood, D.; Zelenay, P.; More, K.; Stroh, K.; Zawodzinski, T.; Boncella, J.; McGrath, J. E.; Inaba, M.; Miyatake, K.; Hori, M.; Ota, K.; Ogumi, Z.; Miyata, S.; Nishikata, A.; Siroma, Z.; Uchimoto, Y.; Yasuda, K.; Kimijima, K. I.; Iwashita, N. *Chemical Reviews* **2007**, *107*, 3904.

(32) Kinoshita, K. *Carbon: electrochemical and physicochemical properties*, 1988.

(33) Schoots, K.; Ferioli, F.; Kramer, G. J.; van der Zwaan, B. C. C. *International Journal of Hydrogen Energy* **2008**, *33*, 2630.

(34) Auer, E.; Freund, A.; Pietsch, J.; Tacke, T. *Applied Catalysis a-General* **1998**, *173*, 259.

(35) Kinoshit.K; Bett, J. *Carbon* **1973**, *11*, 237.

(36) Kinoshit.K; Bett, J. A. S. *Carbon* **1973**, *11*, 403.

(37) Beguin, F.; Frackowiak, E. *Carbons for eletrochemical energy storage and conversion systems*, 2010.

(38) Boehm, H. P. *Carbon* **1994**, *32*, 759.

(39) Kangasniemi, K. H.; Condit, D. A.; Jarvi, T. D. *Journal of the Electrochemical Society* **2004**, *151*, E125.

(40) Kim, Y. T.; Ito, Y.; Tadai, K.; Mitani, T.; Kim, U. S.; Kim, H. S.; Cho, B. W. *Applied Physics Letters* **2005**, *87*.

(41) Randin, J. P.; Yeager, E. *Journal of Electroanalytical Chemistry* **1972**, *36*, 257.

(42) Andreas, H. A.; Conway, B. E. *Electrochimica Acta* **2006**, *51*, 6510.

(43) Chu, X.; Kinoshita, K. *Materials Science and Engineering B-Solid State Materials for Advanced Technology* **1997**, *49*, 53.

(44) Randin, J. P.; Yeager, E. *Journal of the Electrochemical Society* **1971**, *118*, 711.

(45) Bleda-Martinez, M. J.; Lozano-Castello, D.; Morallon, E.; Cazorla-Amoros, D.; Linares-Solano, A. *Carbon* **2006**, *44*, 2642.

(46) Gryglewicz, G.; Machnikowski, J.; Lorenc-Grabowska, E.; Lota, G.; Frackowiak, E. *Electrochimica Acta* **2005**, *50*, 1197.

(47) Lozano-Castello, D.; Cazorla-Amoros, D.; Linares-Solano, A.; Shiraishi, S.; Kurihara, H.; Oya, A. *Carbon* **2003**, *41*, 1765.

(48) Vilinskaya, V. S.; Korobanov, A. A.; Burshtein, R. K.; Gerasimova, A. V. *Bulletin of the Academy of Sciences of the Ussr Division of Chemical Science* **1978**, *27*, 865.

(49) Shi, H. *Electrochimica Acta* **1996**, *41*, 1633.

(50) Chmiola, J.; Largeot, C.; Taberna, P. L.; Simon, P.; Gogotsi, Y. *Angewandte Chemie-International Edition* **2008**, *47*, 3392.

(51) Chmiola, J.; Yushin, G.; Dash, R.; Gogotsi, Y. *Journal of Power Sources* **2006**, *158*, 765.

(52) Chmiola, J.; Yushin, G.; Dash, R. K.; Hoffman, E. N.; Fischer, J. E.; Barsoum, M. W.; Gogotsi, Y. *Electrochemical and Solid State Letters* **2005**, *8*, A357.

(53) Guha, A.; Lu, W. J.; Zawodzinski, T. A.; Schiraldi, D. A. *Carbon* **2007**, *45*, 1506.

(54) Antolini, E. *Journal of Materials Science* **2003**, *38*, 2995.

(55) Serp, P.; Figueiredo, J. L. *Carbon materials afor catalysis*; John Wiley & Sons, Inc., 2009.

(56) Shimazu, K.; Uosaki, K.; Kita, H.; Nodasaka, Y. *Journal of Electroanalytical Chemistry* **1988**, *256*, 481.

(57) Fraga, M. A.; Jordao, E.; Mendes, M. J.; Freitas, M. M. A.; Faria, J. L.; Figueiredo, J. L. *Journal of Catalysis* **2002**, *209*, 355.

(58) Vandam, H. E.; Vanbekkum, H. *Journal of Catalysis* **1991**, *131*, 335.

(59) Coloma, F.; Sepulvedaescribano, A.; Fierro, J. L. G.; Rodriguezreinoso, F. *Langmuir* **1994**, *10*, 750.

(60) de Miguel, S. R.; Scelza, O. A.; Roman-Martinez, M. C.; de Lecea, C. S. M.; Cazorla-Amoros, D.; Linares-Solano, A. *Applied Catalysis a-General* **1998**, *170*, 93.

(61) Sepulveda-Escribano, A.; Coloma, F.; Rodriguez-Reinoso, F. *Applied Catalysis a-General* **1998**, *173*, 247.

(62) Heal, G. R.; Mkayula, L. L. *Carbon* **1988**, *26*, 803.

(63) Heal, G. R.; Mkayula, L. L. *Carbon* **1988**, *26*, 815.

(64) Watanabe, M.; Uchida, M.; Motoo, S. *Journal of Electroanalytical Chemistry* **1987**, *229*, 395.

(65) Turkevich, J.; Miner, R. S.; Babenkova, L. *Journal of Physical Chemistry* **1986**, *90*, 4765.

(66) Honji, A.; Mori, T.; Hishinuma, Y. *Journal of the Electrochemical Society* **1990**, *137*, 2084.

(67) Wang, X.; Hsing, I. M. *Electrochimica Acta* **2002**, *47*, 2981.

(68) Kim, M. S.; Park, J. N.; Kim, H. Electrode catalyst for fuel cell. In *US Patent Application Publication* Korea, 2006.

(69) Uchida, M.; Aoyama, Y.; Tanabe, M.; Yanagihara, N.; Eda, N.; Ohta, A. *Journal of the Electrochemical Society* **1995**, *142*, 2572.

(70) Watanabe, M.; Sei, H.; Stonehart, P. *Journal of Electroanalytical Chemistry* **1989**, *261*, 375.

(71) McBreen, J.; Olender, H.; Srinivasan, S.; Kordesch, K. V. *Journal of Applied Electrochemistry* **1981**, *11*, 787.

(72) Watanabe, M.; Saegusa, S.; Stonehart, P. *Chemistry Letters* **1988**, 1487.

(73) Kinoshita, K. *Journal of the Electrochemical Society* **1990**, *137*, 845.

(74) Vanharde.R; Vanmontf.A. *Surface Science* **1966**, *4*, 396.

(75) Vanharde.R; Hartog, F. *Surface Science* **1969**, *15*, 189.

(76) Boudart, M. *American Scientist* **1969**, *57*, 97.

(77) Peuckert, M.; Yoneda, T.; Betta, R. A. D.; Boudart, M. *Journal of the Electrochemical Society* **1986**, *133*, 944.

(78) Mayrhofer, K. J. J.; Blizanac, B. B.; Arenz, M.; Stamenkovic, V. R.; Ross, P. N.; Markovic, N. M. *Journal of Physical Chemistry B* **2005**, *109*, 14433.

(79) Mayrhofer, K. J. J.; Strmcnik, D.; Blizanac, B. B.; Stamenkovic, V.; Arenz, M.; Markovic, N. M. *Electrochimica Acta* **2008**, *53*, 3181.

(80) Han, B. C.; Miranda, C. R.; Ceder, G. *Physical Review B* **2008**, *77*.

(81) Sun, Y.; Zhuang, L.; Lu, J.; Hong, X.; Liu, P. *Journal of the American Chemical Society* **2007**, *129*, 15465.

(82) Eikerling, M. *Journal of the Electrochemical Society* **2006**, *153*, E58.

(83) Malek, K.; Eikerling, M.; Wang, Q. P.; Navessin, T. C.; Liu, Z. S. *Journal of Physical Chemistry C* **2007**, *111*, 13627.

(84) Eikerling, M.; Kornyshev, A. A. *Journal of Electroanalytical Chemistry* **1998**, *453*, 89.

(85) Eikerling, M.; Ioselevich, A. S.; Kornyshev, A. A. *Fuel Cells* **2004**, *4*.

(86) Uchida, M.; Fukuoka, Y.; Sugawara, Y.; Eda, N.; Ohta, A. *Journal of the Electrochemical Society* **1996**, *143*, 2245.

(87) Ridge, S. J.; White, R. E.; Tsou, Y.; Beaver, R. N.; Eisman, G. A. *Journal of the Electrochemical Society* **1989**, *136*, 1902.

(88) Ihonen, J.; Jaouen, F.; Lindbergh, G.; Lundblad, A.; Sundholm, G. *Journal of the Electrochemical Society* **2002**, *149*, A448.

(89) Jaouen, F.; Lindbergh, G.; Sundholm, G. *Journal of the Electrochemical Society* **2002**, *149*, A437.

(90) Soboleva, T.; Zhao, X. S.; Mallek, K.; Xie, Z.; Navessin, T.; Holdcroft, S. *Acs Applied Materials & Interfaces* **2010**, *2*, 375.

(91) Wood, D. L.; Chlistunoff, J.; Majewski, J.; Borup, R. L. *Journal of the American Chemical Society* **2009**, *131*, 18096.

(92) Li, G. C.; Pickup, P. G. *Journal of the Electrochemical Society* **2003**, *150*, C745.

(93) Passalacqua, E.; Lufrano, F.; Squadrito, G.; Patti, A.; Giorgi, L. *Electrochimica Acta* **2001**, *46*, 799.

(94) Gode, P.; Jaouen, F.; Lindbergh, G.; Lundblad, A.; Sundholm, G. *Electrochimica Acta* **2003**, *48*, 4175.

(95) Xie, Z.; Navessin, T.; Shi, K.; Chow, R.; Wang, Q. P.; Song, D. T.; Andreaus, B.; Eikerling, M.; Liu, Z. S.; Holdcroft, S. *Journal of the Electrochemical Society* **2005**, *152*, A1171.

(96) Wan, C. H.; Lin, M. T.; Zhuang, Q. H.; Lin, C. H. *Surface & Coatings Technology* **2006**, *201*, 214.

(97) Marie, R.; Roller, J.; Neagu, R.; Fatih, K.; Tuck, A. Low Pt loading thin cathode catalyst layer by Reactive Spray Deposition Technology. In *Fuel Cell Seminar 2007*; Williams, M., Krist, K., Garland, N., Satyapal, S., Eds., 2008; Vol. 12; pp 59.

(98) Alberti, G.; Casciola, M.; Massinelli, L.; Bauer, B. *Journal of Membrane Science* **2001**, *185*, 73.

(99) Weber, A. Z.; Newman, J. *Journal of the Electrochemical Society* **2003**, *150*, A1008.

(100) Kreuer, K. D. *Journal of Membrane Science* **2001**, *185*, 29.

(101) Mauritz, K. A.; Moore, R. B. *Chemical Reviews* **2004**, *104*, 4535.

(102) Jalani, N. H.; Datta, R. *Journal of Membrane Science* **2005**, *264*, 167.

(103) Jalani, N. H.; Choi, P.; Datta, R. *Journal of Membrane Science* **2005**, *254*, 31.

(104) Choi, P. H.; Datta, R. *Journal of the Electrochemical Society* **2003**, *150*, E601.

(105) Kreuer, K. D.; Paddison, S. J.; Spohr, E.; Schuster, M. *Chemical Reviews* **2004**, *104*, 4637.

(106) Kreuer, K. D. *Chemistry of Materials* **1996**, *8*, 610.

(107) Eikerling, M.; Kornyshev, A. A.; Kuznetsov, A. M.; Ulstrup, J.; Walbran, S. *Journal of Physical Chemistry B* **2001**, *105*, 3646.

(108) Hickner, M. A.; Ghassemi, H.; Kim, Y. S.; Einsla, B. R.; McGrath, J. E. *Chemical Reviews* **2004**, *104*, 4587.

(109) Peckham, T. J.; Yang, Y.; Holdcroft, S. *Key Materials in Fuel Cells, Part 1: PEM fuel cells*; Taylor & Francis: London, 2010.

(110) Rikukawa, M.; Sanui, K. *Progress in Polymer Science* **2000**, *25*, 1463.

(111) Gebel, G. *Polymer* **2000**, *41*, 5829.

(112) Arico, A. S.; Creti, P.; Antonucci, P. L.; Cho, J.; Kim, H.; Antonucci, V. *Electrochimica Acta* **1998**, *43*, 3719.

(113) Uchida, H.; Song, J. M.; Suzuki, S.; Nakazawa, E.; Baba, N.; Watanabe, M. *Journal of Physical Chemistry B* **2006**, *110*, 13319.

(114) Hiesgen, R.; Eberhardt, D.; Aleksandrova, E.; Friedrich, K. A. *Fuel Cells* **2006**, *6*, 425.

(115) Beattie, P. D.; Basura, V. I.; Holdcroft, S. *Journal of Electroanalytical Chemistry* **1999**, *468*, 180.

(116) Ignaszak, A.; Ye, S. Y.; Gyenge, E. *Journal of Physical Chemistry C* **2009**, *113*, 298.

(117) Leofanti, G.; Padovan, M.; Tozzola, G.; Venturelli, B. *Catalysis Today* **1998**, *41*, 207.

(118) IUPAC. Reporting physisorption data for gas/solid systems with special reference to the determination of surface area and porosity, 1985; Vol. 57; pp 603.

(119) IUPAC "Recommendations for the characterisation of porous solids," 1994.

(120) Gregg, S. J. S., K.S. *Adsorption, surface area and porosity*, 2nd ed.; Academic Press, 1982.

(121) Thomas, J. M. *Introduction to the principles of heterogeneous catalysis*; Academic Press, 1967.

(122) Dubinin, M. M. *Chemical Reviews* **1960**, *60*, 235.

(123) Dubinin, M. M.; Vyshnyakova, M. M.; Zhukovskaya, E. G.; Leontev, E. A.; Lukyanovich, V. M.; Sarakhov, A. I. *Zhurnal Fizicheskoi Khimii* **1960**, *34*, 2019.

(124) Solcova, O.; Matejova, L.; Schneider, P. *Applied Catalysis a-General* **2006**, *313*, 167.

(125) Deboer, J. H.; Lippens, B. C.; Linsen, B. G.; Broekhof.Jc; Vandenhe.A; Osinga, T. J. *Journal of Colloid and Interface Science* **1966**, *21*, 405.

(126) Deboer, J. H.; Linsen, B. G.; Osinga, T. J. *Journal of Catalysis* **1965**, *4*, 643.

(127) Deboer, J. H.; Linsen, B. G.; Vanderpl.T; Zonderva.Gj. *Journal of Catalysis* **1965**, *4*, 649.

(128) Deboer, J. H.; Lippens, B. C. *Journal of Catalysis* **1964**, *3*, 38.

(129) Lippens, B. C.; Deboer, J. H. *Journal of Catalysis* **1964**, *3*, 44.

(130) Lippens, B. C.; Deboer, J. H. *Journal of Catalysis* **1965**, *4*, 319.

(131) Lippens, B. C.; Linsen, B. G.; Deboer, J. H. *Journal of Catalysis* **1964**, *3*, 32.

(132) Barrett, E. P.; Joyner, L. G.; Halenda, P. P. *Journal of the American Chemical Society* **1951**, *73*, 373.

(133) Xie, Z.; Zhao, X. S.; Adachi, M.; Shi, Z. Q.; Mashio, T.; Ohma, A.; Shinohara, K.; Holdcroft, S.; Navessin, T. *Energy & Environmental Science* **2008**, *1*, 184.

(134) Barsoukov, E.; Macdonald, J. R. *Impedance spectroscopy theory, experiment , and application*; Wiley-Interscience: New Jersey, 2005.

(135) Easton, E. B.; Pickup, P. G. *Electrochimica Acta* **2005**, *50*, 2469.

(136) Eikerling, M.; Kornyshev, A. A. *Journal of Electroanalytical Chemistry* **1999**, *475*, 107.

(137) De Levie, R. *in Advances in Electrochemistry and Electrochemical Engenieering*; Interscience: New York, 1967; Vol. 6.

(138) Goldstein, J.; Newbury, D.; Echlin, P.; Joy, D. *Scanning Electron Microscopy and X-Ray Microanalysis*; Kluwer Academic: New York, 2003.

(139) Williams, D. B.; Carter, C. B. *Transmission Electron Microscopy*; Springer, 2009.

(140) Debe, M. K. *Handbook of Fuel Cells: Fundamentals, Technology and Applications*; John Wiley&Sons: Chichester, 2003; Vol. 3.

(141) Gong, K. P.; Du, F.; Xia, Z. H.; Durstock, M.; Dai, L. M. *Science* **2009**, *323*, 760.

(142) Caillard, A.; Coutanceau, C.; Brault, P.; Mathias, J.; Leger, J. M. *Journal of Power Sources* **2006**, *162*, 66.

(143) Springer, T. E.; Raistrick, I. D. *Journal of the Electrochemical Society* **1989**, *136*, 1594.

(144) Broka, K.; Ekdunge, P. *Journal of Applied Electrochemistry* **1997**, *27*, 281.

(145) Wang, Q. P.; Eikerling, M.; Song, D. T.; Liu, Z. S. *Journal of Electroanalytical Chemistry* **2004**, *573*, 61.

(146) Kruk, M.; Jaroniec, M. *Chemistry of Materials* **2001**, *13*, 3169.

(147) Choma, J.; Jaroniec, M.; Piotrowska, J. *Carbon* **1988**, *26*, 1.

(148) Dubinin, M. M. *Carbon* **1987**, *25*, 593.

(149) Seaton, N. A.; Walton, J.; Quirke, N. *Carbon* **1989**, *27*, 853.

(150) Kruk, M.; Jaroniec, M.; Bereznitski, Y. *Journal of Colloid and Interface Science* **1996**, *182*, 282.

(151) Liu, H. L.; Seaton, N. A. *Chemical Engineering Science* **1994**, *49*, 1869.

(152) Liu, H. L.; Zhang, L.; Seaton, N. A. *Chemical Engineering Science* **1992**, *47*, 4393.

(153) Murray, K. L.; Seaton, N. A.; Day, M. A. *Langmuir* **1999**, *15*, 6728.

(154) Seaton, N. A. *Chemical Engineering Science* **1991**, *46*, 1895.

(155) Kruk, M.; Jaroniec, M.; Sayari, A. *Langmuir* **1997**, *13*, 6267.

(156) Conway, B. E. *Electrochemical Supercapacitors*, 1999.

(157) Xie, J.; More, K. L.; Zawodzinski, T. A.; Smith, W. H. *Journal of the Electrochemical Society* **2004**, *151*, A1841.

(158) Adachi, M.; Navessin, T.; Xie, Z.; Frisken, B.; Holdcroft, S. *Journal of the Electrochemical Society* **2009**, *156*, B782.

(159) Nam, J. H.; Kaviany, M. *International Journal of Heat and Mass Transfer* **2003**, *46*, 4595.

(160) Lim, C.; Wang, C. Y. *Electrochimica Acta* **2004**, *49*, 4149.

(161) Li, X. G.; Sabir, I.; Park, J. *Journal of Power Sources* **2007**, *163*, 933.

(162) Xue, D.; Dong, Z. *Journal of Power Sources* **1998**, *76*, 69.

(163) Cheng, X. L.; Yi, B. L.; Han, M.; Zhang, J. X.; Qiao, Y. G.; Yu, J. R. *Journal of Power Sources* **1999**, *79*, 75.

(164) Friedmann, R.; Van Nguyen, T. *Journal of the Electrochemical Society*, *157*, B260.

(165) Li, A. D.; Chan, S. H.; Nguyen, N. T. *Electrochemistry Communications* **2009**, *11*, 897.

(166) Yu, H. M.; Ziegler, C.; Oszcipok, M.; Zobel, M.; Hebling, C. *Electrochimica Acta* **2006**, *51*, 1199.

(167) Ma, S.; Chen, Q.; Jogensen, F. H.; Stein, P. C.; Skou, E. M. *Solid State Ionics* **2007**, *178*, 1568.

(168) Kiselev, A. V. Second International Congress on Surface Activity, 1957, London.

(169) Muller, E. A.; Gubbins, K. E. *Carbon* **1998**, *36*, 1433.

(170) Kiselev, A. V.; Kovaleva, N. B.; Korolev, A. I.; Shcherbakova, K. D. *Doklady Akademii Nauk Sssr* **1959**, *124*, 617.

(171) Walker Jr, P. L.; Janov, J. *Journal of Colloid and Interface Science*, *28*, 449.

(172) Pierce, C.; Smith, R. N.; Wiley, J. W.; Cordes, H. *Journal of the American Chemical Society* **1951**, *73*, 4551.

(173) Kulikovsky, A. A.; Divisek, J.; Kornyshev, A. A. *Journal of the Electrochemical Society* **1999**, *146*, 3981.

(174) Parthasarathy, A.; Dave, B.; Srinivasan, S.; Appleby, A. J.; Martin, C. R. *Journal of the Electrochemical Society* **1992**, *139*, 1634.

(175) Zawodzinski, T. A.; Derouin, C.; Radzinski, S.; Sherman, R. J.; Smith, V. T.; Springer, T. E.; Gottesfeld, S. *Journal of the Electrochemical Society* **1993**, *140*, 1041.

(176) Havranek, A.; Wippermann, K. *Journal of Electroanalytical Chemistry* **2004**, *567*, 305.

(177) Iden, H.; Ohma, A.; Shinohara, K. *Journal of the Electrochemical Society* **2009**, *156*, B1078.

(178) Boyer, C.; Gamburzev, S.; Velev, O.; Srinivasan, S.; Appleby, A. J. *Electrochimica Acta* **1998**, *43*, 3703.

(179) Andreaus, B.; McEvoy, A. J.; Scherer, G. G. *Electrochimica Acta* **2002**, *47*, 2223.

(180) Paganin, V. A.; Oliveira, C. L. F.; Ticianelli, E. A.; Springer, T. E.; Gonzalez, E. R. *Electrochimica Acta* **1998**, *43*, 3761.

(181) Buchi, F. N.; Scherer, G. G. *Journal of the Electrochemical Society* **2001**, *148*, A183.

APPENDICES

Appendix A

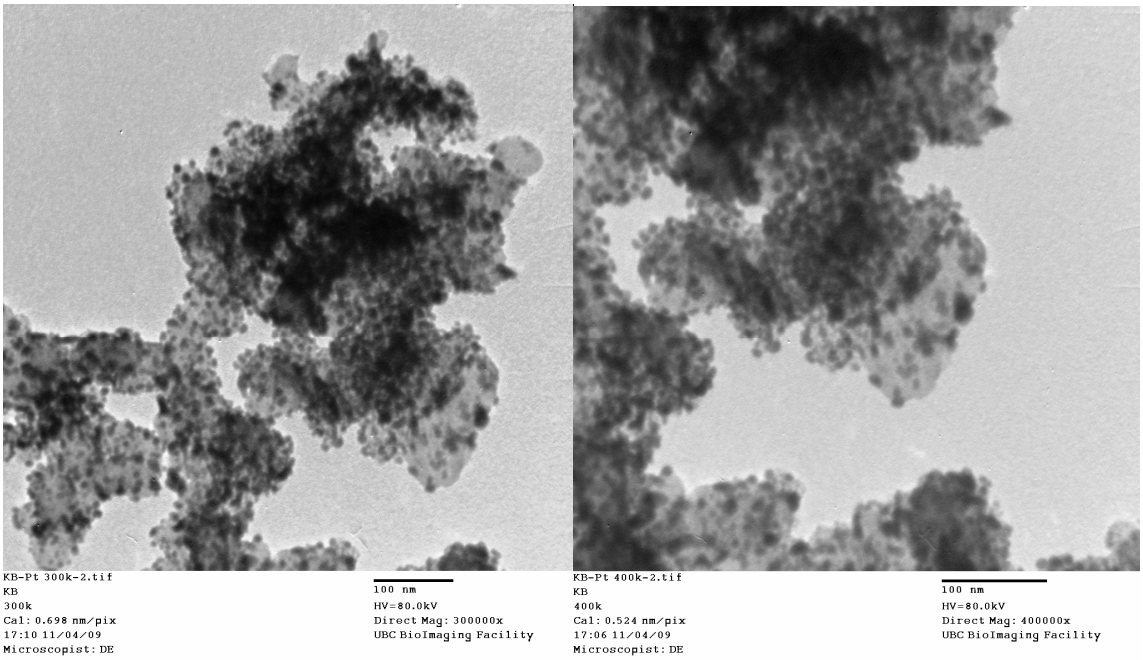

Figure A1: TEM micrographs of Pt/Ketjen Black composite.

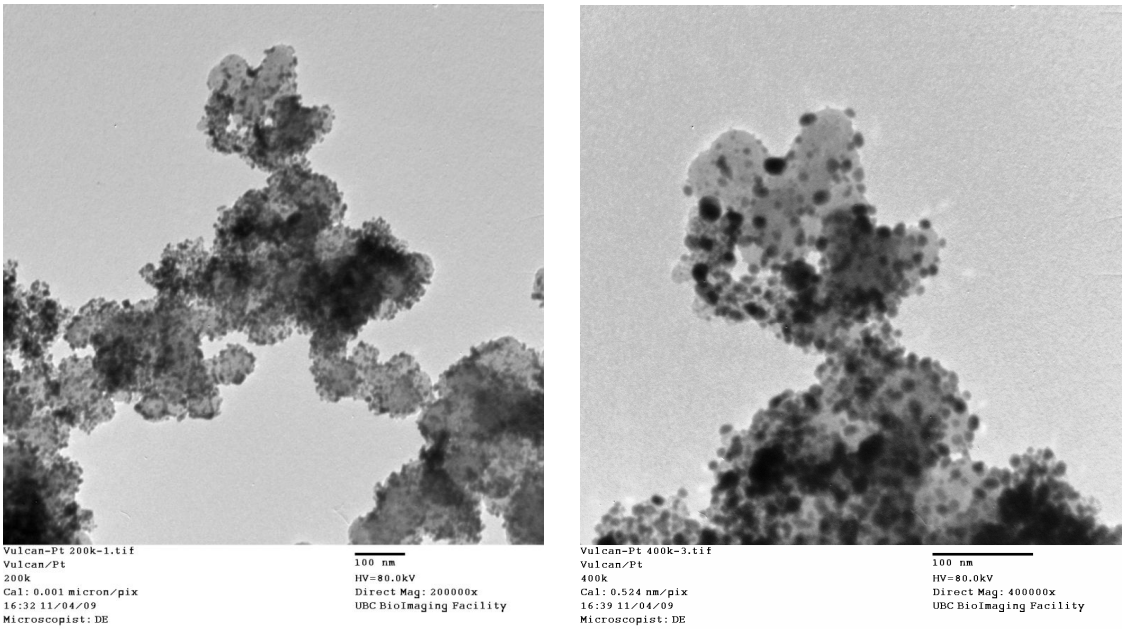

Figure A2: TEM micrographs of Pt/Vulcan composite.

Appendix B

Specifications of catalyst layers

Table B1: Catalyst layers specifications.

	Ionomer loading, wt%	Ionomer loading, mg/cm^2	CL thickness	V fraction, carbon, vol%	V fraction, Pt, vol%	V fraction, ionomer, vol%
Ketjen Black	5	0.0469	15.3± 2.5	15.8	1.2	1.6
	30	0.375	18.5 ± 4.0	13.1	1	11
	50	0.875	9.6 ± 0.8	23.6	1.9	45.7
Vulcan XC-72	5	0.0469	10.0± 0.5	23.6	1.9	2.5
	50	0.875	9.0 ± 0.5	29.5	2.3	57.1

Ionomer loading is calculated from the ionomer/carbon (I/C) ratio. CL thickness is determined from SEM. Volume fraction are calculated from theoretical loadings of the components and the geometry of the CL, as described below.

Carbon loading: 0.48 mg/cm^2

Pt loading: 0.40 mg/cm^2

Density of carbon: 2.01 g/cm^3

Density of Pt: 21.45 g/cm^3

Density of ionomer: 1.914 g/cm^3

$$V_{fraction} = \frac{L}{\rho \cdot d}$$

where L is the loading of a component (g/cm^2), ρ is density (g/cm^3), and d is thickness of the CL (cm).

Appendix C

Water vapour sorption in Nafion membrane and catalyst coated membranes (CCMs).

Isotherms of Ketjen Black-based CCMs coated with catalyst layer on one side (hCCM) and both sides (fCCM) containing 30 wt% ionomer in the CL are shown in Figure below. The ordinate represents the total mass of adsorbed water and shows a net increase in water uptake with addition of a CL on either side of the Nafion 211 membrane. Water uptake of the CL is calculated by subtracting water uptake of Nafion 211 membrane from the total CCM water uptake.

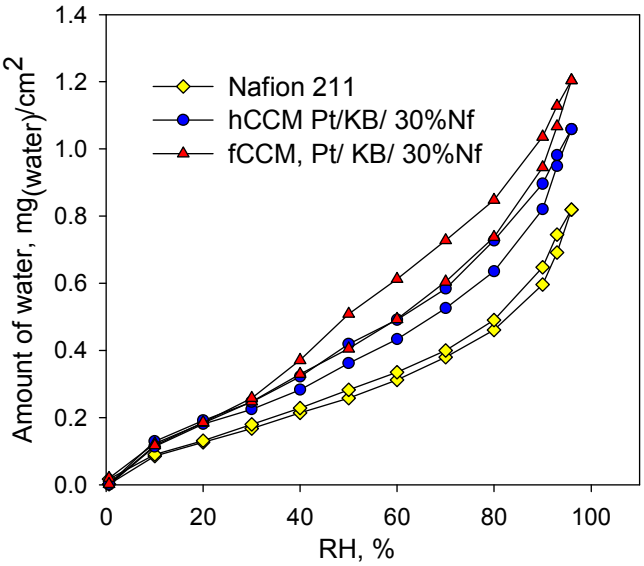

Figure C1: Absolute water content in Nafion membrane, one-side coated membrane (hCCM), and both sides coated membrane (fCCM), 30 wt% ionomer CL, Pt/Ketjen Black.

Water uptake of Nafion 211 during DVS sorption and desorption used for calculation of water uptake in CLs are summarized in the Table C1.

Table C1: Water uptake of Nafion 211 membrane during sorption and desorption.

Sorption			Desorption		
RH, %	Water uptake, -	% error	RH, %	Water uptake, -	% error
0.6	0.00	0	97	0.19	5
10	0.02	10	94	0.17	5
20	0.03	9	90	0.15	5
30	0.04	11	80	0.11	6
40	0.05	12	70	0.09	8
50	0.06	9	60	0.08	6
60	0.07	9	50	0.06	5
70	0.09	6	40	0.05	11
80	0.11	5	30	0.04	12
90	0.14	7	20	0.03	13
94	0.16	7	10	0.02	8
97	0.19	5	0.6	0.00	0

% error is the standard deviation of three Nafion 211 samples.

Appendix D

EIS Nyquist plots for determination of proton resistance

Resistance to proton transport was extracted from Nyquist plots as described in Section 4.2.3. Proton conductivity of the CL was calculated from the proton resistance and the thickness of the CL estimated from SEM. It is assumed that thickness of CLs does not change under fuel cell operation.

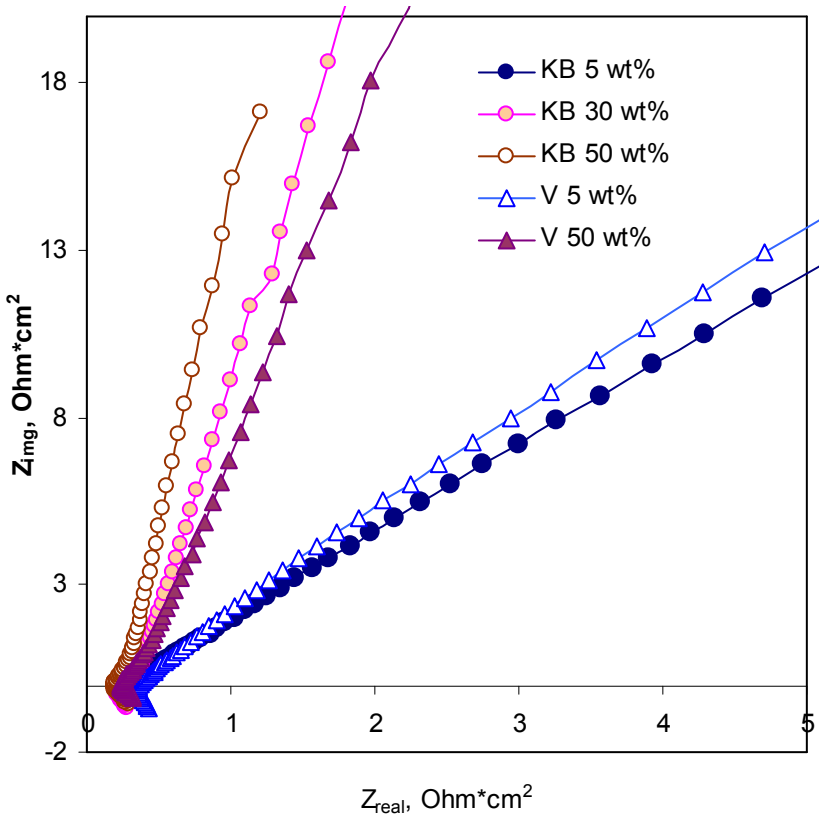

Figure D1: Nyquist plots for Ketjen Black and Vulcan-based CL under 100% RH.

Appendix E

EIS spectra at high current density

At very high current density, > 2 A/cm^2, a second arc in the low frequency region appears in EIS spectra. This is attributed to the dehydration of the anode and the anode side of the membrane at such high current densities.[179-181]

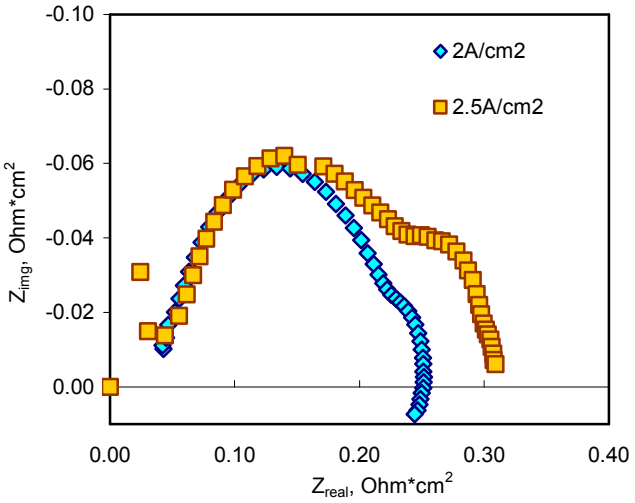

Figure E1: EIS spectra of Ketjen Black 5 wt% ionomer CLs showing the second arc in the low frequency region, H_2/O_2, 100% RH at 2 and 2.5 A/cm^2 current density.

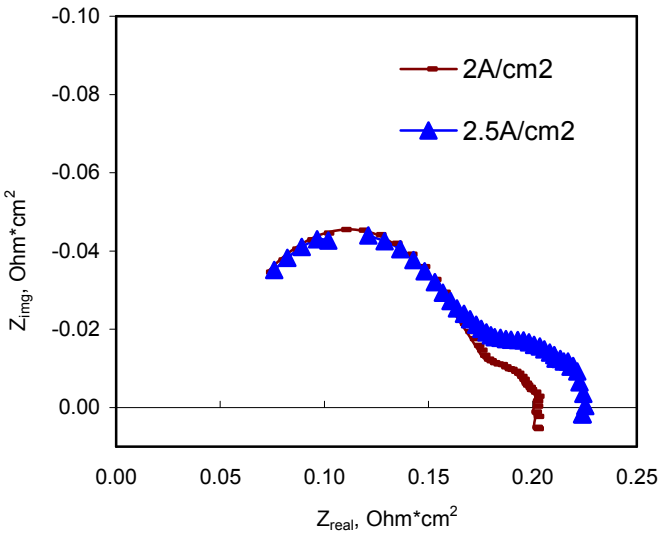

Figure E2: EIS spectra of Vulcan 5 wt% ionomer CLs showing the second arc in the low frequency region, H_2/O_2, 100% RH at 2 and 2.5 A/cm^2 current density.